MEASUREMENT OF THE $^{3}\mathrm{He}(\mathrm{e},\mathrm{e}'\mathrm{p})\mathrm{pn}$ REACTION AT HIGH MISSING ENERGIES AND MOMENTA

BY FATIHA BENMOKHTAR

A dissertation submitted to the

Graduate School—New Brunswick

Rutgers, The State University of New Jersey

in partial fulfillment of the requirements

for the degree of

Doctor of Philosophy

Graduate Program in Physics and Astronomy

Written under the direction of

Professor Ronald Gilman

and approved by

____

____

____

____

____

New Brunswick, New Jersey

October, 2004

ABSTRACT OF THE DISSERTATION

Measurement of the $^3\mathrm{He(e,e'p)pn}$ Reaction at High Missing Energies and Momenta

by Fatiha Benmokhtar

Dissertation Director: Professor Ronald Gilman

We investigate the structure of ^{3}He through the measurement of quasielastic ^{3}He(e,e′). The measurements use the high duty factor electron beam and the high-precision two-spectrometer system in Hall A of the Thomas Jefferson National Accelerator Facility (TJNAF). The measurements were performed in perpendicular kinematics at fixed momentum and energy transfer by the electron, $|\vec{q}|$ = 1.5 GeV/c and ω = 837 MeV, respectively.

A description of the reaction in the plane wave impulse approximation is presented. The experimental equipment is described in detail. For the measurements, the kinematics of the experiment are given. The procedures to remove backgrounds and perform radiative corrections, are also discussed in detail. The detailed method of performing radiative corrections in particular is novel to this work. Finally, the resulting cross sections, distorted spectral functions, and asymmetry A_{TL} are presented, and the physics implications are discussed.

We extracted cross sections and distorted spectral functions up to high missing momentum, p_m up to 1 GeV/c, and up to high missing energies, E_m up to 140 MeV, the

pion production threshold. The experimental data are much higher in statistics and much more extensive in kinematic coverage than any previous measurement. Theoretical predictions are in good agreement with the data, leading to the conclusion that the cross section at large missing momenta is strongly enhanced by nucleon-nucleon correlations, with additional enhancement from final-state interactions. The conventional NN correlations present in a modern three-body nuclear wave function, along with a modern reaction mechanism theory, appear sufficient to explain the data; there is no strong indication of a need to include any additional exotic physics, such as quark degrees of freedom.

Acknowledgements

First of all, I would like to thank my adviser Prof. Ronald Gilman for following this work from a close distance. This thesis wouldn't be achieved without his guidance and encouragements. Thank you Ron for being such a good adviser and for believing on my capacities.

I am grateful to Douglas Highinbotham on playing a very important role in the good functioning of the experiment and his hard work on guiding the analysis. I thank him as well for accepting to be a member in my defense committee. Doug was my second adviser. Thanks Doug.

Many thanks to Prof. Ronald Ransome for his guidance and his precious advices during the four years I spent in Rutgers. I would like to thank him for being confident on my work and I am happy that I didn't disappoint him.

I would like to thank Prof. W. Kloet and Prof. E. Andrei for being members of my defense committee and for the valuable discussions which improved the contents of this thesis.

My special thanks go to Prof. Charles Glashausser for encouraging my application to Rutgers and for being a very good chair of the intermediate energy group.

Many thanks to Prof. Jolie Cizewski for her guidance and encouragements during the years I spent in the graduate school.

I would like to thank all the nuclear physics group in Rutgers, especially Noemie Koller for being such a nice and a sweet person and Prof. Larry Zamick for making work in the nuclear physics group appreciable by organizing the seminars. I am sorry if I solved the puzzles very fast, but I am happy that I won the tea box, it helped me a lot when I was writing the dissertation until very late in the night.

I would like to thank the spokespeople of the experiment: Arun Saha, Marty Epstein and Eric Voutier for their hard work during and after the experiment for believing on my capabilities to analyze the continuum data. Arun was all the time available and ready for discussions, Marty was a very important member in the collaboration, I am thanking him for answering my questions. Thanks to Eric for his encouragements and being confident on my work. I thank him as well for his suggestions and the valuable discussions and ideas.

My special thanks go to Prof. Jean Mougey for intitiating me to the real experimental world of electron scattering and making my dream of working in one of the best laboratories in the world come true.

I would like to thank all the staff of Jefferson Lab and the members of the Hall A collaboration for their hard work on assuring the good functioning of the experiment. My thanks go especially to Kees de Jager, the chair of Hall A.

I would like to thank Prof. Jean-Marc Laget for his theoretical claculations. I have a special respect for Jean-Marc, especially for his challenge on the analysis of the continuum and finding the reaction mechanism in the continuum. Merci Jean-Marc.

Thanks to my magister's adviser Prof. Akila Frahi-Amroun for introducing me to the world of electron scattering and for her valuable instructions. Akila, always encouraged me. Many thanks as well to Prof. N. Bendjabellah for encouraging me to come to the US.

I would like to thank all my friends graduate students or postdocs in Rutgers especially: Indranil Paul, Masud Haque, Jing Yuan, Monica Hasegan, Andrea Zech, Antonia Toropova, Maxim Dion, Marcello Civelli, William Ratcliff, Elena Stefanova, Edouard Boulat, David Brookes, Banu Ilal, the list is so long... I would like to thank especially Benjamin Doyon for his encouragements during the last few months and being with a big help. Merci Benjamin.

I would like to thank my friends in Virginia: Clarrisse, Yordanka, Agus, Rikki, Marcy, Vipuli, Sonja and others. My special thanks go to Marat Rvachev for his hard work during the experiment and providing the group with the R-function which made the calculation of the acceptance of the spectrometers a very simple task.

Many thanks to Kawtar Hafidi for encouraging me and being like an old sister.

I would like to thank my friends from Algeria for keeping contact with me and for being present in my life during these last four years. I would like to thank especially: Ahmed Grigahcen, Zouleikha M. Sahnoun, Toufik Mostefaoui, Murad Hamidouche, Akila Hidouche, Guendouz Wahab and Yogortha Mehious.

And Finally, I would like to thank my family for believing on my capacities, especially my mother Tounsia and my father Amer, I admire them for their patience and courage. They wanted me to become a computer scientist or a doctor in medicine, but they are pretty happy with what I am now. Sahit a yemma, sahit a Vava. Sahit a yathmathniw ath yessethma: Samia, Achour, Mourad, Rachid et Ghania.

Dedication

A ma famille...

Table of Contents

List of Tables

List of Figures

Chapter 1

Introduction

A central goal of nuclear physics is to understand the properties of nuclei, starting from the interaction of free nucleons. While shell-model and collective approaches to understanding nuclear structure have existed for decades, it is only in recent years that advances in computational techniques and computer hardware have allowed calculations starting from the nucleon-nucleon force. With these advances, nuclear physicists are beginning a much more detailed study of topics such as three-body forces in nuclei, and the importance of quark degrees of freedom.

The traditional approach to nuclear structure is essentially a theory of point-like nucleons, that adds in the nucleon form factors as needed. But since the nucleons themselves are made of quarks, one can ask if the quark substructure of the nucleon plays any role in the structure of nuclei. The usual assumption is that the long-range attractive force between nucleons is indeed dominated by pion exchange between the nucleons, but the short range repulsive force is likely to be better described with quark and gluon degrees of freedom. Then, to search for quark effects in nuclei, one has to examine phenomena sensitive to the short-range, and thus high-momentum, part of the nuclear wave function. Thus, one wishes to study short-range correlations between nucleons. This study has only really become possible in recent years, as we now have the ability, for light nuclei, to make predictions based on the nucleon-nucleon force.

Even in a standard shell-model calculation of nuclear structure, in which a nucleon might be viewed as an independent particle moving in an average potential, one needs additional two-body forces to account for the properties of nuclear levels. Furthermore, if one has two particles in a nucleus, the wave function of the two particles can be transformed into a center-of-mass wave function times a relative wave function, which reflects the correlations between the two nucleons. So conventional models always have correlations between two particles, and to find quark effects, we need to identify in data that there are effects of correlations, that these correlations are short range, and that quark models, but not conventional nucleon-nucleon forces, can be used to explain these correlations.

There is a long history of experimental interest in two-nucleon correlations. It has been a motivation for the study of many interactions that necessarily involve two nucleons, such as (e,e′NN) and (π^+,π^-) reactions. However, there is a lack of definitive results concerning two-nucleon correlations due to additional reaction mechanism effects that obscure the correlation physics. There are always problems at some level with nucleons rescattering with the nucleus, and with meson-exchange currents and isobar excitation.

Attention in recent years has shifted to (e,e′p) and (e,e′NN) reactions on few body nuclei. Modern nucleon-nucleon potentials generate excellent wave functions and accurate descriptions of nuclear properties. On the experimental side, the modern generation of high-current, continuous-beam accelerators allows the studies to be carried out to very high values of missing momentum, well above the $\approx$ 200 MeV/c Fermi momentum of light nuclei, so that one knows nucleon-nucleon correlations must be important. The experiment described here, ^{3}He(e,e′p), takes advantage of these theoretical and experimental advances to provide one of the most discriminating tests to date of the ability to describe nuclei in terms of hadronic degrees of freedom, or alternately the need to use quark degrees of freedom to describe nuclear properties.

1.1 Electron Scattering

Electron scattering is one of the most powerful tools used in the exploration of nuclear matter. The electromagnetic interaction is well described by the Quantum Electro-Dynamics (QED), where the beam electron exchanges a virtual photon with the target nucleus; this approach is called one photon exchange approximation. The electromagnetic interaction is relatively weak compared to the hadronic interaction and the resulting virtual photon can probe the entire nuclear volume, in contrast to hadronic probes that mostly sample the nuclear surface. In contrast to real photon probes, in which the energy and momentum transfer are fixed, electron scattering allows one to vary the energy and momentum transfer individually.

During the past few decades, a wealth of information has been obtained on the single particle aspects of nuclear structure, in particular through elastic, inelastic $(\mathrm{e}, \mathrm{e}')$ and quasielastic $(\mathrm{e}, \mathrm{e}'\mathrm{p})$ electron scattering experiments. These results have led to strong constraints on the self-consistent mean field description of nuclei, and it is fair to say that the one-body properties of nuclei are now well under control.

- By increasing the momentum transfer, one can probe the spatial structure of nuclei over distances comparable to or smaller than the nucleon size, where short range correlations between two or several nucleons are important. These correlations are poorly known, and their determination is one of the major goals of modern nuclear physics.

- At high momentum transfer, the internal structure of hadrons cannot be ignored. Indeed, the study of the interplay of mesonic and nucleonic degrees of freedom with those of their constituents, using the nucleus as a laboratory, is also a fundamental objective. How is a nucleon affected by the presence of close neighbors in the nuclear medium? Is there a distance below which it loses its identity within a large quark cluster?

Experimental studies of electromagnetically induced two-body and three-body breakup of the three-nucleon system have mainly been performed on ^{3}He, because of the experimental difficulties associated with the use of tritium. The experiments included the electron-induced two-body breakup reaction channel $^3\mathrm{He}(\mathrm{e},\mathrm{e}'\mathrm{p})\mathrm{d}$ [1, 2, 3, 4, 5], and two-body break-up experiments of the type $^3\mathrm{He}(\mathrm{e},\mathrm{e}'\mathrm{d})\mathrm{p}$ have also been performed [2, 6, 7, 8]. In these experiments, the proton momentum distributions in ^{3}He were obtained up to 500 MeV/c. Although the cross section is strongly influenced by contributions from meson-exchange and final state rescattering, signatures of NN correlations were observed in these studies for momenta above 300 MeV/c. The proton-proton density distribution was extracted for relative momenta from 200 to 550 MeV/c in a model-dependent analysis of inclusive (e,e') data by Beck [9].

Coincidence experiments have proven to be very useful tools to study specific aspects of the nucleus. In particular, the $(\mathrm{e},\mathrm{e}'\mathrm{p})$ reaction has been used not only to explore the single nucleon structure of nuclei, but also to study the behavior of nucleons embedded in the nuclear medium.

The high energy, high duty cycle beam of Jefferson Lab allows one to fully develop such studies by:

- extending the domain of momentum transfer towards higher values where short range effects and possibly the internal structure of the nucleons are manifested,
- exploring nuclear structure in extreme conditions, by focusing on the high momentum part of the wave functions, and
- increasing the specificity of the probe by separating the response functions associated with different polarization states of the virtual photons.

The E89044 experiment in Hall A of Jefferson Lab exploited these possibilities by undertaking a series of $(\mathrm{e},\mathrm{e}'\mathrm{p})$ measurements on ^{3}He.

The $(\mathrm{e},\mathrm{e}'\mathrm{p})$ reaction formalism was first developed in references [10, 11, 12, 13, 14]. A brief review of the formalism is presented below; for more details the reader is referred to a review of $(\mathrm{e,e'p})$ by J. Kelly [15]. The kinematic variables are defined below, and the most general cross section is given in the formalism of the plane wave Born approximation (PWBA). The proton momentum density distribution is defined, and the kinematical settings are presented.

1.2 $^3\mathrm{He}(\mathrm{e,e'p})$ Kinematics

We describe, in the laboratory coordinate system, the kinematics of coincidence $(\mathrm{e,e'p})$ detection using the standard notation of the total energies and the three-momenta of the participant particles in the reaction; see Fig. 1.1:

- incident electron: $k_i = (E_i, \vec{k}_i)$,
- detected electron: $k_f = (E_f, \vec{k}_f)$,
- detected proton: $p_p = (E_p, \vec{p}_p)$,
- target nucleus: $p_A = (E_A, \vec{p}_A)$,
- undetected residual system: $p_B = (E_B, \vec{p}_B)$,
- virtual photon: $q = (\omega, \vec{q})$.

In the present experiment, the momentum of the incident and scattered electrons and of the knocked out proton are measured, so that $\vec{k}_i$, $\vec{k}_f$ and $\vec{p}_p$ are known. In ^{3}He(e,e′p) coincidence measurements, the experimentally determined quantities are $\vec{k}_i$, $\vec{k}_f$ and $\vec{p}_p$. The total energy of the detected proton E_p is obtained with $E_p = \sqrt{M_p^2 + p_p^2}$, where M_p is the proton rest mass. The electrons are ultra-relativistic (i.e. $\mathrm{k_i \gg m_e}$), so that $E_i \approx |\ \vec{k}_i\ |$ and $E_f \approx |\ \vec{k}_f\ |$. Additionally, in the laboratory frame, the initial momentum of the target ^{3}He nucleus is neglected so that $p_A = (M_A, \vec{0})$, where M_A is the rest mass of the ^{3}He nucleus.

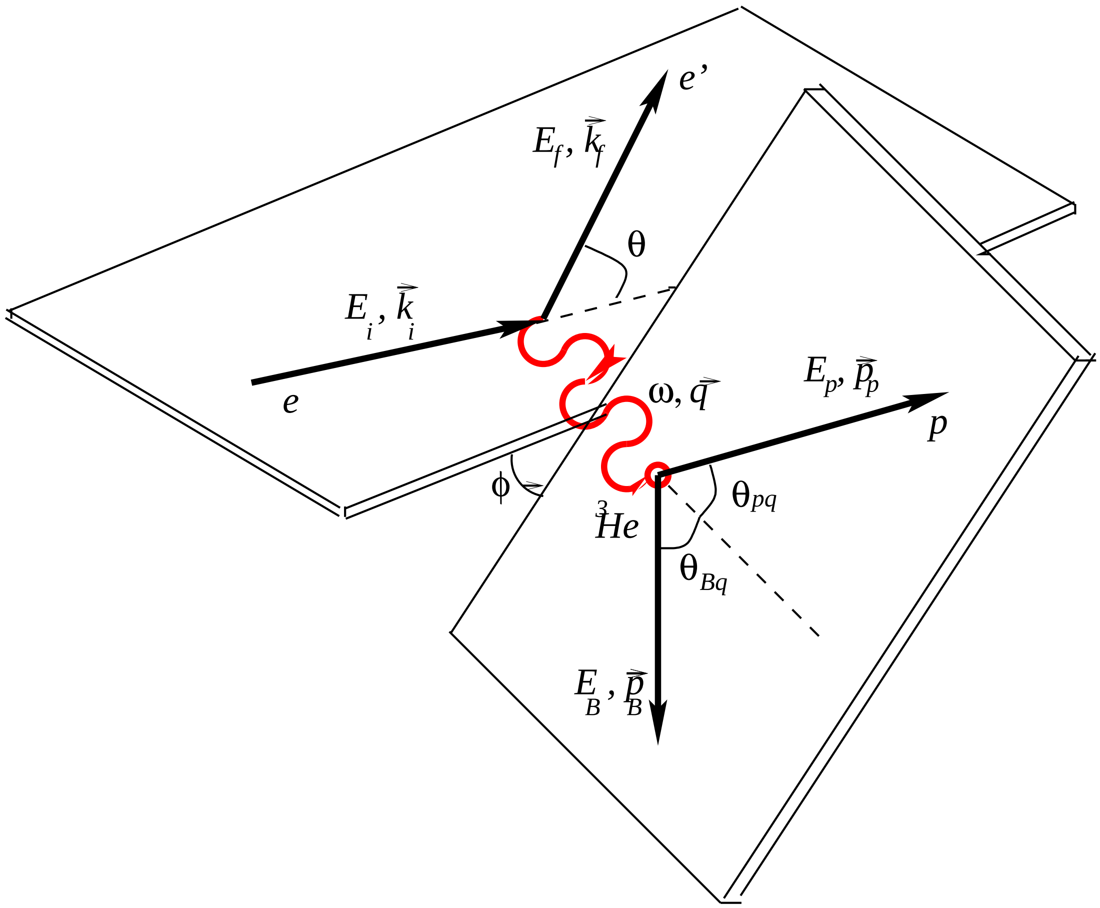

Figure 1.1: Kinematic definitions for the $(\mathrm{e}, \mathrm{e}'\mathrm{p})$ reaction.

The four-momentum of the virtual photon is calculated from momentum and energy conservation

$$q = k_i - k_f = (\omega, \vec{q}). \tag{1.1}$$

with $\omega = E_i - E_f$ and the three momentum transfer $\vec{q} = \vec{k}_i - \vec{k}_f$.

We adopt the notation $Q^2 = -q^2 \geq 0$, for our space-like electron scattering reaction.

The scattering plane is defined by $\vec{k}_i$ and $\vec{k}_f$. The reaction plane is defined by $\vec{q}$ and $\vec{p}_p$. The angle between the reaction plane and the scattering plane is defined to be the out-of-plane angle, ϕ. Since detection of the proton at ϕ = 0 or ϕ = 180^o corresponds to a measurement in the scattering plane, these measurements are called "(nearly) in-plane kinematics". All the measurements presented in this thesis correspond to in-plane kinematics. The angle of the detected proton with respect to $\vec{q}$ is θ_{pq}. Detection of the proton along $\vec{q}$, θ_{pq} = 0, corresponds to "parallel kinematics". If $\vec{p}$ is not parallel to $\vec{q}$, the setting is called perpendicular kinematics.

The three momentum of the recoil system, $\vec{p}_B$, can be calculated by applying momentum conservation at the reaction vertex:

$$\vec{p}_B = \vec{q} - \vec{p}_p \tag{1.2}$$

We define the missing momentum of the reaction to be the momentum we did not measure during the reaction. It is equal to $\vec{p}_B$,

$$\vec{P}_m = \vec{p}_B = \vec{q} - \vec{p}_p \tag{1.3}$$

The excitation energy of the system is given by the missing energy E_m; it is the difference between the transferred energy and the sum of the energies of the knocked out proton and the recoil system. It is given by:

$$E_m = \omega - T_p - T_B, \tag{1.4}$$

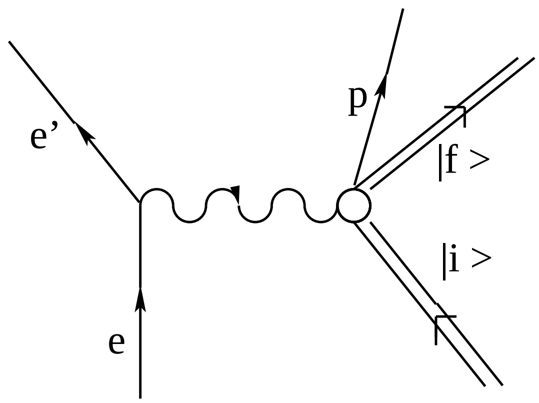

Figure 1.2: One photon exchange approximation.

and also given by:

$$E_m = \omega - (\sqrt{p_p^2 + M_p^2} - M_p) - (\sqrt{p_B^2 + M_B^2} - M_B). \quad (1.5)$$

where M_B is the mass of the recoil system.

1.3 Plane Wave Born Approximation (PWBA)

In the plane wave Born approximation (PWBA), the incident and scattered electrons are described by Dirac plane waves and the interaction with the nucleus is mediated by one single virtual photon [1]as illustrated in Fig. 1.2.

In this approximation, the six-fold differential cross section for the $(\mathrm{e}, \mathrm{e}'\mathrm{p})$ reaction is given by:

$$\frac{d^6\sigma}{d\omega d\Omega_e dE_p d\Omega_p} = K\sigma_M(R_T + \epsilon R_L + \sqrt{\epsilon(1+\epsilon)}R_{TL}\cos\phi + \epsilon R_{TT}\cos 2\phi) \quad (1.6)$$

where

[1]The largest term in calculating the $(\mathrm{e}, \mathrm{e}'\mathrm{p})$ cross section is the one corresponding to the exchange of a single virtual photon. Higher order terms contain more than one photon, and are suppressed due to the weakness of the electromagnetic coupling constant.

- K is a kinematic factor, $p_p{}^2/2\|$,
- $\sigma_{\mathrm{M}} = \frac{\alpha^2}{4\mathrm{E_0}^2}\frac{\cos^2(\theta/2)}{\sin^4(\theta/2)}$ is the Mott cross section, which describes the scattering of a relativistic electron on a point-like target particle.
- $\epsilon = \left[1 + 2\frac{|\tilde{q}^2|}{Q^2}\tan^2\frac{\theta}{2}\right]^{-1}$ is the polarization of the virtual photon. [2]

The four independent response functions $\mathrm{R_L}$, $\mathrm{R_T}$, $\mathrm{R_{LT}}$ and $\mathrm{R_{TT}}$ contain all the information that can be extracted from the hadronic system using the $(\mathrm{e}, \mathrm{e'p})$ reaction. They are related to the components of the hadronic current J = $(\rho, \vec{J})$ by the relations:

- $\mathrm{R_L} =< \rho\rho^+ >$
- $\mathrm{R_T} = < \mathrm{J_{||}J_{||}^+} + \mathrm{J_\perp J_\perp^+} >$
- $\mathrm{R_{LT}}\ \cos\phi = - < \rho\mathrm{J_{||}^+} + \mathrm{J_{||}}\rho^+ >$
- $\mathrm{R_{TT}}\cos 2\phi =< \mathrm{J_{||}J_{||}^+} - \mathrm{J_\perp J_\perp^+} >$

where $\mathrm{J_{||}}$ and $\mathrm{J_\perp}$ are perpendicular to the momentum transfer $\vec{q}$ in the scattering plane and perpendicular to the scattering plane respectively.

1.4 Plane Wave Impulse Approximation (PWIA)

In the plane wave impulse approximation (PWIA) the total energy and momentum of a single virtual photon is absorbed by a single nucleon while the other nucleons stay spectators, as shown in Fig.1.3.

In this approach, the outgoing nucleon leaves the nucleus without interacting with the rest of the nucleons and may be represented by a plane wave. This nucleon is the one detected in a coincidence experiment.

Applying momentum conservation at the photon-proton vertex, the initial proton momentum, $\vec{p_i}$, is given by:

---

[2]The polarization ϵ is defined only for virtual photons; real photons are characterized by $Q^2 = 0$.

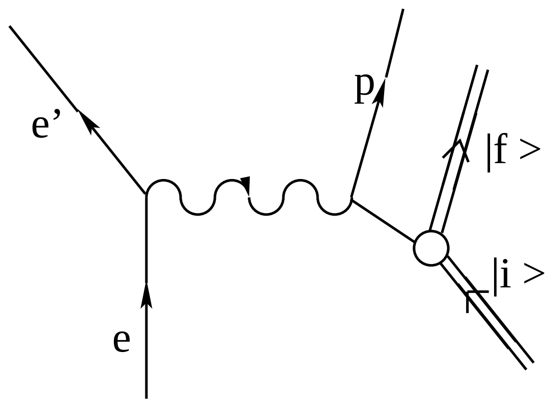

Figure 1.3: One photon exchange approximation.

$$\vec{p}_i = \vec{p}_p - \vec{q}. \tag{1.7}$$

Comparing the equations 1.7 and 1.3 , one can see that the initial proton momentum is related to the missing momentum, $\vec{P}_m$, of the reaction by:

$$\vec{p}_i = -\vec{P}_m \tag{1.8}$$

By measuring the missing momentum in an $(\mathrm{e}, \mathrm{e}'\mathrm{p})$ experiment, one can therefore determine the initial momentum that the struck proton had inside the nucleus before the scattering occurred. Note that this interpretation is only valid in the framework of the PWIA.

The $(\mathrm{e}, \mathrm{e}'\mathrm{p})$ cross section in the PWIA is given by:

$$\frac{d^6\sigma}{d\omega d\Omega_e dE_p d\Omega_p} = p_p^2 \times \sigma_{ep} \times S(P_m, E_m) \tag{1.9}$$

where σ_{ep} is the off-shell electron-proton cross section. $S(P_m, E_m)$ is the spectral function, and represents the probability of finding a proton of momentum P_m and energy E_m inside the nucleus.

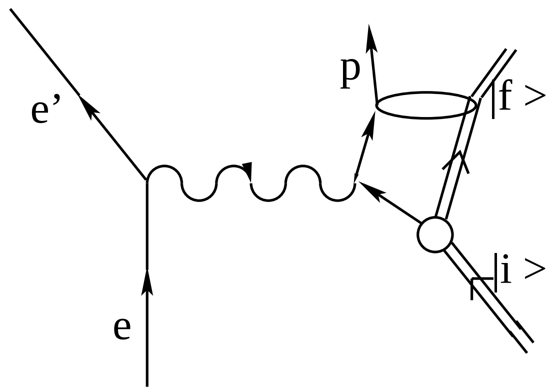

Figure 1.4: Distorted Wave Impulse Approximation.

1.5 Distorted Wave Impulse Approximation (DWIA)

In this approximation, the ejected nucleon interacts with the residual nucleus via the strong interaction. The distorted wave impulse approximation (DWIA) takes final states interactions (FSI) into account, while at the same time maintaining the other assumptions of the PWIA. Figure1.4 represents the diagram for the DWIA.

In the DWIA, the FSI are usually addressed using an optical potential to derive the distorted wave for the ejected nucleon. The optical potentials are obtained from fits to elastic nucleon-nucleus scattering data. A description of the optical potential formalism may be found in Ref. [16]

1.6 $^3\mathrm{He(e,e'p)pn}$ Reaction and Nucleon-Nucleon correlations

Exclusive $(\mathrm{e,e'p})$ measurements can provide information on the spatial structure of nuclei at a resolution less than the size of the nucleons, where correlations between two or more nucleons are expected to be significant. By choosing appropriate kinematics one can separate the effect of nucleon-nucleon correlations from the effects of final-state interactions (FSI) and other reaction-mechanism effects. Understanding correlations, particularly short-range correlations, might require consideration of the underlying quark substructure of the nucleon.

In this section we present two signatures of NN correlations in ^{3}He that one might expect to observe in the $(\mathrm{e}, \mathrm{e}')$ reaction. Consider an electron which scatters on a proton belonging to a pair of correlated nucleons inside a nucleus, ^{3}He in our case [17, 18], transferring energy ω and momentum $\vec{q}$. In the center of mass system of the two nucleons, these nucleons will have equal and opposite momenta, $\pm\vec{P}_m$, which will be large if they are close together. In the plane-wave impulse approximation (PWIA) - see Fig. 1.6a - the interaction between the outgoing nucleon and the residual nuclear fragments is neglected. If we further neglect the momentum of the pair relative to the residual nucleus (here a single nucleon), the struck proton is ejected with momentum $\vec{q} - \vec{P}_m$, while the other nucleon of the pair moves off with the recoil momentum of the reaction, $\vec{P}_m$. The spectator nucleon is at rest, so this is the three-body breakup (3bbu) reaction channel, as opposed to the two-body breakup (2bbu) channel with a pd final state, see Fig. 1.5. The spectator nucleon and the undetected nucleon of the pair constitute a recoil system of mass:

$$M_r^2 = \left[M_{A-2} + \sqrt{M_N^2 + P_m^2} \right]^2 - P_m^2 \,. \tag{1.10}$$

Here M_N is the mass of the undetected nucleon and M_{A-2} is the mass of the $A-2$ nuclear system.

Thus, in PWIA, a signature of the disintegration of correlated nucleons is the appearance of a peak in the cross section as a function of missing energy, E_m, in the continuum region, with the position depending on P_m: $E_m = M_r + M_p - M_A$. The correlation peak was observed for the first time in [3]. The peak width reflects the motion of the center of mass with respect to the spectator nucleon and its magnitude is directly related to the wave function of the two correlated nucleons. The peak thus signifies the absorption of virtual photons on nucleons correlated in pairs, as in the electro-disintegration of deuterons. This picture remains valid even if the two nucleons of the correlated pair reinteract - see Fig. 1.6b.

In PWIA, the integral over the continuum gives the momentum distribution of the proton in the pair. The integral is obtained experimentally by dividing the experimental cross section by the elementary off-shell electron-proton cross section σ_{ep} [19] multiplied by a kinematic factor K, and integrating over missing energy:

$$\eta(P_m) = \int \Big(\frac{d^6\sigma}{dE_f dE_p d\Omega_e d\Omega_p} \, / \, K\sigma_{ep} \Big) \; dE_m \tag{1.11}$$

The momentum distribution will yield a second signature of NN correlations. One might expect that NN correlations lead preferentially to 3bbu rather than 2bbu, due to the reduced probability for the two undetected nucleons to form a bound deuteron. Thus, the signature is that as NN correlations become important at missing momenta greater than the Fermi momentum, the momentum distribution from 3bbu will be enhanced relative to that for 2bbu.

This simple picture is complicated by several factors, so that data must be compared to detailed calculations before drawing conclusions about NN correlations in nuclei. First, the peak in the missing energy has a purely kinematic origin, in that it will appear as long as the ^{3}He electrodisintegration involves two active nucleons plus a spectator nucleon. Second, the effective momentum density distribution is an actual density only in the PWIA limit. This picture is modified by final-state interactions and meson-exchange currents (MEC). When the two nucleons in the active pair rescatter, the position and width of the peak do not change. But one measures the transition between a correlated pair in the ground state and a correlated pair in the continuum. When one of the nucleons of the active pair reinteracts with the spectator third nucleon - see Fig. 1.6c - the position, shape, and amplitude of the peak might all be affected.

In Thomas Jefferson National Accelerator Facility (JLab) Hall A experiment E89-044 [20], we studied the $^3\mathrm{He(e, e'p)pn}$ reaction in the quasielastic region at transferred 3-momentum $|\vec{q}|$ = 1501 MeV/c and energy ω = 840 MeV, so Q^2 = 1.55 GeV^2. This thesis reports the results of measurements in perpendicular kinematics with Bjorken x = $\mathrm{Q^2/(2M_p\,\omega)}$ = 0.96, near the top of the quasifree peak (Bjorken x = 1). Protons were detected at several angles relative to $\vec{q}$, corresponding to missing momenta P_m of 0 - 1 GeV/c.

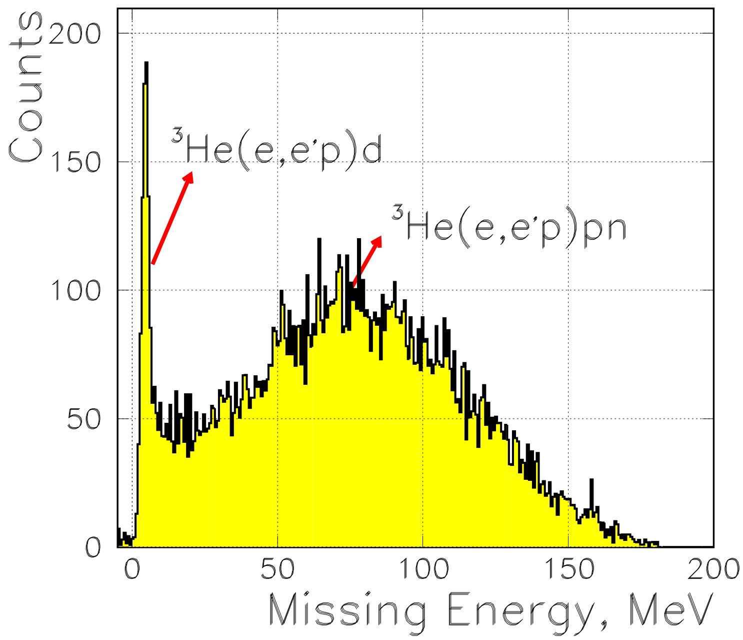

Figure 1.5: Missing energy spectrum for the $^3\mathrm{He}(\mathrm{e}, \mathrm{e}'\mathrm{p})$ reaction at P_m = 550 MeV/c.

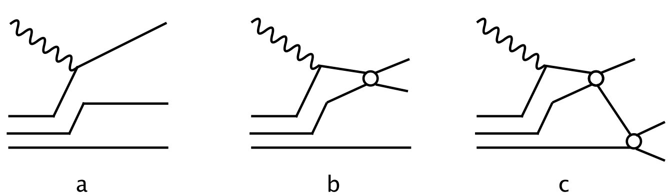

Figure 1.6: Feynman diagrams for a) PWIA, b) rescattering, and c) rescattering with the spectator nucleon.

1.7 Experimental spectral function

An experimental spectral function can be determined by dividing the measured $(\mathrm{e},\mathrm{e}'\mathrm{p})$ cross section by the appropriate factor,

$$S^{exp}(P_m, E_m) = \frac{1}{p_p^2\sigma_{ep}} \times \frac{d^6\sigma}{d\omega d\Omega_e dE_p d\Omega_p}\,. \tag{1.12}$$

This requires a model of the off-shell electron-proton cross section, σ_{ep}. We use the CC1 prescription of de Forest [19], which is commonly used by others (see [21] and [5] for example). The model of σ_{cc1} used in this thesis uses the parametrization of Simon $et\ al.$ [22] of the free-nucleon form factors. The cross section σ_{ep} is given by [3]

$$\sigma_{ep} = \sigma_M\left[\frac{Q^4}{|\vec{q}|^4}\,W_C + \tau^2\,W_T + \frac{Q^2}{|\vec{q}|^2}\tau\,W_I\cos\phi + \tau^2\,W_S\right]. \tag{1.13}$$

where $\tau = \sqrt{\frac{Q^2}{|\vec{q}|^2} + \tan^2\frac{\theta}{2}}$ and the W's are given by

$$W_c = \frac{1}{4\bar{E}E_f}\left[(\bar{E}+E_f)^2\left(F_1^2 + \frac{Q^2}{4m^2}\kappa^2F_2^2\right) - |\vec{q}|^2(F_1+\kappa F_2)^2\right], \tag{1.14}$$

$$W_T = \frac{Q^2}{2\bar{E}E_f}(F_1+\kappa F_2)^2 \tag{1.15}$$

$$W_S = \frac{p'^2}{\sin^2\gamma}\bar{E}E_f\left[(\bar{E}+E_f)^2\left(F_1^2 + \frac{Q^2}{4m^2}\kappa^2F_2^2\right)\right], \tag{1.16}$$

$$W_I = -\frac{p'^2}{\sin\gamma}\bar{E}E_f(\bar{E}+E_f)\left[(\bar{E}+E_f)^2\left(F_1^2 + \frac{Q^2}{4m^2}\kappa^2F_2^2\right)\right]. \tag{1.17}$$

where $\bar{E} = \sqrt{p^2+m^2}$, with p the initial momentum of the struck proton and m the mass of the proton. The anomalous magnetic moment of the proton is κ; it is related

[3]Note that if the proton were free and point-like particle, σ_{ep} in Eq. 1.13 would be equal to the Mott cross section

to the magnetic moment of the proton by $\kappa = \mu_p - 1 = 1.793$. F_1 and F_2 are the Dirac and Pauli form factors of the proton, respectively. They are given in terms of the electric and magnetic Sachs form factors, G_E and G_M

$$F_1(Q^2) = \frac{G_E(Q^2) + \tau G_M(Q^2)}{1+\tau} \tag{1.18}$$

$$F_2(Q^2) = \frac{G_E(Q^2) - \tau G_M(Q^2)}{1+\tau} \tag{1.19}$$

If PWIA is valid, then the experimental spectral function determined from the measured $(\mathrm{e}, \mathrm{e}'\mathrm{p})$ cross section should be equal to the theoretical spectral function, $S^{exp}(P_m, E_m) = S(P_m, E_m)$. Furthermore, in PWIA the spectral function is only a function of P_m and E_m, so that measurements of S^{exp} at different kinematics should yield the same result if P_m and E_m are fixed.

1.8 Overview of kinematic settings

The $^3\mathrm{He}(\mathrm{e}, \mathrm{e}'\mathrm{p})\mathrm{pn}$ kinematical settings of the experiment analysed in this thesis are presented in Table 1.1. The data were collected at two values of the beam energy, 4.8068 GeV and 1.2553 GeV. At each beam energy, scattered electrons were detected by the Hall A electron spectrometer, set at a fixed scattering angle and momentum corresponding to the quasi-elastic knockout of protons with transferred momentum $|\vec{q}| = 1.5$ GeV/c and energy $\omega =$ 837 MeV.

In coincidence with the scattered electron, the knocked out proton was detected by the Hall A hadron spectrometer, in perpendicular coplanar (e,e′p) kinematics. With $\vec{q}$ and ω fixed and coplanar detection of the knocked out proton, the requirement of observing the ^{3}He(e,e′p)d reaction provides a relationship between the angle and momentum of the detected proton. The central angle and momentum of the hadron spectrometer were varied while in fact keeping the ^{3}He(e,e′p)d reaction within the spectrometer acceptance, thus providing ^{3}He(e,e′p)d measurements over a range of momentum of the undetected recoil.

Table 1.1: Perpendicular kinematic settings analyzed in this thesis. Given are nominal values of spectrometer settings, beam energies and other kinematic parameters.

Run #	Kin	$\tilde{q}$ (GeV/c)	E_{beam} (GeV)	ω (GeV)	ϵ	P_m (GeV/c)	E_e (GeV)	θ_e (deg)	P_p (GeV/c)	θ_p (deg)	t (hr)
4	Σ_1	1.50	4.8068	0.837	0.943	0.150	3.966	16.40	1.493	54.04	0.9
5	Σ_2	1.50	4.8068	0.837	0.943	0.150	3.966	16.40	1.493	42.56	0.7
6	Σ_3	1.50	1.254	0.837	0.108	0.150	0.417	118.72	1.493	19.87	3.4
7	Σ_1	1.50	4.8068	0.837	0.943	0.300	3.966	16.40	1.472	59.83	10.1
8	Σ_2	1.50	4.8068	0.837	0.943	0.300	3.966	16.40	1.472	36.76	6.6
9	Σ_3	1.50	1.254	0.837	0.108	0.300	0.417	118.72	1.472	25.67	33.3
10	Σ_1	1.50	4.8068	0.837	0.943	0.425	3.966	16.40	1.444	64.76	19.9
11	Σ_2	1.50	4.8068	0.837	0.943	0.425	3.966	16.40	1.444	31.84	15.5
12	Σ_3	1.50	1.254	0.837	0.108	0.425	0.417	118.72	1.444	30.59	64.6
13	Σ_1	1.50	4.8068	0.837	0.943	0.550	3.966	16.40	1.406	69.80	35.2
14	Σ_2	1.50	4.8068	0.837	0.943	0.550	3.966	16.40	1.406	26.79	42.8
15	Σ_3	1.50	1.254	0.837	0.108	0.550	0.417	118.72	1.406	35.63	122.
28	Σ_1	1.50	4.8068	0.837	0.943	0.750	3.966	16.40	1.327	78.28	23.0
29	Σ_1	1.50	4.8068	0.837	0.943	1.000	3.966	16.40	1.171	89.95	23.0

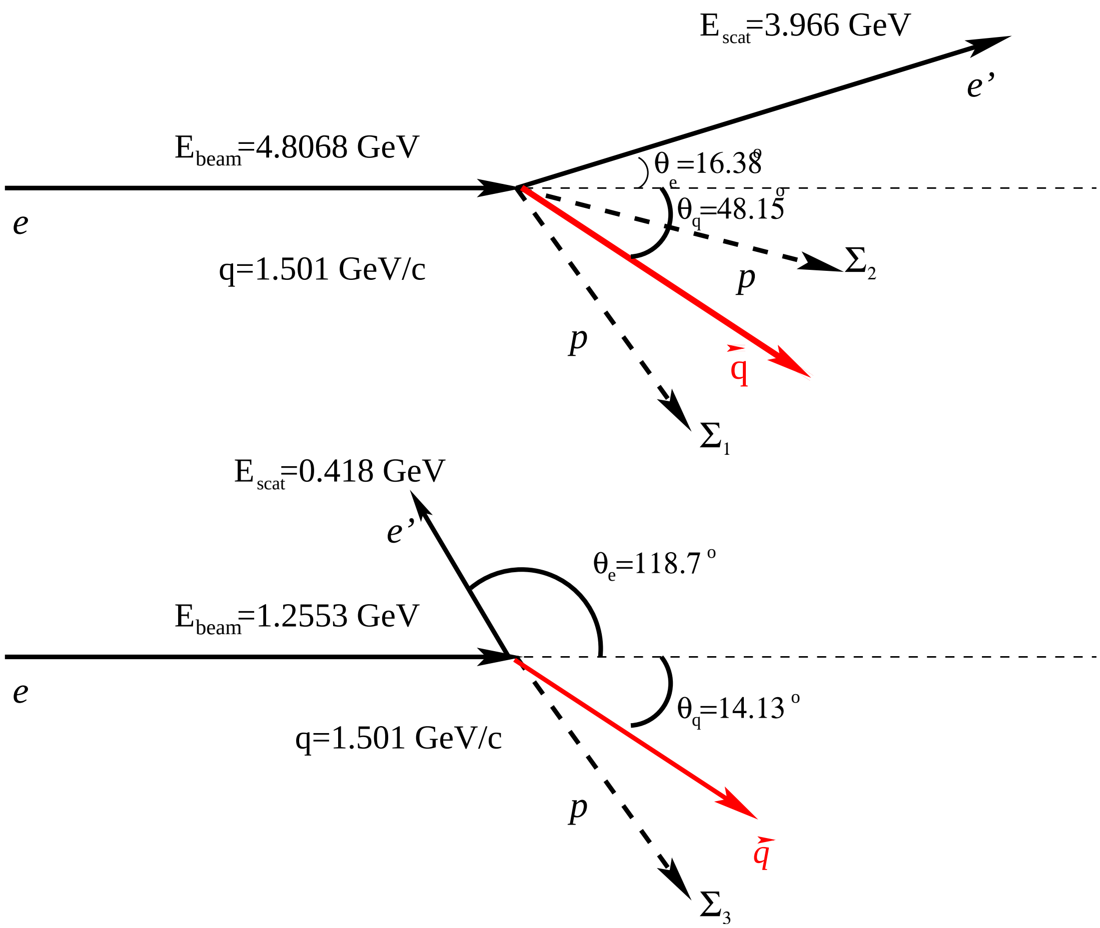

Figure 1.7: Graphical view of kinematic settings analyzed in this thesis. Given are actual beam energies and central angles and momenta of the electron spectrometer.

Table 1.2: Missing momentum ranges of measured $^3\mathrm{He(e,e'p)d}$ and $^3\mathrm{He(e,e'p)pn}$ cross sections.

Kinematics	Beam energy (GeV)	Forward/backward of $\vec{q}$	P_m range (MeV)
Σ_1	4.8	backward	0 – 1000
Σ_2	4.8	forward	0 – 550
Σ_3	1.2	backward	0 – 550

This thesis uses both a digit and a letter notation to designate ^{3}He(e,e′p) kinematic settings. The digit notation, kinematics i, refers to an angle and momentum setting of both electron and hadron spectrometers, and is defined in the first column of Table 1.1. The letter notation (Σ_1, Σ_2, and Σ_3) is used to designate a beam energy, and whether the proton was detected forward (closer to the beam dump) or backward with respect to the momentum transfer $\vec{q}$. The letter notation is defined in the second column of Table 1.1.

The ^{3}He(e,e′p)pn data are extracted up to $E_m = 140$ MeV in this thesis. Covered ranges of P_m at each beam energy are given in Table 1.2.

Data collected at Σ_1 and Σ_2 settings were used for the extraction of the transverse-longitudinal asymmetry A_{TL}. The ^{3}He(e,e′p)d analysis was the thesis subject of Marat Rvachev [23]. The ^{3}He(e,e′p)d parallel kinematics data collected by the E89044 experiment are the subject of a thesis by Emilie Penel-Notaris [24].

Chapter 2

Experimental Setup

The E89044 experiment was performed in Hall A at the Thomas Jefferson National Accelerator Facility (TJNAF), known also as CEBAF (Continuous Electron Beam Accelerator Facility). The data taking phase took place from December 1999 to May 2000. This was a coincidence experiment, with the scattered electrons detected in the electron arm High Resolution Spectrometer (HRSe) and the knocked out proton detected in the Hadron High Resolution Spectrometer (HRSh).

2.1 Jefferson Lab

The world's premier medium energy scattering laboratory, Jefferson Lab, consists of a state-of-the-art continuous wave electron accelerator, with three complementary experimental halls, A, B and C, that use the beam to explore different aspects of nuclear physics, a free electron laser facility, and an applied research center.

The CEBAF accelerator at Jefferson Lab is capable of delivering high quality continuous electron beams up to 5.7 GeV as of the date of writing this thesis. Future plans include upgrades to 12 GeV; the machine is eventually upgradable to 25 GeV. The accelerator site layout is shown in Fig. 2-1. The electron beam is produced at the injector by illuminating a photocathode, then accelerated to $45\ \mathrm{MeV}$ (for standard 4.045 GeV conditions). The beam is further accelerated in each of two superconducting linacs, through which it can be recirculated up to four times, each producing an energy gain of $800\ \mathrm{MeV}$ per pass. The beam can be extracted "simultaneously" to each of the three experimental halls, A, B and C. The current to each hall can be controlled independently. A linac contains 20 cryo-modules, each containing eight superconducting niobium cavities cooled by liquid helium at 2 K, with a design accelerating gradient of $5\ \mathrm{MeV/m}$. The design maximum current is 200 μA, which can be split arbitrarily between three interleaved $499\mathrm{MHz}$ bunch trains. One such bunch train can be peeled off after each linac pass to any one of the Halls using Radio-Frequency (RF) separators and septa. All Halls can simultaneously receive the maximum energy beam. Hall B with its CEBAF Large Acceptance Spectrometer (CLAS) requires currents as low as $1\ \mathrm{nA}$, while up to $120\ \mu\mathrm{A}$ currents are being delivered to one or even both of the other Halls. Hall C has been operational since November 1995. Hall A started taking data during May 1997; it was designed for programs requiring high precision measurements. Hall B has operated since December 1997; its almost 4π acceptance makes it an ideal device to study multi-particle final states.

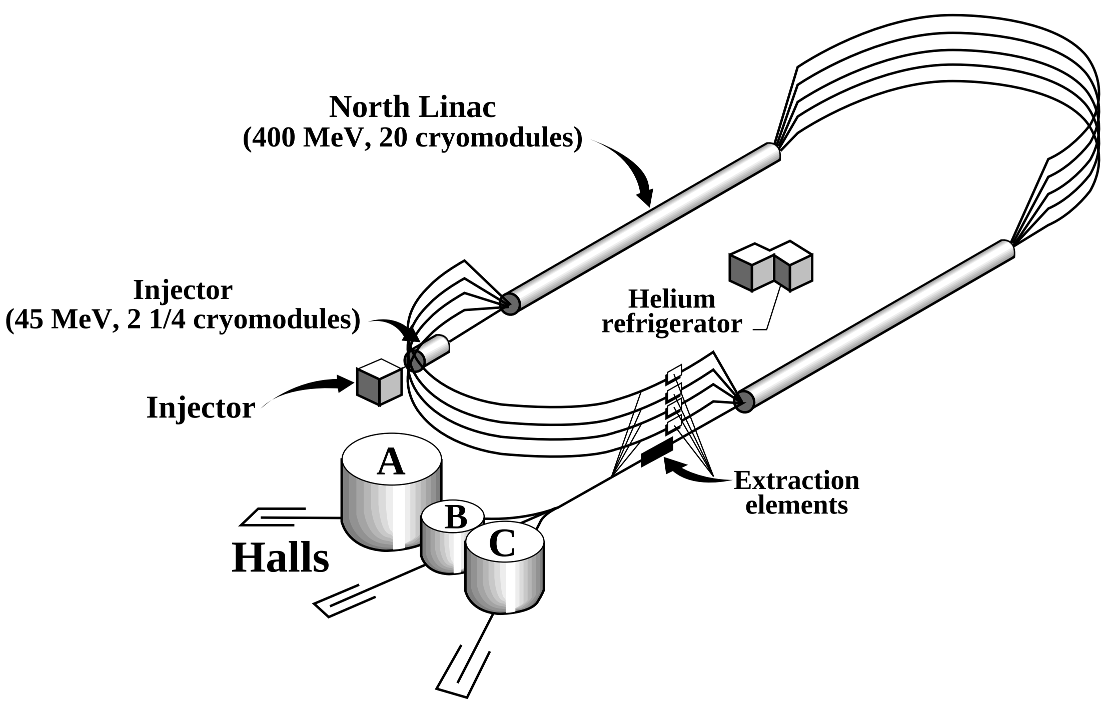

Figure 2.1: Layout of the Jefferson Lab accelerator site.

2.2 Hall A

Figure 2.2 shows a schematic layout of experimental Hall A. The hall is circular in shape and has a diameter of 53 m. The bulk of the volume of the hall is underground, well shielded to contain radiation with concrete and a thick layer of earth. The central elements are two High Resolution Spectrometers (HRS). Both of these devices provide a momentum resolution of better than 2×10^{-4} and a horizontal angular resolution of better than $2\ \mathrm{mr}$ at a design maximum central momentum of $4\ \mathrm{GeV/c}$. The present base instrumentation in Hall A [28] has been used with great success for experiments which require high luminosity and high resolution in momentum and/or angle for at least one of the reaction products.

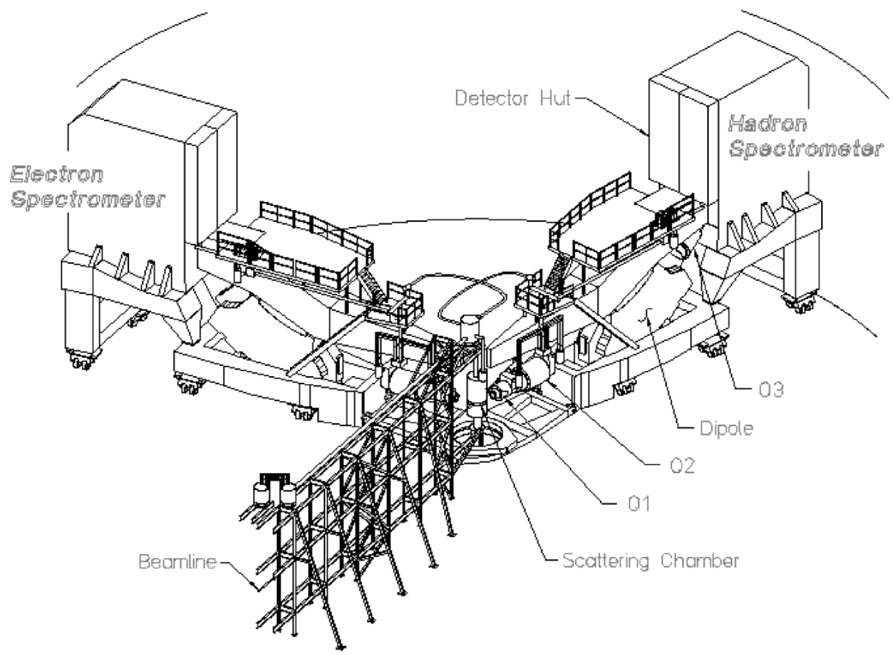

Figure 2.2: Schematic layout of Hall A.

2.3 Beamline

2.3.1 Beam Position Monitors (BPMs)

Two beam position monitors (BPMs) located 7.524 m and 1.286 m upstream of the nominal target center are used to determine the position and direction of the beam at the target location. During E89044, the beam position in the last two BPMs was read out 6 times per trigger, at intervals of 4 μs. This allowed precise tracking of the motion of the beam due to rastering for each event.

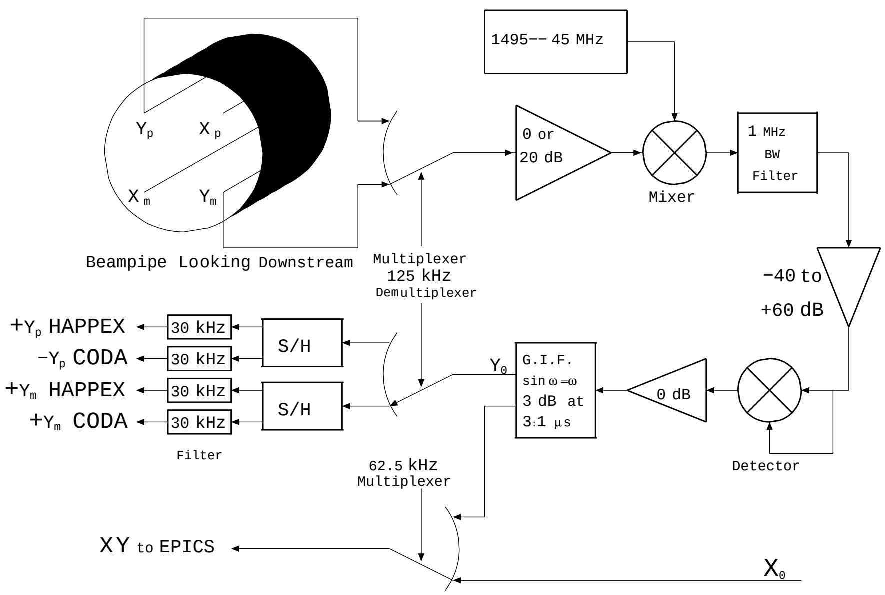

Figure 2.3: Beam position monitor readout electronics.

A wire (harp) scanner is used for precise measurements of the beam profile and position. It operates by moving differently-oriented wires across a low current beam and reading out the induced wire signals [25]. Harp scanners are positioned adjacent to each of the two last BPMs before the target, and are surveyed relative to the hall coordinates. They are used for calibration of the BPMs in a procedure called “bull’s eye”.

2.3.2 Beam Current Monitors (BCMs)

The beam current delivered to the hall is measured by two cylindrically shaped RF beam cavity monitors (BCM) 15.48 cm in diameter and 15.24 cm in length, placed 24.5 m upstream of the target. When the cavities are tuned to the frequency of the beam, their output voltage levels is proportional to the beam current. The output signal is amplified and split into two parts.

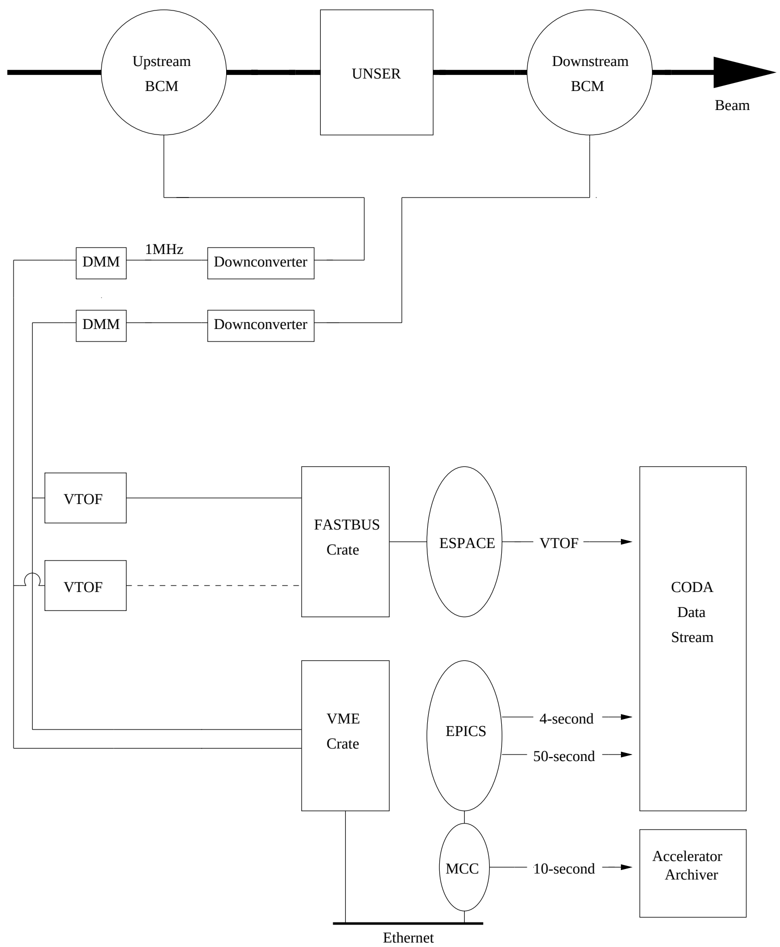

Figure 2.4: Block-diagram of BCM readout. Figure courtesy of Brian Diederich.

One part is sent to a high-precision digital AC voltmeter, which provides a measurement of the beam current averaged over 1 s periods. The other part of the signal is converted by an RMS-to-DC converter into an analog DC voltage level, which is then converted to a frequency signal by a V-to-F converter. This frequency signal is sent to scalers gated by the start and the end of each run, providing a measurement of the beam charge accumulated during the runs. Figure 2.4 shows a block-diagram of the Hall A implementation of the BCM readout.

2.3.3 Beam Energy Measurement

The absolute beam energy for Hall A is measured by two independent methods: the Arc method based in the beam deflection in a known magnetic field in the arc section of the beam line, and the eP method, based on elastic electron-proton scattering [26] Both methods can provide a precision of $\Delta E_{beam}/E_{beam} \approx 2 \times 10^{-4}$.

Table 2.1 summarizes the beam energy measured during the E89044 experiment with both methods.

Table 2.1: Absolute beam energy during the e89044 experiment.

Date	Pass	Arc Energy (MeV)	eP Energy (MeV)	$(\frac{\mathrm{eP}}{\mathrm{ARC}}) - 1)10^{-3}$
12/11/1999	1	842.57(16)	843.45(21)	1.0 $\pm$ 0.4
12/15/1999	5	4032.3(8)		
2/3/2000	3	2906.3(6)	2902.76(46)	-1.2 $\pm$ 0.4
2/6/2000	2	1954.8(4)	1956.15(43)	0.7 $\pm$ 0.4
2/10/2000	2	1954.2(4)	1955.96(43)	0.9 $\pm$ 0.4
2/14/2000	5	4806.8(9)	4809.0(2.7)	0.5 $\pm$ 0.7
2/20/2000	5		4805.15(3)	
3/4&3/2000	1	644.54(13)	645.03(25)	0.8 $\pm$ 0.6
3/5&9/2000	2	1255.0(2)	1255.89(30)	0.7 $\pm$ 0.4
3/28&29/2000	2	1255.3(2)	1255.6( )	0.2 $\pm$ 0.4
4/2/2000	5	3085.8(6)	3083.5(3)	-0.7 $\pm$ 0.4
5/5&6/2000	4	4237.5(20)	4240.4(9)	0.7 $\pm$ 0.7
5/23/2000	4	4530.6(9)	4530.56(50)	0 $\pm$ 0.4
6/20/2000	4	4531.0(10)	4531.1(10)	0 $\pm$ 0.4

Arc Measurement

The arc measurement is based on the principle that an electron in a constant magnetic field has a circular trajectory; its radius depends on the magnitude of the magnetic field and the electron's momentum. The Arc method was developed by a group of Saclay; it measures the deflection of the beam in the section of the beam line between the beam switch-yard and the hall entrance.

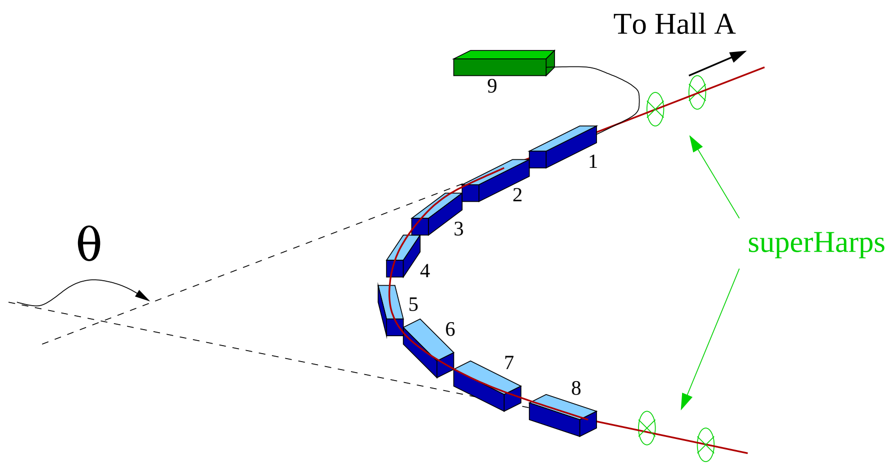

Figure 2.5: The arc section of the beamline

Figure 2.5 presents the setup used for the arc measurement. Two measurements of the magnetic field integral, $\int \tilde{\mathrm{B}} \cdot \mathrm{d}\tilde{\mathrm{l}}$ are made in a ninth reference dipole, relative to which the eight arc dipoles are calibrated with field maps. Measurements are also made of the bend angle, θ, of the beam of the arc based on a set of wire scanners called superHarps. The superHarps are moved across the beam path. When the beam strikes a wire, the particles scattering off the wire are collected by a simple ion chamber, hence a current is generated and the beam position is recorded.

The electron momentum can be calculated by:

$$p = c.\frac{\int_0^l \vec{B} \cdot d\vec{l}}{\theta} \tag{2.1}$$

where c = 0.299792 is the speed of light in units of $\mathrm{GeV\ rad/Tm}$, and θ is the deflection angle (see Fig. 2.5)

eP Measurement

This method was developed by the Université Blaise Pascal group. The eP method utilizes a stand-alone device along the beam-line located 17 m upstream of the target.

The device measures the resulting angles of the ejected electron, θ_e, and the recoil proton, θ_p, during the elastic scattering of the beam on protons in a CH_2 target. A schematic diagram of the eP energy measurement system is shown in Fig. 2.6.

The beam energy is given by

$$E = M_p \frac{\cos\theta_e + \frac{\sin\theta_e}{\tan\theta_p} - 1}{1 - \cos\theta_e} + O(m_e^2/k'^2) \tag{2.2}$$

with E the beam energy, M_p the proton mass, and m_e and k' the electron mass and momentum, respectively.

Terms of order m_e^2/k'^2 are neglected. The error due to this approximation is one part in 10^8. The proton angle is always fixed at 60^o, while the electron angle will be in the range from 9^o to 41^o depending on the beam energy, which can range from 0.5 to 6 GeV.

The particles are detected in the reaction plane using silicon micro-strip detectors. Seven electron detectors with dimensions $12.8 \times 12.8\,\mathrm{mm}^2$ are placed in each arm. Each detector is equipped with an associated scintillator as well as with a Cerenkov counter. In addition there is a proton detector with dimensions of $51.2 \times 25.6\,\mathrm{mm}^2$ placed at exactly 60^o in the reaction plane of each arm. Each proton detector has two scintillators for triggering and time-of-flight measurement purposes. Furthermore, each Si detector is equipped with an additional detector oriented perpendicularly to it. This detector is used to make measurements in the transverse plane, which is needed for final accuracy as well as to distinguish between background and elastic events.

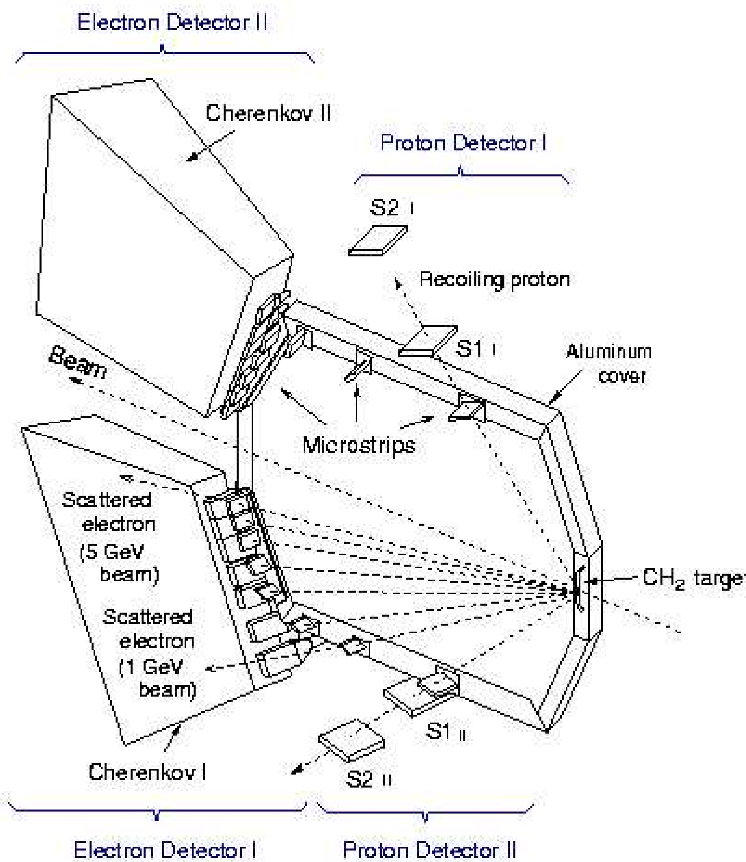

Figure 2.6: Schematic layout of the eP energy measurement system.

2.4 Targets

A ^{3}He Cryogenic target was used for the experiment. The ^{3}He cell was designed, fabricated and tested by the CalState L. A. group (D. Margaziotis, K. Aniol, M. Epstein and others). Mechanical drawings of the cell were done at JLab (P. Brindza and J. Miller), with the gas handling system designed and built at JLab.

The cell is cylindrical in shape, with a diameter of 10.32 cm and a wall thickness of 0.33 mm. It can be used with either ^{3}He or ^{4}He. During the commissioning period of the experiment, several test runs were made with the target filled with ^{4}He. During the rest of the experiment the target contained ^{3}He at a temperature of 6.3 K and pressures from 60 to 120 psi.

Gas is propelled along the axis of the cylinder at a velocity of $\sim$ 30 m/s; the electron beam is directed perpendicularly to the axis of the cylinder, and is positioned to pass through the target close to its center. To minimize damage from local heating by the electron beam, during the experiment the beam was rastered to a square 4×4 mm profile.

Figure 2.7 shows a schematic diagram of the ^{3}He target loop. ^{3}He gas is cooled in the heat exchanger, by ^{4}He supplied by the end station refrigerator (ESR) at a temperature of $\sim$ 4.5 K. Low power and high power heaters, shown in Fig. 2.7 in zigzag lines, are controlled by a Proportion, Integral and Derivative (PID) feedback system, keeping the ^{3}He gas in the target at the temperature of 6.3 K. During the experiment, two heat exchangers were connected in parallel, dramatically increasing the amount of available cooling power. The idea was proposed by P. Brindza, JLab, and allowed a substantial increase in the beam currents on the target. During the whole experiment, the ^{3}He target operated very stably, with maximum sustained currents of 140 μA at full $\sim$ 0.072 g/cm^3 density.

The measurements of temperature and pressure are made by sensors located at several positions along the cryogenic loop (see Fig. 2.7). These sensors are 70% and 99% accurate for pressure and temperature measurements respectively. Some of these sensors were damaged by the electron beam and others presented an instability in time: the only sensors used were CT93, CT96 and CT97 for the temperature measurements and PT267 for the pressure. Unfortunately, the equation of state of the ^{3}He in these temperature and pressure conditions is poorly known and does not allow an accurate determination of the target density.

Other targets employed in the experiment were: a carbon foil target, three aluminum ’dummy’ targets, and a BeO target. See Table 2.2. The carbon foil target is

Table 2.2: Targets other than ^{3}He used during the experiment.

Perpendicular Kinematics	$\|vecq\|$ [GeV/c]	E_{beam} [GeV]	ω [GeV]	ϵ	P_m [GeV/c]	Carbon Pointing	4cm Dummy	10cm Dummy
Kin01	1.50	4.80	0.837	0.943	0.00	YES	YES	YES
Kin02	1.50	4.80	0.837	0.934	0.00	YES	YES	YES
Kin03	1.50	1.25	0.837	0.108	0.00	YES	YES	YES
Kin04	1.50	4.80	0.837	0.943	0.150	YES	NO	NO
Kin05	1.50	4.80	0.837	0.943	0.150	YES	NO	NO
Kin06	1.50	1.25	0.837	0.108	0.150	YES	YES	YES
Kin07	1.50	4.80	0.837	0.943	0.300	NO	NO	NO
Kin08	1.50	4.80	0.837	0.943	0.300	NO	NO	NO
Kin09	1.50	1.25	0.837	0.108	0.300	YES	YES	YES
Kin10	1.50	4.80	0.837	0.943	0.425	YES	NO	NO
Kin11	1.50	4.80	0.837	0.943	0.425	YES	NO	NO
Kin12	1.50	1.25	0.837	0.108	0.425	YES	YES	YES
Kin13	1.50	4.80	0.837	0.943	0.550	YES	YES	YES
Kin14	1.50	4.80	0.837	0.943	0.550	YES	YES	YES
Kin15	1.50	1.25	0.837	0.108	0.550	YES	YES	YES
Kin28	1.50	4.80	0.837	0.943	0.750	YES	YES	YES
Kin29	1.94	4.80	0.837	0.943	1.00	YES	YES	YES

a thin carbon foil positioned perpendicularly to the nominal beam direction. It was used for a measurement of misspointing of spectrometers (Sec. 3.5.1). The ‘dummy’ targets are pairs of thin aluminum plates, positioned vertically at a distance of 4, 10 or 15 cm. The dummy targets are normally used for the measurement of contributions from aluminum walls of other targets. In this experiment the dummy targets were used for checks of quality of reconstruction of the reaction point along the beam. The BeO target was used to visually (through cameras) check the beam position, by observing the fluorescent light emitted from the target when hit by the beam. Hall A targets are arranged in a vertical assembly, which can be remotely moved in the vertical direction within the scattering chamber in order to expose the desired target to the beam.

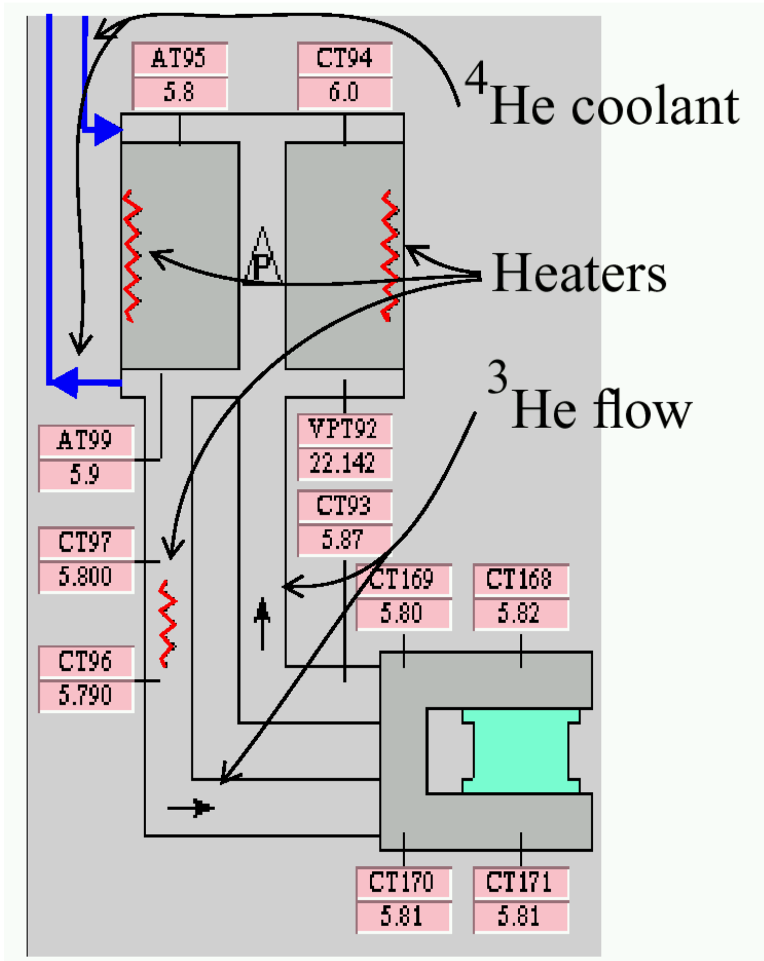

Figure 2.7: Diagram of ^{3}He target loop. During E89044, ^{3}He gas in the target was cooled by two heat exchangers connected in parallel.

2.5 Spectrometers

The Hall A spectrometers have been designed for detailed investigations of the structure of nuclei, often using the $(\mathrm{e}, \mathrm{e}'\mathrm{p})$ reaction. The measurements extend the range of momentum transfer and internal nucleon momenta over those of earlier measurements at other facilities.

The core of the Hall A equipment is a pair of identical 4 GeV/c spectrometers. Their basic layout is shown in Fig. 2.9 and Fig. 2.10. The vertical bending design includes a pair of superconducting $\cos(2\theta)$ quadrupoles followed by a 6.6 m long dipole magnet

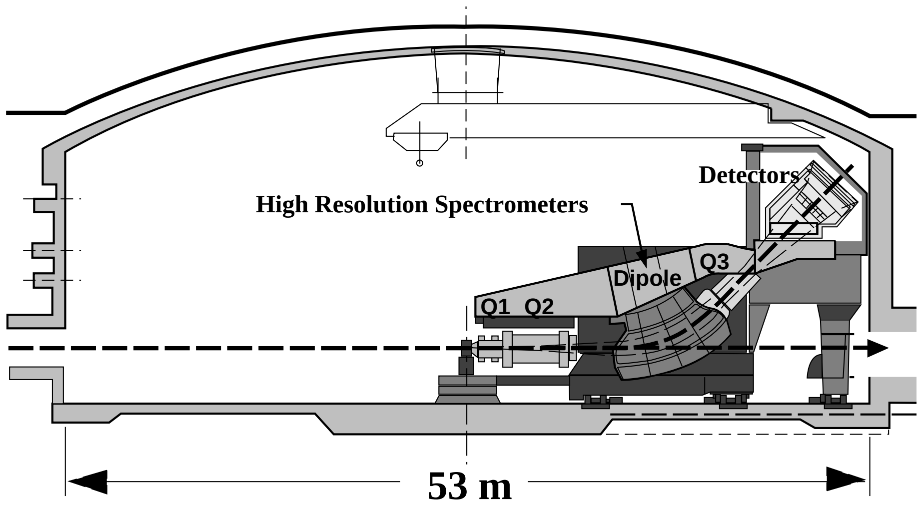

Figure 2.8: Side view of one of the Hall A HRS spectrometers.

with focussing entrance and exit pole faces, including additional focussing from a field gradient, n, in the dipole. Following the dipole is a third superconducting $\cos(2\theta)$ quadrupole. The second and third quadrupoles of each spectrometer are identical in design and construction because they have similar field and size requirements. The main design characteristics of the spectrometers are shown in Table 2.3.

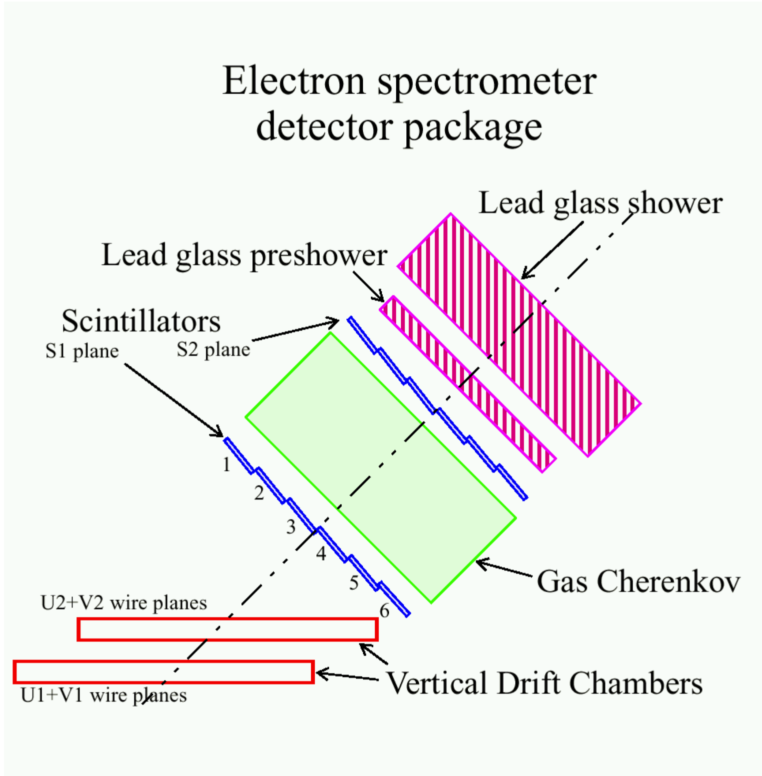

Figure 2.9: Electron arm package.

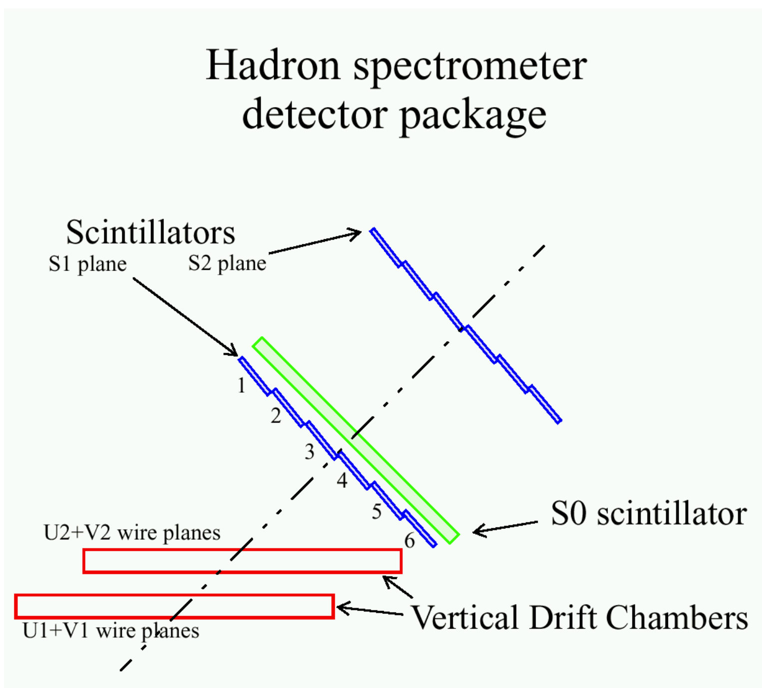

Figure 2.10: Hadron arm package.

Table 2.3: Hall A spectrometers characteristics.

Deflection angle	45°
Optical length	23.4 m
Momentum coverage	0.3 - 4.0 GeV/c
Momentum acceptance	$\pm$ 4.5%
Momentum resolution	2.5×10^{-4}
HRSe Angular coverage	12.5 - 150°
HRSh Angular coverage	12.5 - 130°
Horizontal angular acceptance	$\pm$ 30 mr
Horizontal angular resolution (FWHM)	0.6 mr
Vertical angular acceptance	$\pm$ 60 mr
Vertical angular resolution (FWHM)	2.0 mr

2.5.1 Vertical Drift Chambers

Tracking information is provided by a pair of Vertical Drift Chambers (VDCs) in each HRS, described in detail in [16].

The concept of a VDC fits well into the scheme of a spectrometer with a small acceptance, allowing a simple analysis algorithm and high efficiency, because multiple tracks are rare. The VDCs are bolted to an aluminum frame, which slides on Thomson rails attached to the box beam. Each VDC can be removed for repair using these Thomson rails. The position of each VDC relative to the box beam can be reproduced to within $100\ \mu\mathrm{m}$. Each VDC chamber is composed of two wire planes, in a standard UV configuration. The wires of each successive plane are at 90^o to one another, and lie in the laboratory horizontal plane. They are inclined at an angle of 45^o with respect to the dispersive and non-dispersive directions.

The nominal particle trajectory crosses the wire planes at an angle of 45^o with respect to the dispersive and non-dispersive directions. The nominal particle trajectory crosses the wire planes at an angle of 45^o (see Fig. 3.2). There are a total of 368 sense wires in each plane, spaced 4.24 mm form each other. The signals from the sense wires

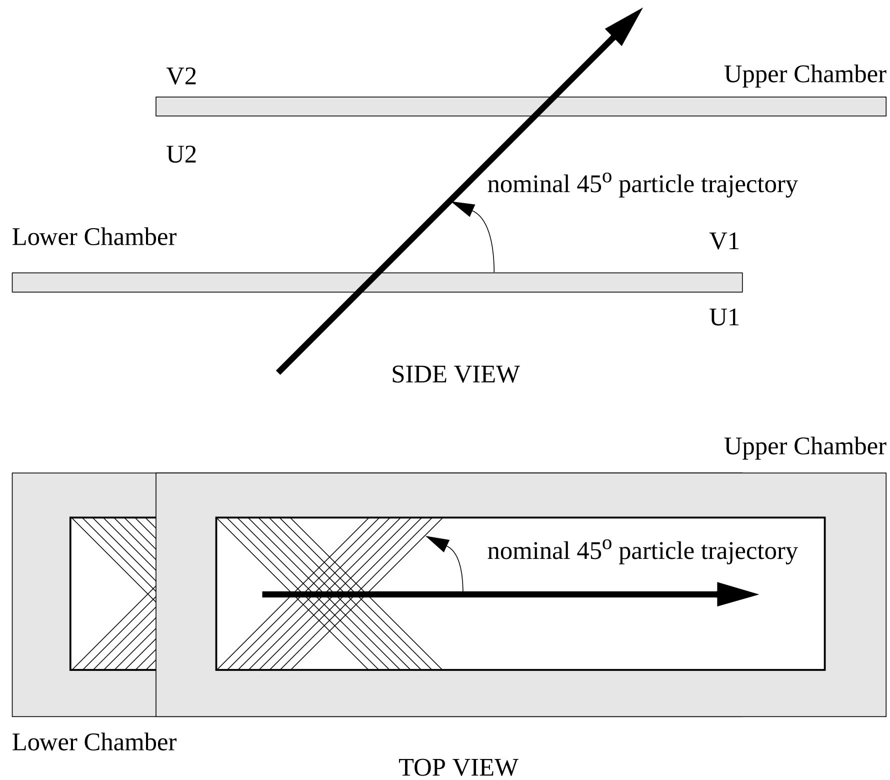

Figure 2.11: A pair of vertical drift chambers, as mounted at the focal plane. Figure courtesy Kivin Fissum.

are shaped by a LeCroy 2735DC amplifier-discriminator card mounted 30 cm away from the chamber. The ECL logic signals are then routed via $5\ \mathrm{m}$ long twisted-pair cable to a FastBus LeCroy TDC module 1877. The feedback of the ECL signals from these cables on the sense wires and amplifier inputs is suppressed by careful shielding of the output cables and VDCs.

The electric field of the VDCs is shaped by gold-plated Mylar planes, nominally at $-4.0\ \mathrm{KV}$ when the standard gas mixture of argon (62%) and ethane (38%) is used. The gas is bubbled through cooled alcohol to reduce aging effects on sense wires and flows at about $5\ \mathrm{l/h}$.

2.5.2 Scintillators

There are two primary trigger scintillator planes (S1 and S2) separated by a distance of about $2\ \mathrm{m}$. The scintillators were built by the University of Regina, Canada. They were assembled at TRIUMF in 1994. Each plane is composed of six identical overlapping paddles made of thin plastic scintillator $(5\ \mathrm{mm\ BC408})$ to minimize hadron absorption. Each scintillator paddle is viewed by two photomultipliers (PMTs). The time resolution per plane is approximately $0.30\,\mathrm{ns}$. The active area of S1 is about $175\ \mathrm{cm} \times 35\ \mathrm{cm}$ and that of S2 is $220\ \mathrm{cm} \times 54\ \mathrm{cm}$. During the experiment, we needed a high hadron trigger efficiency, so an additional scintillator trigger counter $(\mathrm{S0})$ was introduced immediately behind the S1 scintillator plane. S0 is 10 mm thick and has an active area of $190\ \mathrm{cm} \times 40\ \mathrm{cm}$. The S0 paddle is viewed by 2 PMTs, labeled top (T) and bottom (B).

2.5.3 Gas Cerenkov Detector

To discriminate between electrons and pions, a threshold gas Cerenkov detector was employed. A Cerenkov detector operates on the principle that when a charged particle travels through the detector medium, it emits Cerenkov light if it travels faster than light would in that same medium $(i.e; v \geq c/n$, where n is the index of refraction of the detector medium). The Cerenkov light is emitted about the particle's trajectory in a forward pointing cone with an angle, θ_{c} defined by:

$$\cos(\theta_c) = 1/n\beta. \tag{2.3}$$

The Cerenkov detector employed in the HRSE used 2780 liters of $\mathrm{CO_2}$ gas as a medium. The carbon dioxide was at atmospheric pressure, leading to an index of n=1.00041. With this index of refraction, the minimum particle momentum for the production of Cerenkov light is 0.017 GeV/c for electrons and 4.8 GeV/c for pions. Note that the threshold momentum of pions is above the maximum momentum for the spectrometer so pions could only give a Cerenkov signal through the production of knock-on electrons (known as δ-ray electrons).

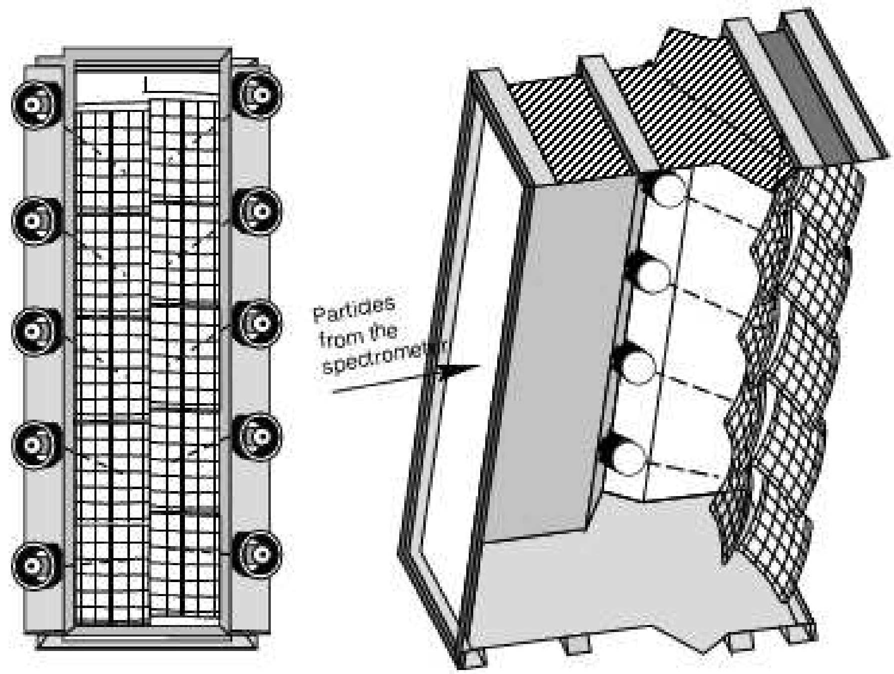

Figure 2.12: Gas Cerenkov detector in electron arm.

The Cerenkov is a rectangular tank, with 10 Photo-Multiplicator tubes (PMT) and 10 mirrors. The PMTs have a spherical entrance window of 129 mm diameter of which only a spherical part of 110mm of diameter is efficient to collect the light obtained after reflection on the mirrors. The photocathode is made of bialkali with a quantum efficiency of 22.5 % at 385 nm and an extended response in the UV until 220 nm. Each mirror has a rectangular profile built in an empty sphere of interior radius (reflective face) of 900 mm and thickness of 10 mm.

The 10 mirrors are placed just before the output window and are grouped in two columns of 5 mirrors. Each mirror reflects light onto a PMT placed at the side of the box, see Fig. 2.12. The mirrors of each column are identical and the two columns are almost symmetrical. Positions and angles of the PMTs are not placed regularly like for the mirrors but were adjusted by an optical study in order to maximize the collection of light coming from the particular envelope of particles which have to be detected with the spectrometer. The PMTs are fixed but the mirrors can be adjusted.

We expect to have 15 photoelectrons per meter of gas. With our apparatus the length of gas crossed is 1.5 meters so we expect to have 23 photoelectrons from each electron. This theoretical value was verified experimentally with a beam and leads to an efficiency greater then 99.99 %.

2.5.4 Shower and Preshower detectors

Lead-glass counters provide additional Particle Identification (PID). They are electromagnetic calorimeters that detect the energy deposited when a particle enters the detector. A high energy electron will radiate photons through Bremsstrahlung in the calorimeter, which will, in turn, generate positron-electron pairs. These pairs will also radiate photons, and a shower of electrons, positrons and photons will be generated. Electrons and positrons produce Cerenkov light which will be detected by the PMTs at the end of each block.

Hadrons, mainly pions, usually deposit a small amount of energy due to ionization and direct cerenkov light giving an energy ratio, deposited to incident, much smaller than one.

The Hall A electron HRS is equipped with two layers of segmented total absorption lead-glass detectors, called preshower and shower detectors. The preshower consists of 24 identical modules in front of the shower detector. Each module consists of two lead glass blocks of size $10\ \mathrm{cm} \times 10\ \mathrm{cm} \times 35\ \mathrm{cm}$, made of TF-1 lead-glas. Each module is viewed by a single PMT optically coupled to the side of the block. The second layer, the shower detector, is made of 96 (16×6) blocks of SF-5 lead-glass each one is $15\ \mathrm{cm} \times 15\ \mathrm{cm} \times 35\ \mathrm{cm}$. The shower detector serves as a total absorption calorimeter; it is 14.83 radiation lengths thick, while the preshower is just 3.65 radiation lengths thick.

There is a big difference between the mean free paths of electrons and hadrons, so the electron has a high probability of starting a shower in the preshower while the pions mostly pass thru without starting a shower. By looking at the energy deposited in the preshower detector versus the energy deposited in the shower detector, electrons and pions can be distinguished.

2.5.5 Collimators

Each spectrometer is equipped with a set of collimators, positioned 1.25 m from the target on the electron and hadron spectrometers, respectively. There are three collimators for each spectometer and each collimator can be selected remotely via a vertical actuator:

- Large collimator, made of $80\ \mathrm{mm}$ thick tungsten with a vertical window opening varying from 121.8mm to 129.7 mm and a horizontal opening varying from 62.9 mm to 66.8 mm.

- Small collimator, made also from tungsten. It is $53.2\ \mathrm{mm} \times 21.3\ \mathrm{mm}$ at the entrance face and $53.2\ \mathrm{mm} \times 22.6\ \mathrm{mm}$ at the exit face.

- Sieve slit, used to study optical proprieties of the spectrometers. The sieve slit is a 5 mm thick tungsten plate with dimensions of approximately 200 mm $\times$ 300 mm. A regular pattern of 49 (7×7) circular holes is drilled through the sieve slit surface. Most of the holes are 2 mm in diameter, except for two, one in the center and one displaced two rows vertically and one row horizontally, which are 4 mm in diameter. During the study, the sieve slit is moved in across the spectrometer entrance window and allows to cut out the events which do not pass through the holes; in fact particles reaching the spectrometer after crossing the tungsten thickness are subject to energy loss and it is easy to separate them from the ones passing through the holes. The sieve slit is positioned 75 mm further from the target.

2.6 Coordinate systems

An overview of the coordinate systems used in this document is presented. All coordinate systems presented are Cartesian. In this section, angular coordinates should be taken to refer to the tangent of the angle in question.

2.6.1 Hall A Coordinate System (HCS):

The origin of the HCS is at the center of the hall, defined by the intersection of the electron unrastered beam, centered in the last three BPMs, and the vertical symmetry axis of rotation of the target assembly. A top view of the Hall A coordinate system is presented in Fig.2.13. The $\hat{z}$ axis is along the beam line and points in the direction of the beam dump, $\hat{y}$ is vertically upward, and $\hat{x}$ = $\hat{y} \times \hat{z}$.

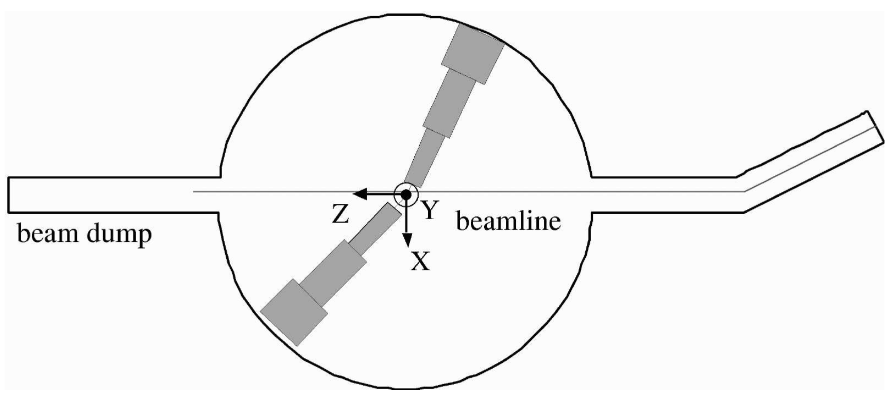

Figure 2.13: Top view of the Hall A coordinate system.

2.6.2 Target Coordinate System (TCS):

Each Spectrometer has its own TCS. A line perpendicular to a sieve slit surface of the spectrometer and going through the mid-point of the central sieve slit hole defines the z axis of the TCS for a given spectrometer. See Fig. 2.14. The x axis is the line crossing the center of the sieve slit and pointing downward. Under optimal circumstances this origin should coincide with the origin for the Hall A laboratory coordinate system and the center of rotation of the spectrometer. The $x - z$ plane contains the y axis of the hall coordinate system. The triplet $\hat{x}$, $\hat{y}$ and $\hat{z}$ is right handed. Variables referring to the coordinates at the target are designed by the subscript "tg". Variables x_{tg} and y_{tg} are defined as the x and y coordinates of the point of intersection of a particle trajectory with the z_{tg} = 0 plane. The variables θ_{tg} and ϕ_{tg} are defined as:

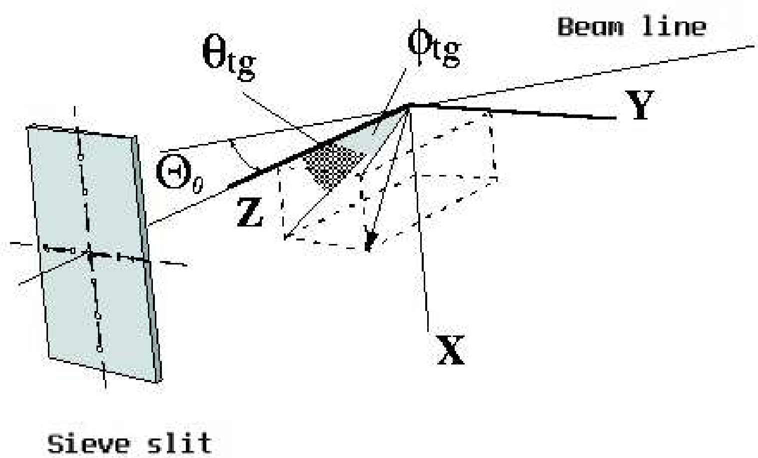

Figure 2.14: Target coordinate system.

$$\tan\theta_{tg} = \frac{dx}{dz}, \quad \text{and} \tag{2.4}$$

$$\tan\phi_{tg} = \frac{dy}{dz}. \tag{2.5}$$

The relative momentum δ_{tg} is defined by $\delta_{tg} = (p - p_0)/p_0$, where p is the particle momentum and p_0 is the spectrometer central momentum. Additional subscripts ‘e’ or ‘h’ on x_{tg}, y_{tg}, θ_{tg}, ϕ_{tg} and δ_{tg} denote whether the coordinate system of the electron or hadron arm.

2.6.3 Focal Plane Coordinate System (FPCS):

The origin of the focal plane coordinate system is defined as the point of intersection of wire 184 of the U1 VDC wire plane with the projection of wire 184 of the V1 wire plane on the U1 wire plane. The $\hat{y}$ axis lies in the U1 wire plane and is parallel to the short symmetry axis of the VDC1; the $\hat{z}$ axis points in the direction of the projection of the local central ray ($x_{tg} = y_{tg} = \theta_{tg} = \phi_{tg} = 0$) on a plane perpendicular to the $\hat{y}$ axis (Fig. 2.15). Variables referring to the focal plane coordinate system are designated by the subscript "fp".

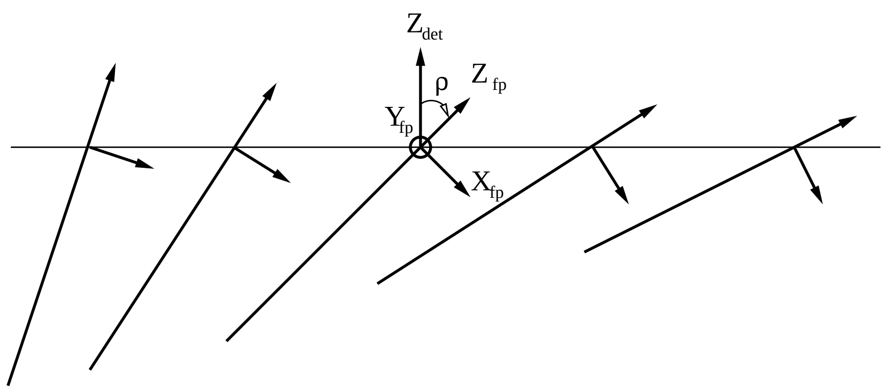

Figure 2.15: Definition of the Focal Plane Coordinate system.

Coordinates y_{fp} and ϕ_{fp} are corrected for misalignments in the VDC package by a set of polynomial coefficients y_{i000} and p_{i000} acting on powers of x_{fp} [27]. The dependence of the angle between the local central ray ($x_{tg} = y_{tg} = \theta_{tg} = \phi_{tg} = 0$) and the central ray ($x_{tg} = y_{tg} = \theta_{tg} = \phi_{tg} = \delta_{tg} = 0$) on the particle momentum is contained in another set of polynomial coefficients, t_{i000}, also acting on powers of x_{fp} [16]. Coefficients y_{i000}, p_{i000} and t_{i000} are determined during calibration of the spectrometer optics database; see Sec. 3.4.

2.7 Data acquisition and electronics

2.7.1 Data acquisition system

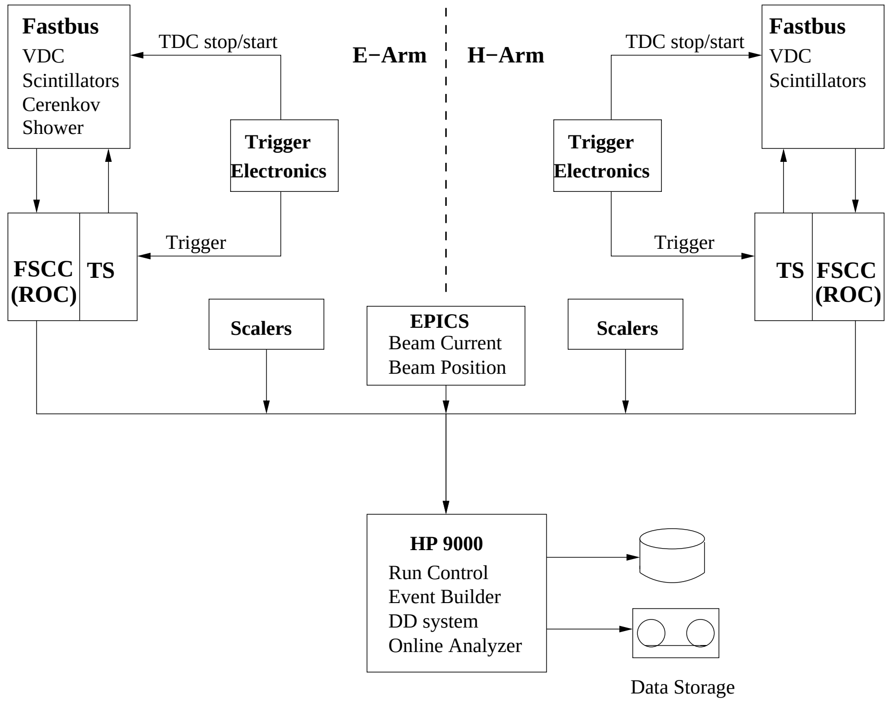

Figure 2.16: Block-diagram of the Hall A DAQ system.

The E89044 experiment used the CEBAF online data acquisition (CODA) system [29]. CODA is specially designed for nuclear physics experiments at Jefferson Lab. It consists of a set of software and hardware packages from which the data acquisition system can be constructed. The recorded data file starts with a header which gives the run size and the run number. The data file also contains:

- CODA events from the detectors and the beam helicity signal.
- EPICS [30] data from the slow control software used at JLAB. The sampled beam current and beam position information as well as the magnet information and target temperature and pressure are fed to EPICS and recorded.
- CODA scaler events: the DAQ reads the scaler values every few seconds and

feeds them to the main data stream. The scalers are read from the trigger supervisor (TS) so they are not affected by the DAQ dead time. Therefore, one can use scaler readings to correct the DAQ dead time.

The data were first written to a local disk and then transferred to the Mass Storage System (MSS). The total volume of data recorded during the 5 months of the E89044 experiment was about 1.4 TBytes. The data were analyzed using a standard event processing, FORTRAN-based program, ESPACE (Event Scanning Program for Hall A Collaboration Experiments) [27]. ESPACE was originally developed at Mainz and improved at MIT before being introduced to Hall A in 1995. Common operations such as histogramming, graphics and macro processing are implemented using various CERNLIB packages [31]. ESPACE's capabilities include:

- Reading, decoding and scaling raw event data.
- Reconstruction of wire chamber tracks, computation of spectrometer focal-plane coordinates and target quantities.
- Computation of basic physics quantities like the angles, four vectors and kinematics.
- Dynamic definition of histograms and ntuples, and output of these in HBOOK format [32].
- Fitting of analysis parameters to experimental data, including: position offsets and spectrometer reconstruction matrix elements.
- Display of single events in terms of detector hits in a graphics window.
- Program control and analysis steering via the Kit for a User Interface Package (KUIP).

2.7.2 Trigger setup

In the E89044 experiment setup, the main physics trigger types were: an electron spectrometer singles trigger, T1, a hadron spectrometer singles trigger, T3, and a coincidence trigger, T5. Auxiliary physics triggers, used for measurements of efficiencies of the main triggers, were an electron spectrometer trigger (denoted "T2", or "type 2"), and a hadron spectrometer trigger ("T4", or "type 4").

Fig. 2.17 shows a simplified schematic view of the setup of the main physics triggers. The main physics triggers were generated using scintillator signals. The scintillators were arranged in two planes in each of the two detector packages, with six scintillator paddles in each plane, and two photomultiplier tubes (PMTs) viewing each paddle. Therefore, the PMTs of the two scintillator planes provided $2 \times 2 \times 6 = 24$ signals for each spectrometer. In Fig. 2-14 "S1" and "S2" denote signals from the lower and the upper scintillator planes, respectively. "S1-L" ("S1-R") denotes scintillator signals from the left (the right) PMTs of the lower scintillator plane. "S2-L" ("S2-R") denotes scintillator signals from the left (the right) PMTs of the upper scintillator plane.

Analog signals from the scintillator PMTs were first sent to a discriminator (LeCroy Model 4413/200) providing both analog and digitized outputs. The analog signals were sent to ADCs. The digitized signals were split in three parts: one part was sent to TDCs, another part was sent to scalers gated by the start and the end of each run, and the third part was sent to a logical AND unit making a coincidence between pairs of PMTs viewing the same paddle. For each spectrometer, 12 outputs of the logical AND unit were fed into the Memory Lookup Unit (MLU, LeCroy Model 2372). The MLU is a programmable device that, given a combination of logical signals at its inputs, provides a corresponding (programmed) combination of logical signals at its outputs. In the experiment, the electron and the hadron spectrometer MLUs were programmed to issue a logical signal 'S-ray' when:

1. Coincident hits were present in both PMTs of a scintillator paddle in the S1

scintillator plane.

2. Coincident hits were present in both PMTs of a scintillator paddle in the S2 scintillator plane.

3. These two paddles were either adjacent or coincided in their relative position in the planes.

The coincidence between the S-rays from the two spectrometers within a $\sim$ 100 ns time window formed the coincidence trigger T5. The absence of a coincidence, but the presence of an S-ray, formed either the electron singles trigger T1, from the electron spectrometer S-ray, or the hadron spectrometer singles trigger T3, from the hadron spectrometer S-ray.

The auxiliary trigger type 2 for the electron spectrometer was generated when the electron S-ray was not present and any two of the three following "events" were coincident:

1. A coincidence between both PMTs of a scintillator paddle in the S1 scintillator plane of the electron spectrometer.

2. A coincidence between both PMTs of a scintillator paddle in the S2 scintillator plane of the electron spectrometer.

3. The analog sum of the 10 Gas Cherenkov PMTs (electron spectrometer) above a threshold.

Similarly, the auxiliary trigger type 4 for the hadron spectrometer was generated when the hadron S-ray was not present and any two of the three following "events" were coincident:

1. A coincidence between both PMTs of a scintillator paddle in the S1 scintillator plane of the hadron spectrometer.

2. A coincidence between both PMTs of a scintillator paddle in the S2 scintillator plane of the hadron spectrometer.

3. A coincidence between both PMTs of the S0 scintillator paddle (hadron spectrometer).

From the description above it can be seen that the five trigger types are exclusive, i.e. any given trigger can have only a single type, T1, T2, T3, T4, or T5[1]. Scalers counting the number of issued T1 and T3 triggers in fact counted the number of S-rays that occurred in the electron and hadron spectrometers, and therefore their number had to be corrected by the number of coincidence triggers (the correction is described in Sec. 3.4).

The electron and hadron spectrometer MLUs that issued the S-rays were operated in a "strobed" mode. In this mode, the MLUs were issuing an S-ray only 45 ns after arrival of an "enable" signal. The enable signal was formed by the logical OR of the signals from the right PMTs of the S1 and S2 scintillator planes, with the signals from the S1 plane delayed in time relative to the signals from the S2 plane. This setup guaranteed that the timing of generation of the main physics triggers was always defined by the right PMTs of the S2 scintillator plane. This definitiveness of the timing simplifies reconstruction of events (Sec. 3.2.1).

Generated trigger signals were fed into a custom-built Trigger Supervisor (TS) module, which prescaled the triggers and, based on the current state of the data acquisition system (DAQ), decided whether to prompt the DAQ to start the event readout. Trigger prescale factors were downloaded into the TS at the start of runs. In the Hall A TS setup, the prescale factor n for the trigger type i means that the TS attempts to read out every nth event of type i.

[1]Another physics trigger type, T14, occurred (very infrequently) when there was an overlap of 10 ns or less between any two or more of the five main trigger types (T1 – T5) at the Trigger Supervisor.

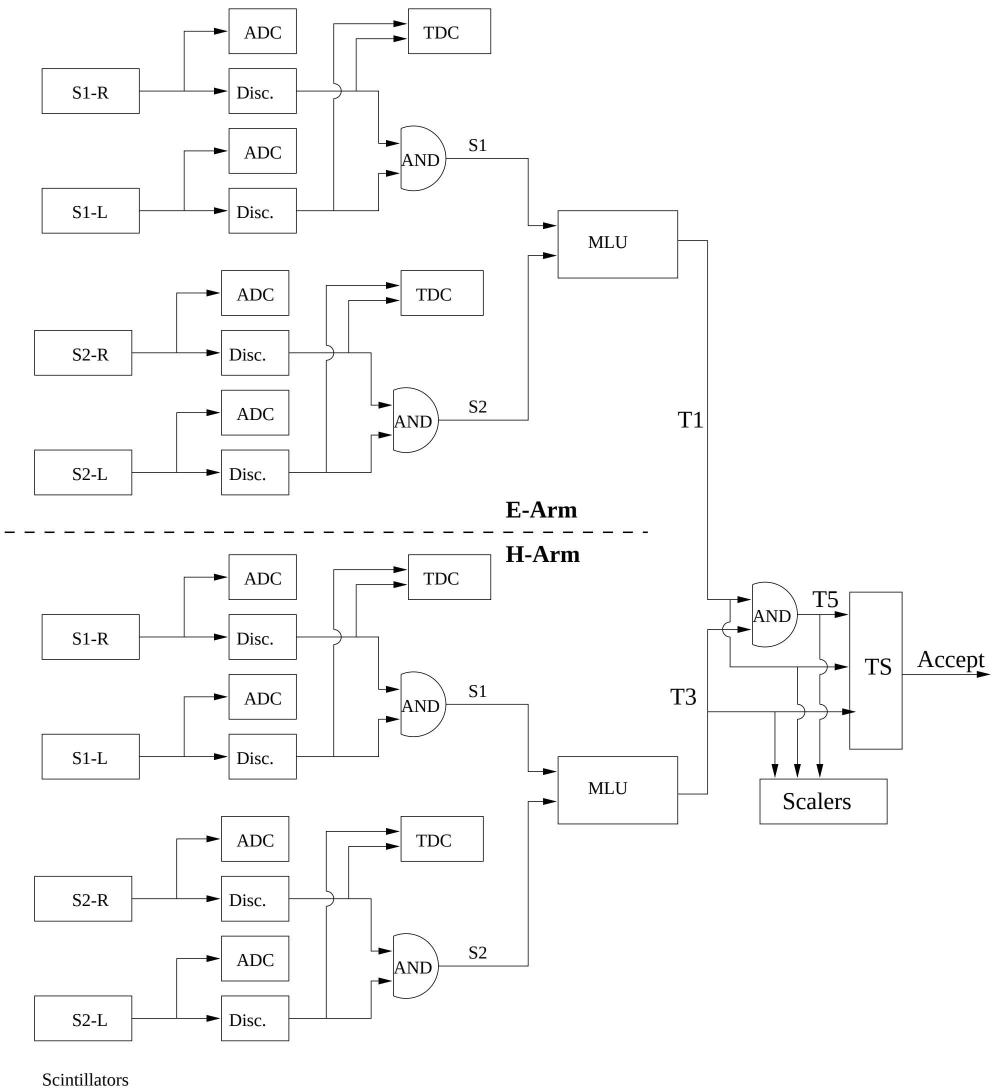

Figure 2.17: Simplified block-diagram of setup of the main physics triggers.

Chapter 3
Detector Calibration

This chapter we describes the calculation of trigger efficiency, tracking efficiency, gas Cherenkov efficiency, proton absorption, the calibration of the optics and detector databases, the measurement of the misspointing of the spectrometers, and the calculation of computer and electronic deadtimes.

3.1 Time parameters

The reconstruction of the trajectories in the wire chambers depends on the determination of the distance of the detected ionizing particle to the wire: it is important to know the both the drift time and drift velocity of the particles resulting from the ionization of the gas. The drift velocity was obtained after calibration and it is equal to 4.9 $\times$ 10^4 m/s [23].

The drift time is extracted form a TDC (Time to Digital Converter) for which the start signal is issued from the wire chamber and the stop signal is given by one of the right photomultipliers of the S2 scintillator. By taking as a reference the ionization time of the gas in the wire chamber plane,

- the starting time $\mathrm{t_{start}}$ is equivalent to the drift time $\mathrm{t_{drift}}$ plus the electronic and propagation delays of the signal $\mathrm{t_{VDCdelay}}$;

- the stopping time $\mathrm{t_{stop}}$ is equivalent to to the time of flight from the wire chamber plan to the scintillator S2 $\mathrm{t_{flight}}$, plus the propagation time of the light in the scintillator to the photomultiplier $\mathrm{t_{prop}}$ and to the electronic and propagation delay of the signal.

Thus, we define that

$$t_{stop} - t_{start} = t_{flight} + t_{prop} - t_{scint.delay} - t_{drift} - t_{VDCdelay} \tag{3.1}$$

so

$$t_{drift} = t_{flight} - (TDC) + t_{scint.delay} - -t_{VDCdelay} \tag{3.2}$$

where $\mathrm{TDC} = \mathrm{t_{stop}} - \mathrm{t_{start}}$.

Calibration of the drift time requires the knowledge of the TDC's "pedestals", the essentially constant delay times, obtained from specific runs during the experiment. The wire chamber parameters were very well calibrated during previous experiments and during the data taking of present experiment. The parameters related to the scintillators were calibrated by N. Lyanage [16] via the variable β.

The time of flight $\mathrm{t_{flight}}$ from a wire chamber plane to the S2 scintillator is obtained from the distance between the two detectors and the velocity β. This velocity is obtained from the time of flight between the two scintillators S1 and S2 which includes the propagation delays, the electronic delays and the gains of the TDCs of the photomultipliers. The calibration of β, hence, allows the optimization of the time parameters involved in the determination of the drift time. If the calibration is well done, the velocity β should be equal to momentum of the particle divided by its total energy: β=p/E. See Fig. 3.1.

3.2 Calibration of the ADCs

The principle of calibration of gains and pedestals of the S1 and S2 scintillators and the Cerenkov detector is the same. It is not a matter of an absolute calibration, but a matter of adjusting the gains of the ADCs of these detectors so that the gains of each channel of a detector are equal. This procedure corrects for variations in light

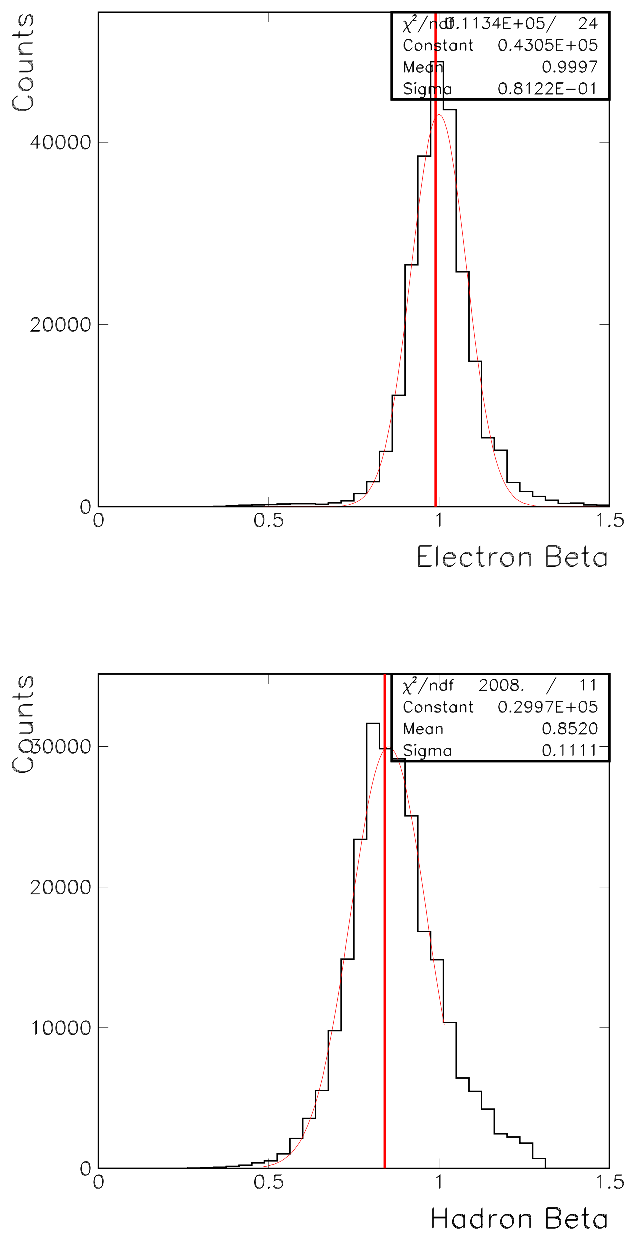

Figure 3.1: Velocity β for electron and hadron arms after calibration. The vertical line shows the position of β calculated from the ratio p/E.

output and collection, photomultiplier gain, cable attenuation, and ADC response. This adjustment is made using the programm ESPACE.

Pedestals of the ADCs are determined from specific runs called pedestal runs, by reading the ADC's values when the electron beam is off. For each channel, the gain is then calculated that the mean value of the ADC, corrected by the pedestal, for all the events coincides with the channel number 1000. Inside each scintillator paddle, the energy deposited is then corrected from the light attenuation in the scintillator material by an exponential law: the attenuation length λ is given by $1/\lambda = 0.7\ \mathrm{m}^{-1}$ for S1 and $1/\lambda = 0.6\ \mathrm{m}^{-1}$ for S2 and S0.

3.3 Efficiencies

3.3.1 Trigger efficiency

Triggers are generated based on scintillator signals and trigger inefficiency is directly caused by scintillator inefficiency which arises due to:

- statistical fluctuations due to a small amount of energy deposited by the charged particles in the scintillator paddles,
- imperfect transmission of light emitted by the particles in the paddles to the photomultiplier tubes (PMTs),
- inefficiencies of the PMTs, and
- other inefficiencies.

Most events missed by the main physics trigger types 1, 3 and 5 (T1, T3 and T5) due to the trigger inefficiency still cause a trigger type 2 (T2) in the electron spectrometer or type 4 (T4) in the hadron spectrometer. Trigger type T2 and T4 allow the calculation of the trigger efficiencies. These triggers were prescaled and recorded to disk at a rate of 50 Hz.

Triggers of types 2 and 4 can be caused by:

1. Background events with trajectories outside the focal plane envelope, hitting a "large-angle" combination of the scintillator paddles in the two scintillator planes S1 and S2.

2. Background events with trajectories outside the focal plane envelope, hitting a scintillator paddle in one of the two scintillator planes, and producing a signal in the Gas Cerenkov (HRSE) or in the S0 detector (HRSH).

3. "Good" events falling within the focal plane envelope and generally having a track in the VDCs, but failing to generate a singles or a coincidence trigger due to the trigger inefficiency, and producing a signal in the Gas Cerenkov (HRSE) or in the S0 detector (HRSH).

As a first step in finding the trigger efficiency, one has to filter out the background events (falling outside the focal plane envelope) from a run containing a large number of recorded T2 and T4 events. Then, one has to separate electrons from π^- in the electron spectrometer (for the T2 events), and protons from π^+ and other positive particles (such as ^{2}H and ^{3}H) in the hadron spectrometer (for the T4 events). These steps are described next.

Background events with trajectories outside the focal plane envelope were filtered out by a software cut requiring a good VDC track reconstructing to the target (both for T2 and T4 events). For T2 events, electrons were separated from the π^- by a cut requiring the sum of the 10 Gas Cerenkov ADC signals to be above a cutoff value. The ADC signals in the sum were corrected for pedestals and gains, as described in Sec. 3.2. For T4 events, the protons were separated from other positive particles by a cut requiring the sum of the two S0 ADC signals to be in the range corresponding to protons (Fig. 4.7). The two S0 ADC signals were corrected for pedestals, gains and light attenuation in the S0 scintillator paddle (Sec. 3.2).

The trigger efficiencies ϵ_e and ϵ_p for detection of electrons and protons, respectively, averaged over the focal plane, were then calculated from the number of (corrected for prescaling, computer and electronic deadtimes) events N_i of trigger types $i = 1, ..., 5$ in the remaining sample, as

$$\epsilon_e = \frac{N_1 + N_5}{N_1 + N_5 + N_2} \tag{3.3}$$

and

$$\epsilon_p = \frac{N_3 + N_5}{N_3 + N_5 + N_4} \tag{3.4}$$

The trigger efficiency determined at different kinematic settings and at different times during the experiment gave consistent results, with 99.9% efficiency of detection of electrons in the electron spectrometer, and 99.8% efficiency of detection of protons in the hadron spectrometer. Statistical errors of the measurements were less than 0.05%.

3.3.2 Wire chamber and tracking efficiency

The efficiency of a single sense wire in the wire chambers is the probability that the wire fires when a charged particle passes sufficiently close to it. It can be estimated with the formula:

$$\epsilon_{wire} = \frac{N_1}{N_0 + N_1}, \tag{3.5}$$

where N_1 (N_0) is the number of times the wire fired (did not fire) when 2 wires adjacent to it fired. The efficiency determined with this formula was monitored during the experiment with the online code "dplot", and is shown in Fig.s 3.2. for the electron spectrometer V2 wire plane and the hadron spectrometer U2 wire plane (^{3}He(e,e′p) data, kinematics 1). The efficiency was determined to be greater than 0.98 for all wires within the acceptance region of the spectrometers used in cross section analysis.

Equation 3.5 does not take into account the case where different particles produce clusters of hit wires with a gap of one wire in between, therefore, this estimated wire

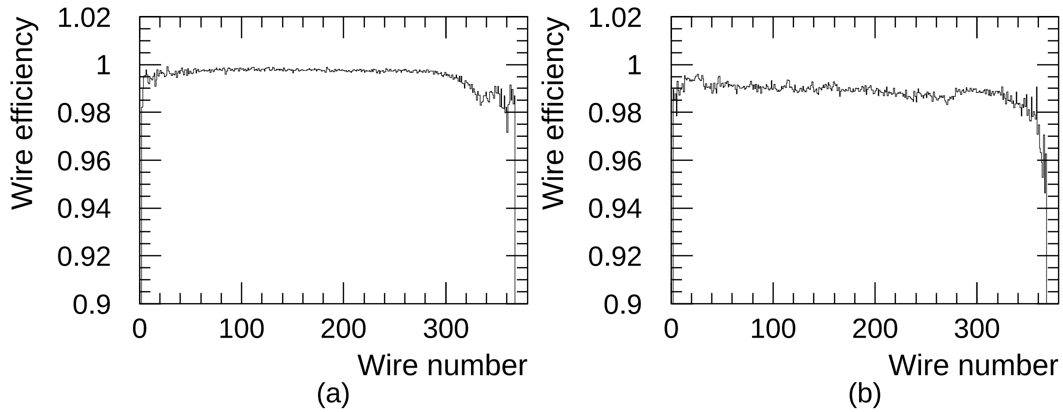

Figure 3.2: Efficiency of VDC wires calculated with the formula 3.5: (a) HRSE V2 wire plane; (b) HRSH U2 wire plane at Kinematics 1. Figure was taken from [23].

efficiency should be considered as a lower bound.

To exclude poorly reconstructed events from the analysis, the following "tracking" cuts were imposed:

- The number of clusters in each wire chamber plane equal to 1.
- The multiplicity i.e, the number of hit wires in the cluster, of each cluster greater than or equal to 3 and less than or equal to 7.

For the singles events these cuts were imposed only on the spectrometer that issued the trigger; for the coincidence events these cuts were applied to both spectrometers. In addition to eliminating events with high cluster multiplicity (created mostly by delta-rays) and events with multiple tracks, these cuts also excluded events with low multiplicity or a missing cluster of hit wires in any of the wire planes. Such events formed a tiny ($< 0.1\%$) fraction of all recorded events and were mostly background particles that happened to have a trajectory satisfying a "good" trigger logic. In general, these background events reconstructed outside the target boundary.

The tracking efficiency $\epsilon_{tr,i}$ for events of type i was then calculated as

$$\epsilon_{tr,i} = \frac{N'_i}{N_i}, \qquad i = 1, 3, 5, \tag{3.6}$$

where N'_i is the number of events of type i passing the tracking cuts, and N_i is the total number of recorded events of type i.

By dividing the detected yield by the tracking efficiencies $\epsilon_{tr,i}$, the detected yield was corrected for events eliminated by the tracking cuts during the cross section analysis. It was assumed that all events eliminated by the tracking cuts were "good" events. Another assumption was that the tracking efficiency is uniform over the active area of the drift chambers. This assumption was found to be correct by a calculation of the tracking efficiency in different regions of the drift chambers.

The magnitude of tracking efficiencies $\epsilon_{tr,i}$ varied between kinematic settings and depended mostly on the rate of particles at the focal planes, through changes in the rate of events with multiple tracks. Overall, the tracking efficiency was rather low, $\sim$ 0.8 for the singles and $\sim$ 0.6 for the coincidence events. For the coincidence events, the tracking cuts required a single good track in both spectrometers, while for the singles events the tracking cuts required a single good track in one of the two spectrometers. This is the reason why the tracking efficiency for the coincidence events is lower.

Despite the low tracking efficiencies, the absolute systematic error due to correcting for the efficiencies was found to be $\sim$ 0.5% for the singles events and $\sim$ 1% for the coincidence events.

3.3.3 Gas Cerenkov efficiency

The electron spectrometer Gas Cerenkov detector is described in Sec. 2.5.3. Figure 2.5.3 shows the distribution of the sum of the 10 gas Cerenkov ADCs corrected for pedestals and gains. The electrons detected in the electron spectrometer were separated from the π^- by a software cut requiring that the sum ($\mathrm{ADC_{sum}}$) is greater than 50.

The gas Cerenkov inefficiency is defined as the fraction of electrons eliminated by

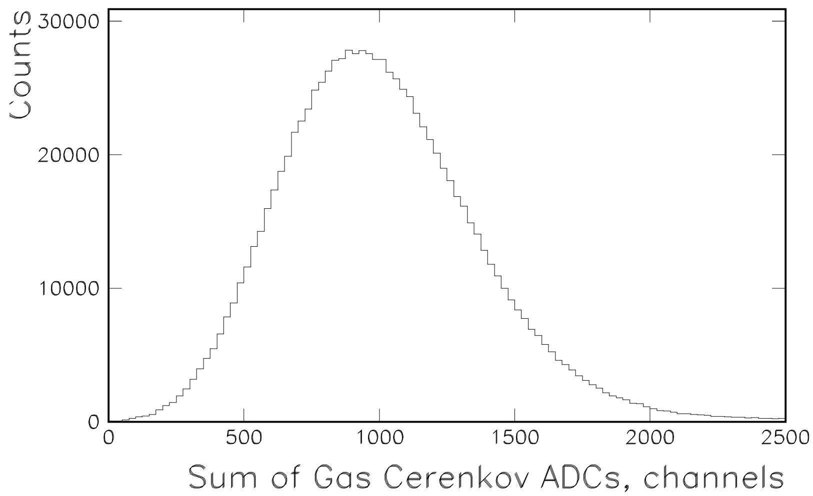

Figure 3.3: Distribution of sum of the 10 Gas Cerenkov ADCs corrected for pedestals and gains, obtained Kinematics 4.

the cut $\text{ADC}_{\text{sum}} > 50$. The inefficiency can be found by considering a sample of data containing purely electrons (and no π^-), and calculating the fraction of events eliminated by the cut.

A simple calculation [16] shows that π^- truly coincident with a positively charged particle in the hadron spectrometer are kinematically not allowed in the ^{3}He(e,e′p)d two-body breakup (2bbu) peak. Therefore, to obtain the required pure sample of electrons, one has to apply the E_{miss} cut selecting the 2bbu peak on a sample containing very few accidental coincidence events. Such a sample was obtained from the ^{3}He(e,e′p) data collected at $P_{miss} = 150$ MeV/c kinematics (where the rate of the accidental coincidences is extremely low), by applying a tight cut on the real coincidence peak; see Fig. 4.3.

Then, the gas Cerenkov efficiency was found with

$$\epsilon_{GC} = \frac{N_{cut}}{N_{tot}}, \tag{3.7}$$

where N_{cut} is the number of events in the sample after application of the cut $\text{ADC}_{\text{sum}} >$

50, and N_{tot} is the total number of events in the sample. The Gas Cerenkov efficiency determined with the technique described was found to be $\sim$ 0.9996 for kinematics 4 and 5.

3.3.4 Proton absorption

The fraction of the protons knocked-out from ^{3}He that were lost before reaching the hadron spectrometer scintillators was calculated with a GEANT [33] simulation by George Chang, Univ. of Maryland. The protons are lost due to the energy losses, absorption and p-N rescattering in the target and spectrometer material, and in the air.

The number of events within the acceptance with and without simulation of energy losses yielded the estimate of proton absorption, $\sim$ 2.3%. This estimate was obtained for the kinematic setting 1 (nominal $P_{miss} = 0$, $E_{beam} = 4.8$ GeV), but is applicable to all kinematic settings analyzed in this thesis, since the hadron spectrometer central momenta were close to 1.5 GeV/c at all kinematic settings. The largest proton absorption, as expected, was due to the proton absorption in the ^{3}He gas in the target.

3.4 Optics calibration

The target coordinate system, denoted by the subscript "tg", and the focal plane coordinate system, denoted by the subscript "fp", are defined in Sec. 2.6. The transformation from the focal plane to the target coordinate system is done through matrix elements Y_{ijkl}, T_{ijkl}, P_{ijkl}, D_{ijkl}, as:

$$y_{tg} = \sum_{i,j,k,l} Y_{ijkl}\, x^i_{fp} \tan^j(\theta_{fp})\, y^k_{fp} \tan^l(\phi_{fp}), \tag{3.8}$$

$$\tan(\theta_{tg}) = \sum_{i,j,k,l} T_{ijkl}\, x^i_{fp} \tan^j(\theta_{fp})\, y^k_{fp}\, \tan^l(\phi_{fp}), \tag{3.9}$$

$$\tan(\phi_{tg}) = \sum_{i,j,k,l} P_{ijkl}\, x^i_{fp} \tan^j(\theta_{fp})\, y^k_{fp} \tan^l(\phi_{fp}), \text{ and} \tag{3.10}$$

$$\delta_{tg} = \sum_{i,j,k,l} D_{ijkl}\, x_{fp}^{i} \tan^{j}(\theta_{fp})\, y_{fp}^{k}\, \tan^{l}(\phi_{fp}). \tag{3.11}$$

The symmetry of the spectrometers with respect to their vertical mid-planes implies that

$$T_{ijkl} = D_{ijkl} = 0 \qquad \text{for odd} \quad k+l, \tag{3.12}$$

$$Y_{ijkl} = P_{ijkl} = 0 \qquad \text{for even} \quad k+l. \tag{3.13}$$

The trajectory and the momentum of the particle at the target is fully characterized by 5 target coordinates: y_{tg}, θ_{tg}, ϕ_{tg}, δ_{tg} and x_{tg}. The fifth coordinate x_{tg} is obtained by combining the first-order trajectory given by the equations 3.9 to 3.11 with the beam position information. Then θ_{tg} and δ_{tg} are corrected for non-zero x_{tg} (described below).

It is important to realize that even with the beam position centered exactly at (0,0) in the hall coordinate system (HCS), for extended targets the x_{tg} coordinate of the trajectories can be quite large[1] [27], leading to relatively large corrections to θ_{tg} and δ_{tg}. The x_{tg} corrections are linear in the first order: $\Delta\theta_{tg} = \alpha x_{tg}$, $\Delta\delta_{tg} = \beta x_{tg}$, and therefore asymmetric with respect to x_{tg}.

3.5 Spectrometer mispointings

The E89-044 Experiment required an accurate knowledge of the spectrometer angles and the mispointing of the dipole axis. During this experiment, six important surveys of the spectrometer positions and target position were performed.

A complete report on the spectrometer setting can be found in [34]. We will present the survey measurements compared to EPICS results and pointing analysis.

Each of the two high resolution spectrometers ideally would have just one spatial

[1] This is because the z_{tg} = 0 plane does not coincide with the vertical HCS yz plane that contains the unrastered beam, except for 90° lab scattering angle.

degree of freedom – rotational around the center of the hall, with the spectrometer central rays going through the hall center. In reality, although ‘pitch’ (the angle between a horizontal plane and the Q1 optical axis) and ‘roll’ (the rotational angle around the Q1 optical axis) displacements were negligible, a translational movement of the spectrometers caused the central rays to miss the hall center in the horizontal direction up to 3 mm and in the vertical direction up to 0.5 mm. These movements were not reproducible, i.e. at the same angular location at a different time each spectrometer could have a different ‘horizontal pointing’ (the horizontal distance between the spectrometer central ray and the hall center; the horizontal pointing is also known as the ‘spectrometer misspointing’) and vertical offset. Two reliable methods of measurement of these displacements were available:

1. A survey of the spectrometers, giving both the horizontal pointing and the vertical offset.

2. The calculation of the horizontal pointing from the position of the carbon foil along the beam reconstructed by a spectrometer (and a knowledge of the location of the carbon foil target; "pointing" runs with an unrastered beam and the carbon foil as the target were made at many kinematic settings).

The most precise information came from the surveys, which were performed several times during the experiment. In particular, the electron spectrometer location (which was fixed most of the time) at the 4.8 GeV and 1.2 GeV kinematics, as well as the location of the hadron spectrometer at several kinematic settings, was determined from the surveys. For the spectrometer settings for which the surveys were not available, the horizontal pointing was calculated using the carbon "pointing" runs, as outlined below.

3.5.1 Surveys, MEDM and Pointing results

The first survey of the two spectrometers was performed in December 12, 1999. Two other surveys were performed on February 2 and 24, 2000 and two on March 13 and 15th, 2000.

In these surveys (See Fig. 3.4), the spectrometer angles and offsets were measured; the results are reported in table 3.2. Also reported in the table are the angles and offsets given by MEDM reading (EPICS) and those obtained by the pointing analysis.

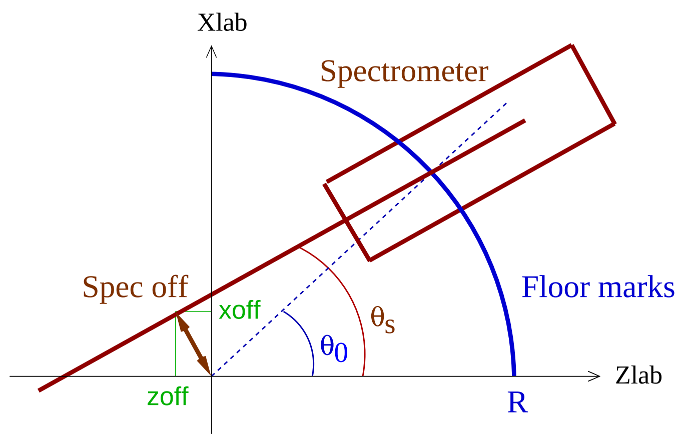

Figure 3.4: Definition of variables.

For MEDM (motif editor and display manager, a motif graphical user interface for designing and implementing control screens), the spectrometer offsets are the results of the LVDT (linear variable differential transformer) measurements. The LVDT principle of measurement is based on magnetic transfer which also means that the resolution of LVDT transducers can be made arbirarily precise. The smallest amount of movement can be detected by suitable signal conditioning electronics. Spectrometer angles are reproduced, with this method, using these offsets and the ideal central angles, from the formula:

$$\theta_s = \theta_0 \pm \frac{Sp_{offMEDM}}{R}\frac{180}{\pi} \tag{3.14}$$

where:

- θ_s is the spectrometer angle reported in the MEDM screen,
- θ_0 the central angle, and
- R is the distance from the center to the front jack of the dipole, R = 8.458 m.

The central angles are calculated using floor mark information:

$$\theta_0 = \theta_{floor} + \frac{Ver}{VerC} + \theta_{0off} \tag{3.15}$$

where:

- Ver is the Vernier,
- $VerC$ is the Vernier Caliber, equal to 173.5 mm/deg, and
- θ_{0off} is the angle offset, equal to -0.179^o for electron arm and 0.197^o for hadron arm.

During the month of December, spectrometer offsets given by EPICS are very different from those measured during the surveys. This is because, during this period, LVDTs did not measure the correct distances since they had been bumped by accident when the hall was open.

We have also calculated the spectrometer offsets and reproduced the angles using the carbon pointing method. For this method, we have used the target position offsets measured during some surveys, and summarized in Table 3.1.

The carbon pointing method is illustrated in Fig.s3.5 and 3.6. Spectrometer offsets are given by the formula:

$$Spec_{off} = y_{tg} - tg_{off} \cdot \sin\theta_s \tag{3.16}$$

Here, y_{tg} is the non-dispersive position, perpendicular to the spectrometer optic axis and calculated by ESPACE for each setting.

Table 3.1: Position of the carbon target.

period	target offset
.. - 10 Dec.	-1.2 mm
11 Dec. - 13 Dec.	+0.66 mm
13 Dec. - 23 Dec.	-0.8 mm
.. - 18 Feb.	-0.86 mm
25 Feb. - ..	-0.23 mm

During the month of March, we can note the spectrometer offsets calculated by pointing for runs 2718 and 2719 have different values from those of the 2778, 2779 and 2780. In fact, between these two settings, the end station refrigerator (ESR) tripped and all spectrometer magnet currents were set to zero; see halog entry 36194.

A survey was performed before run 2778, the y_{tge} variable for this run is plotted in Fig. 3.7, and we can see, from the table, that there is a good agreement between the offsets measured by this method and those calculated by pointing method.

The spectrometer angles, θ_s, were then calculated using these spectrometer offsets:

$$\theta_s = \theta_0 \pm \frac{Sp_{off}(Pointing)}{R} . \frac{180}{\pi} \tag{3.17}$$

where θ_0 is the central angle calculated using the floor marks information; see equation 3.15.

Uncertainty studies of these three methods are summarized below:

- In surveys, spectrometer offsets are measured with about 0.5 mm of accuracy and the precision for the angles is 0.003° [35].

- The angles given by MEDM are good to within 0.012°. Concerning spectrometer offsets, a final estimation is difficult to do, because it depends on how much attention is accorded to the LVDT measurement [36].

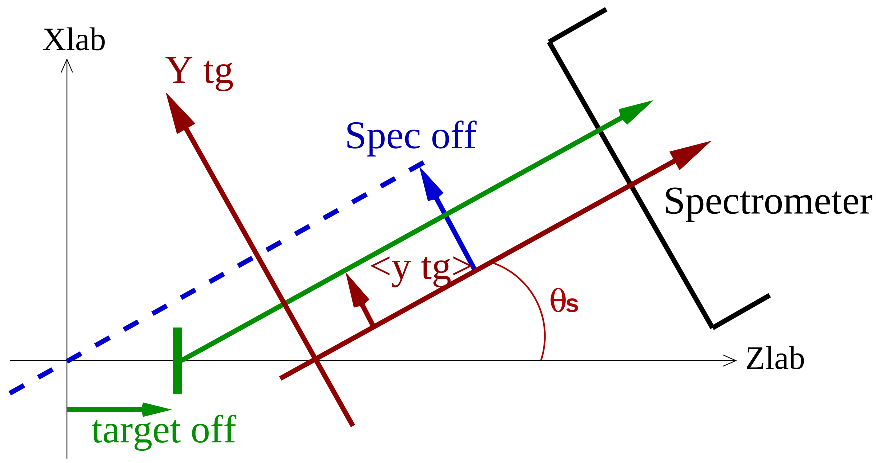

Figure 3.5: Definition of pointing variables for electron arm.

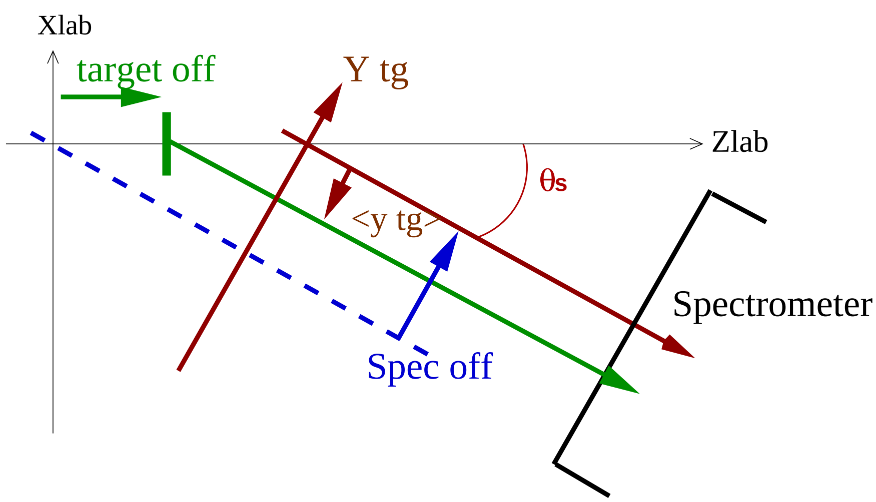

Figure 3.6: Definition of pointing variables for hadron arm.

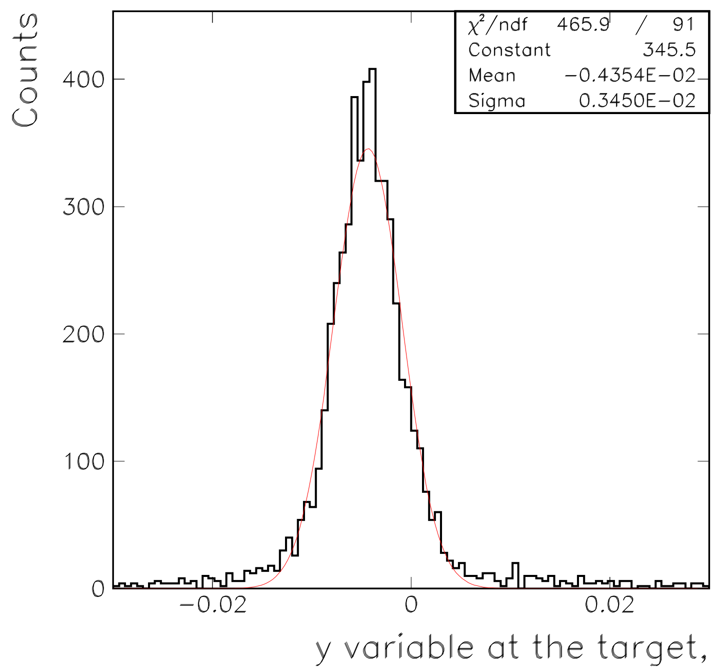

Figure 3.7: The y variable at the target for run number 2778.

- Spectrometer offsets measured by pointing method have $\pm$ 0.5 mm of uncertainty. Thus, from equation 3.15, the precision of the spectrometer angles calculated by this method is 0.015°.

In summary, we have presented the results of the spectrometer settings during the E89044 experiment. We checked that pointing results are in a good agreement with survey measurements. For the kinematics for which we do not have surveys, we can use the carbon pointing method to get the correct spectrometer offsets and angles to use in analyzing the data.

Table 3.2: Comparison of offsets and angles from MEDM, survey and pointing techniques.

	Survey	MEDM	Pointing	Survey	MEDM	Pointing
$\theta_{\mathrm{e/h}}(^\circ)$ $\mathrm{Spec}_{\mathrm{off}}$ (mm) Date	16.523 2.56 12/04/99	16.524 2.6	16.54 2.29 12/12/99	16.553 -2.92 12/04/99	16.557 -3	16.557 -3.021
$\theta_{\mathrm{e/h}}(^\circ)$ $\mathrm{Spec}_{\mathrm{off}}$ (mm) Date		15.487 2.	15.489 1.56 12/17/99		25.207 -1.1	25.209 -1.29
$\theta_{\mathrm{e/h}}(^\circ)$ $\mathrm{Spec}_{\mathrm{off}}$ (mm) Date		31.033 4.	31.038 3.17 12/17/99		25.207 -1	25.199 -1.289
$\theta_{\mathrm{e/h}}(^\circ)$ $\mathrm{Spec}_{\mathrm{off}}$ (mm) Date	16.383 2.74 02/22/00	16.363 5.34	16.384 2.267 02/26/00	69.793 -0.15	69.795 -0.81	69.800 -0.844
$\theta_{\mathrm{e/h}}(^\circ)$ $\mathrm{Spec}_{\mathrm{off}}$ (mm) Date	118.704 2.34 3/13/00	118.393 4.31	118.703 2.86 3/09/00	30.580 0.51	30.586 0.7	30.588 0.297
$\theta_{\mathrm{e/h}}(^\circ)$ $\mathrm{Spec}_{\mathrm{off}}$ (mm) Date	118.704 2.34 3/13/00	118.693 4.31	118.703 2.793 3/09/00	30.580 0.51 3/15/00	30.586 0.7	30.588 0.255
$\theta_{\mathrm{e/h}}(^\circ)$ $\mathrm{Spec}_{\mathrm{off}}$ (mm) Date	118.704 2.34 3/13/00	118.694 4.25	118.707 2.411 3/17/00	25.484 -3.3 3/15/00	25.483 -2.910	25.483 -2.935
$\theta_{\mathrm{e/h}}(^\circ)$ $\mathrm{Spec}_{\mathrm{off}}$ (mm) Date	118.704 2.34 3/13/00	118.694 4.25	118.706 2.552 3/17/00	25.484 -3.3 3/15/00	25.483 -2.910	25.483 -2.831
$\theta_{\mathrm{e/h}}(^\circ)$ $\mathrm{Spec}_{\mathrm{off}}$ (mm) Date	118.704 2.34 3/13/00	118.694 4.25	118.706 2.553 3/17/00	25.484 -3.3 3/15/00	25.483 -2.910	25.483 -2.88

3.6 Computer and electronic dead time

Two kinds of dead time are taken into account in the analysis; electronic dead time (edt) and computer dead time (cdt). These dead times occur when the electronics or the acquisition systems are not able to read the incoming events.

3.6.1 Computer dead time

The computer deadtime arises due to the inability of the DAQ system to record events occurring during a DAQ 'dead time', when it is already recording another event. The computer deadtime is calculated, for each type of event i (i = 1,...,5), from the total number of events of each type which are counted by scalers. This allows one to correct for the number of non-recorded events. For trigger type i, prescaled with an integer prescale factor ps_i (i.e. when the DAQ is set to record every ps_ith event of type i), the computer deadtime $\epsilon_{cdt,i}$ for the E89044 trigger setup can be computed as [37]

$$\epsilon_{cdt,i} = 1 - \frac{T_i ps_i}{S_i'}, \quad i = 1, ..., 5, \tag{3.18}$$

$$S_i' = S_i, \quad i = 2, 4, 5, \tag{3.19}$$

$$S_i' = S_i - S_5 - N_{14}, \quad i = 1, 3 \tag{3.20}$$

where S_i is the end-of-run scaler count for trigger type i, and T_i is the number of recorded events of type i. The subtraction of S_5 and N_{14} from S_1 and S_3 in formula (3.15) is necessary, since, in the trigger setup used, the S_1 and S_3 scalers over counted the number of the singles triggers by the number of the coincidence triggers (S_5) and the number of triggers type 14 (N_{14}). The trigger type 14 occurred (very rarely) when there was an overlap of 10 ns or less between different triggers at the trigger supervisor. The prescale factor for the coincidence trigger (P_5) was set to 1 in all measurements. In cross section measurements, the computer deadtime was kept below 20% by prescaling the singles triggers or an adjustment of the beam current.

3.6.2 Electronic dead time

The electronic dead time is a result of a superposition of two or several signals, given the non-zero time widths of digital signals. It is only significant if the rates are very high; only one signal is taken into account, and the number of events counted by the scalers decreases. The electronic dead time for the E89044 trigger setup was thoroughly studied by M. Jones and R. Michaels [37], during the E91011 (‘N-delta’) experiment in the summer of 2000. They introduced into the E91011 datastream artificial triggers, caused by a pulser sending scintillator-type signals to a linear OR with the paddle signals in both scintillator planes of both spectrometers, thus imitating the regular physics triggers occurring during the data acquisition. The ratio of the number of the recorded events of this type (discriminated from the rest of the data by a tag in a TDC channel), corrected for the computer deadtime and prescaling, to the number of issued pulser-type triggers, yielded the electronic dead time. The electronic deadtime found with this procedure for the coincidence trigger, for a wide range of the sum of the strobe rates in the electron and hadron spectrometers, is plotted in Fig.3.8. A linear parametrization of the electronic deadtime for trigger types 1, 3 and 5 was then obtained [37]:

$$edt_i = 1.9 \cdot 10^{-4} \cdot R_i^S, \qquad i = 1, 3, 5, \tag{3.21}$$

were edt_i is the electronic deadtime of trigger type i, R_1^S and R_3^S are the strobe rate in electron and hadron spectrometers, respectively, and $R_5^S = R_1^S + R_3^S$ is the total strobe rate. The strobe rates are in KHz.

The strobe rates in the electron and hadron spectrometers can be found from the

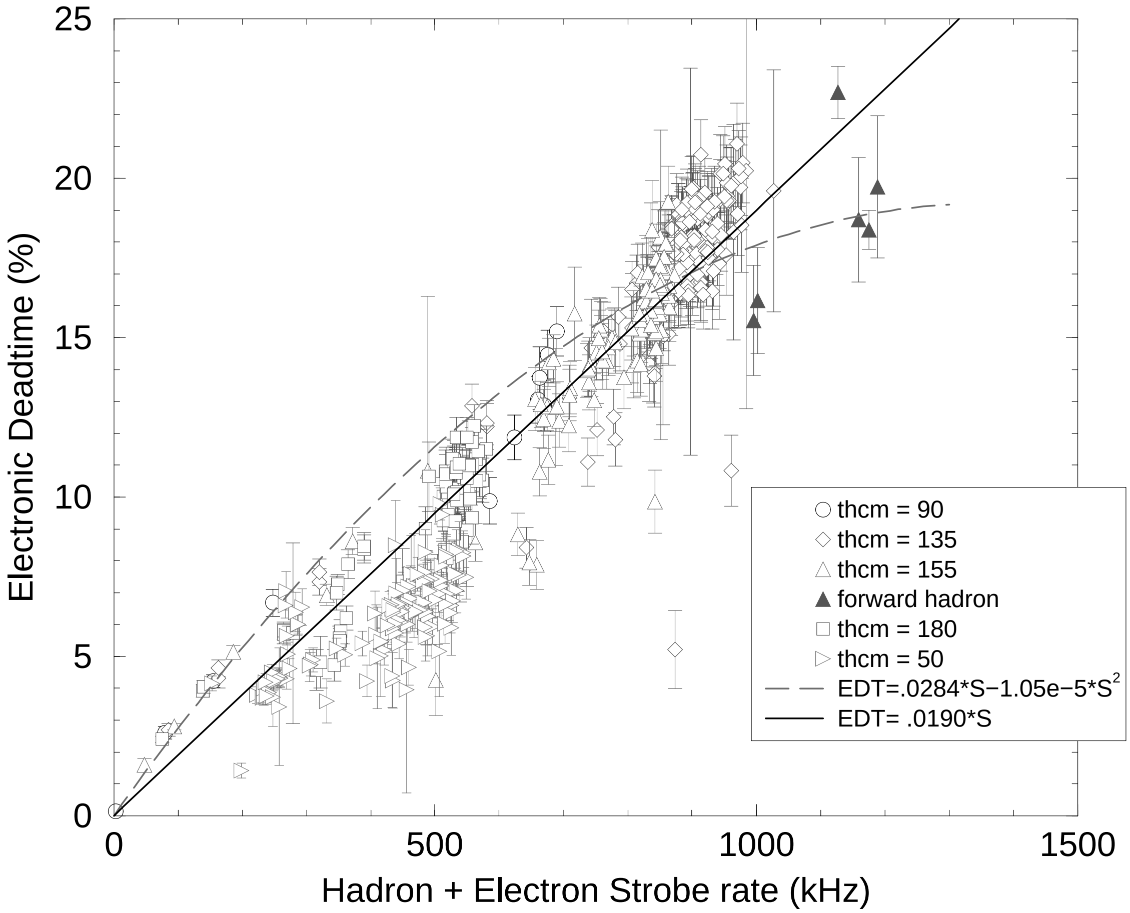

Figure 3.8: Electronic deadtime measured at different values of the sum of the strobe rates in the spectrometers. Figure courtesy of M. Jones [37].

rates of signals in the scintillator paddles, as

$$R_1^S = (0.613 \pm 0.001) \cdot \sum_{j,k} R_{j,k,1}, \quad j = 1, ..., 6, \quad k = 1, 2, \tag{3.22}$$

$$R_3^S = (0.620 \pm 0.0007) \cdot \sum_{j,k} R_{j,k,3} - (5.1 \pm 0.04)10^{-5} \cdot (\sum_{j,k} R_{j,k,3})^2, \tag{3.23}$$

$$j = 1, ..., 6, \quad k = 1, 2,$$

where $R_{j,k,1}$ ($R_{j,k,3}$) is the rate of pulses in the right phototube of paddle j in scintillator plane k of the electron (hadron) spectrometer.

3.6.3 Total deadtime

The electronic and computer deadtimes are combined as:

$$DT = 1 - (1 - cdt)(1 - edt) \tag{3.24}$$

to yield to the total deadtime DT for each trigger type. The total deadtime correction applied to the data is expressed in term of $\frac{1}{1-DT}$.

For the highest strobe rates in the ^{3}He(e,e′p) measurements, at kinematics 14, the electronic deadtime was $\sim$ 16%, with the sum of the strobe rates $\sim$ 830 kHz, and the absolute systematic uncertainty was $\sim$ 1.6% due to correcting for the electronic deadtime. At a majority of the spectrometer settings, however, the electronic deadtime and the systematic uncertainty associated with correcting for the deadtime were much smaller. The systematic uncertainty of the calculated computer deadtime is $\sim$ 10% (relative) error [38].

Chapter 4
Data Analysis

4.1 Overview

In this chapter the major elements of the $(\mathrm{e}, \mathrm{e}'\mathrm{p})$ analysis are presented and discussed. Scattered electrons from the $^3\mathrm{He}(\mathrm{e}, \mathrm{e}'\mathrm{p})$ reaction were detected in the HRSe in coincidence with recoil protons in the HRSh. This chapter will discuss the detection of these particles and how their information at the target is reconstructed, the identification of each particle, the extraction of the cross section and the effective density distributions along with the transverse-longitudinal asymmetries A_{TL}.

The data analysis code ESPACE [27] was used to analyze the raw data, producing histograms of the measured counts after various cuts for background suppression and subtraction. A raw missing energy spectrum is presented in Fig. 4.1. Note the importance of the background before any software cut is applied. Figure 4.2 represent the same data after selection of the real coincidence events, rejection of target wall contributions, and acceptance studies.

The Monte Carlo code MCEEP [39] was used to calculate the corresponding detection phase-space volume. External and internal radiative corrections were applied by radiatively unfolding the cross section; the radiative correction program is introduced in the simulation. The main steps of this analysis are discussed in detail in the following sections.

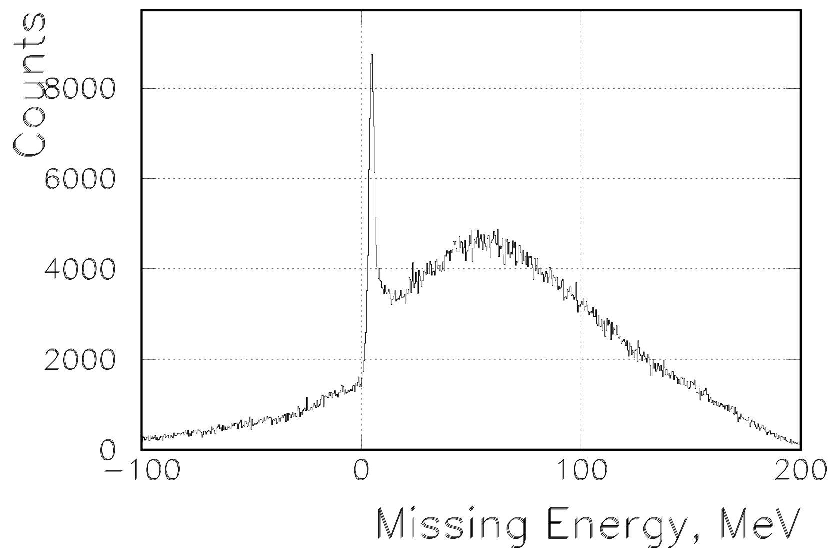

Figure 4.1: Raw missing energy spectrum for kinematics 13, as defined in Table 1.1 .
.

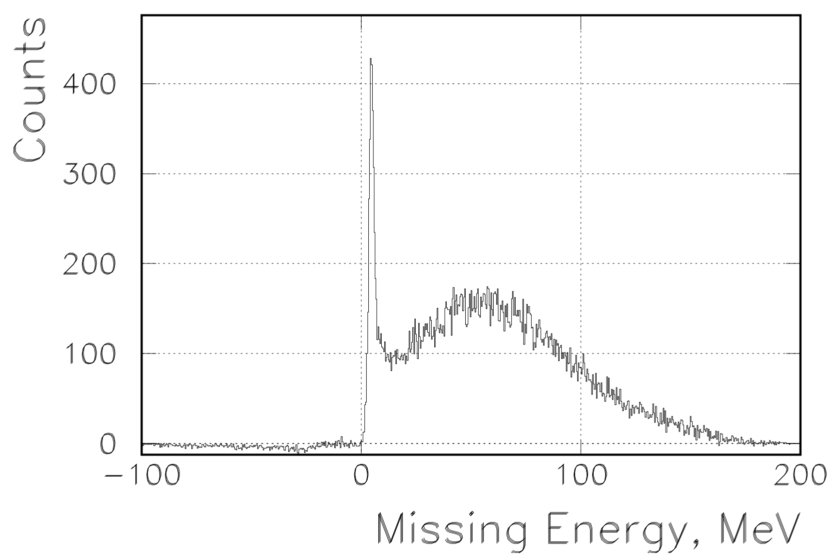

Figure 4.2: Missing energy spectrum for kinematics 13 after accidental and target walls subtraction, and acceptance cut.

4.2 Coincidence time of flight

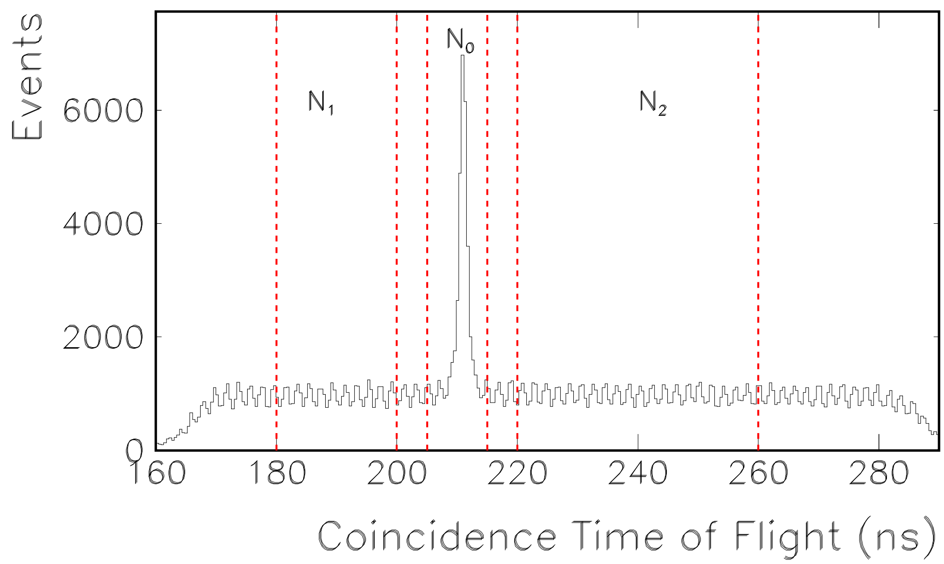

Figure 4.3: Corrected coincidence time-of-flight spectrum. Note the 2 ns structure due to the 499 MHz micro structure of the electron beam.

For coincidence events, the time between the two spectrometer triggers corresponds to the difference in the flight times through the spectrometers of the detected electron and the proton. Since the particles detected in this experiment are relativistic and the range of the proton momenta was narrow, the time-of-flight for a true coincidence event should lie in a narrow range; see Fig. 4.3.

For each kinematic bin, the number of true coincidence events N_t was determined with the formula

$$N_t = N_0 - \frac{\Delta t_0 (N_1 + N_2)}{\Delta t_1 + \Delta t_2} \tag{4.1}$$

where N_0 is the number of events within the bin reconstructing in the real coincidence window Δt_0, and N_1 and N_2 are the number of events within the bin reconstructing in the accidental coincidence windows Δt_1 and Δ_{t_2}, respectively. Statistical uncertainties were propagated as

$$\delta N_t = \sqrt{N_r + (N_1 + N_2)} \left(\frac{\Delta t_0}{\Delta t_1} + \Delta t_2 \right)^2 . \tag{4.2}$$

Widths of the windows varied between kinematic settings, with wider accidental and more narrow real coincidence windows at settings with a higher relative rate of accidental coincidence events.

Care was taken to exclude real coincident (e,e$'\pi^+$), (e,e$'\,^2$H) and (e,e$'\,^3$H) events from the windows.

4.3 Cut on target length

The reconstruction of the reaction point along the beam by the two spectrometers in the laboratory system shows two peaks corresponding to the particles scattered from the aluminium walls. The real diameter of the tuna can is 10.32 cm, while the distance between the two peaks in Fig. 4.4 and 4.5 is very close to 10.30 cm for both spectrometers, signifying a good reconstruction of the reaction point by the two spectrometers.

Contributions from the aluminum target walls were removed by imposing the cut $|\mathrm{z_{lab}}| < 3.5\ \mathrm{cm}$ on the reaction point along the beam reconstructed by the spectrometer positioned at larger scattering angle.

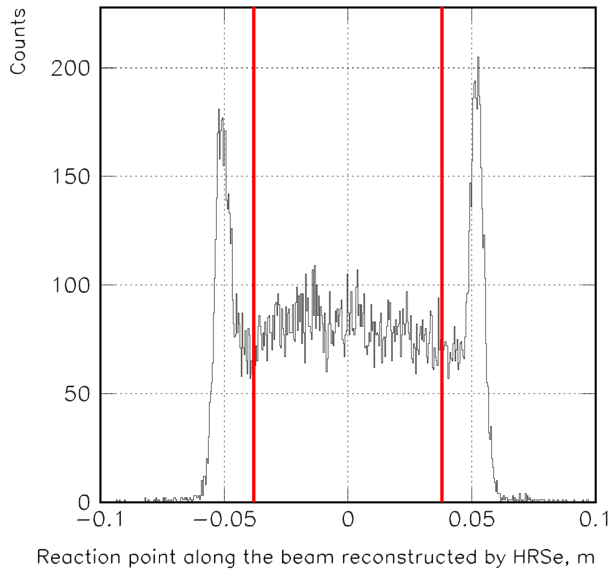

Figure 4.4: Reaction point along the beam reconstructed by the electron spectrometer at kinematics 13 for coincidence events.

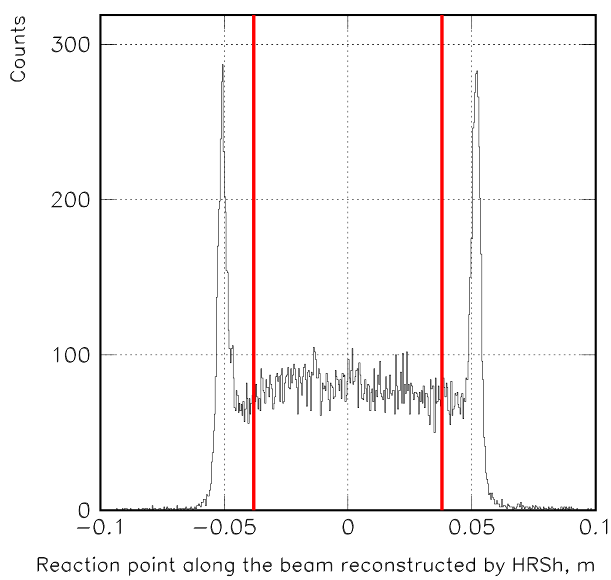

Figure 4.5: Reaction point along the beam reconstructed by the hadron spectrometer at kinematics 13 for coincidence events.

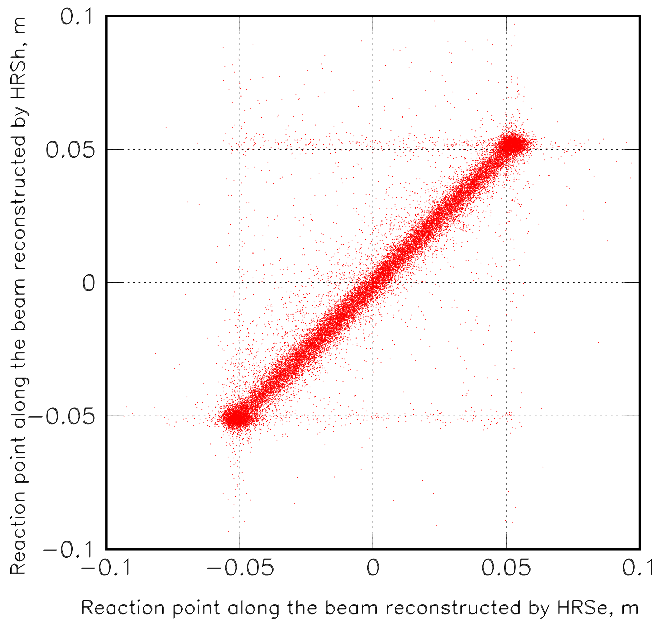

Figure 4.6: Reaction point along the beam reconstructed by the two spectrometers at kinematics 13 for coincidence events. True $^3\mathrm{He}(\mathrm{e},\mathrm{e}'\mathrm{p})$ coincidences are contained in the diagonal band of events.

Figure 4.6 shows the distribution of the reaction point along the beam reconstructed by the hadron spectrometer, z_{labh}, versus the distribution of the reaction point along the beam reconstructed by the electron spectrometer, z_{labe}, for coincidence events detected at kinematics 13. The real coincidence events are located along the diagonal $z_{labe} = z_{labh}$. The cut on the difference between the reconstructed reaction points, $|z_{labe} - z_{labh}| < 2$ cm for Σ_1 and Σ_2 kinematic settings, and the cut $|\mathrm{z_{labe}} - \mathrm{z_{labh}}| < 2.5$ cm for Σ_3 kinematic settings, were used for the rejection of most of the accidental coincidences.

4.4 Particle identification

To ensure that the particles we detected were indeed $(\mathrm{e},\mathrm{e}'\mathrm{p})$ events, the particle identification was checked in each of the two spectrometers.

In the HRSe, pions were rejected by the Cerenkov detector, which uses carbon dioxide as a radiator gas.

For the proton spectrometer, HRSh, the energy deposited in the scintillator S0 allowed the rejection of pions and deuterons detected in coincidence with the electrons. These particles can be separated from the protons by the scintillator ADC spectra: an ADC on each phototube provided a measure of the energy deposited in the scintillator. A plot of ADC values versus the particle time of flight is presented in Fig. 4.7. In addition to a central proton peak, a number of other distinct regions are visible in the scatter plot. Heavier particles deposit more energy in the scintillators, and have smaller velocities. Fig. 4.7 shows the total energy deposited by a particle in the scintillator S0 versus its time of flight.

- A triton region, appearing at high dE and very low time of flight β values. Kinematically, these tritons can only come from the interaction with the Aluminum target walls.
- A deuteron region, appearing at high dE and low time of flight (TOF) values. A few of the deuterons are true coincidences, and appear as a small peak in the coincidence time of flight spectrum.
- A proton region that we need to select for the cross section measurements.
- A pion region, appearing around $\beta = v/c = 1$.

4.5 Phase-space volume calculation

Not all the events being detected contribute to the cross section measurements. Each High Resolution Spectrometer (HRS) does not have a simple acceptance. In fact, and as an example, the dipole magnet has a trapezoidal cross section and the higher momentum particles tend to pass closer to its shorter base side, where the magnetic field

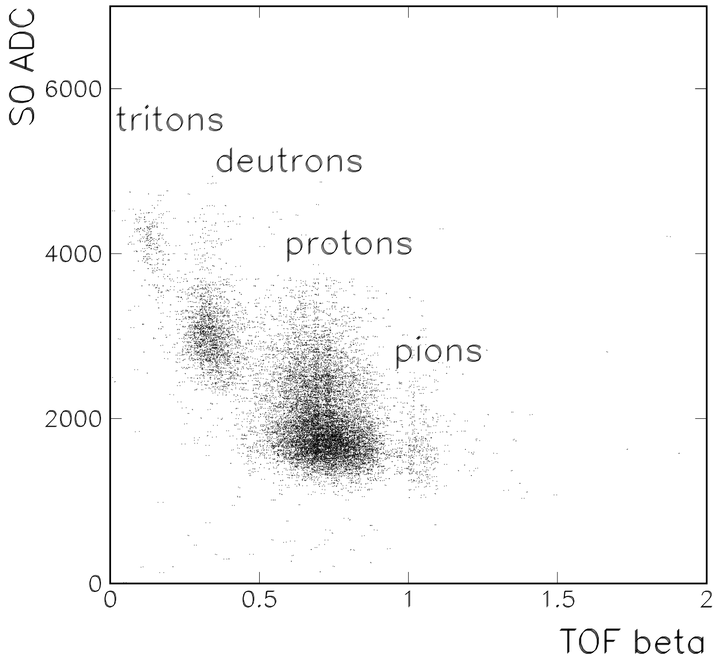

Figure 4.7: Energy deposited by a particle in the S0 scintillator versus its time of flight.

is stronger. This causes a decrease of the accepted range of ϕ_{tg} when δ_{tg} increases. Increasing y_{tg} requires decreasing ϕ_{tg}, and vice versa, in order for the particles to enter the spectrometer through the entrance window. See Fig. 4.8.

To define the boundaries of the HRS acceptance and make an efficient selection of the good events, an acceptance boundary function has been developed for such a purpose using the "R-function" method [40]. The R-function reduces all the cuts to one single cut.

4.5.1 R-function

An R-function is a real-valued function whose sign is completely determined by its arguments. An R-function can be used to define a geometric object by the boundary equation of the shape of this object. The resulting function is equal to zero on the boundary of the geometrical object, greater than zero inside the object and less than zero outside the object. For example, the function $f(x, y) = 1 - (x^2 + y^2)$ can be considered as an R-function defining a circle with a radius of one, since f is equal to zero on the circle, larger than zero inside the circle and less than zero outside the circle. With a given x_{tg}, the spectrometer acceptance is a 4-dimensional region of variables θ_{tg}, ϕ_{tg}, δ_{tg} and y_{tg}. Its main features can be seen in the (ϕ_{tg}, θ_{tg}), (ϕ_{tg}, δ_{tg}), (ϕ_{tg}, y_{tg}) and (θ_{tg}, ϕ_{tg}) distribution of each arm that cover a maximum acceptance possible; see Fig. 4.8. The boundaries of the acceptance are defined as RF > 0. For the E89044 experiment we chose to use the cut RF > 0.002 to define the flat region of the acceptance and to select good events in both simulation and data; see Fig. 4.9 and 4.10.

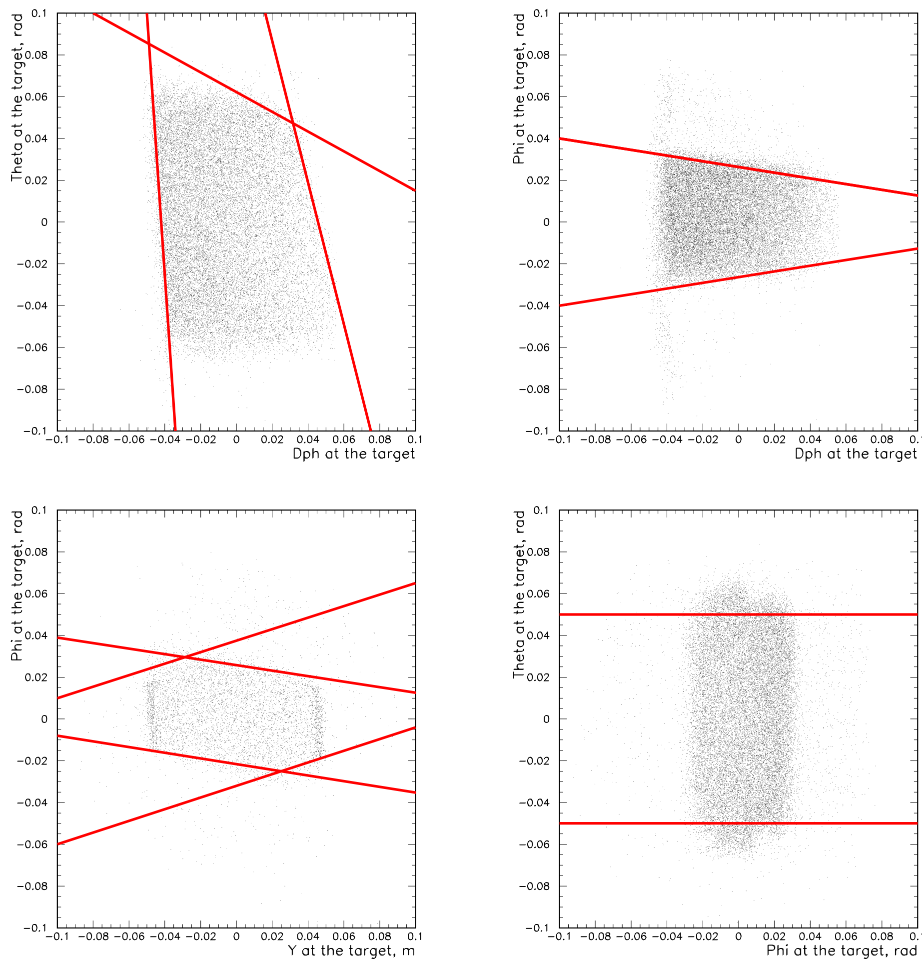

Figure 4.8: Contour plots of the proton singles distributions covering the hadron spectrometer acceptance. Upper left: θ_{tg} vs δ_{tg}, Upper right: ϕ_{tg} vs δ_{tg}. Lower left ϕ_{tg} vs y_{tg}, lower right: θ_{tg} vs ϕ_{tg}. The solid red lines indicate the edges of the initial cut placed on the acceptance.

4.6 Recorded data

The $^3\mathrm{He}(\mathrm{e},\mathrm{e}'\mathrm{p})$ kinematics analyzed in this thesis are summarized in Table 1.1. The data were collected at two values of beam energy, 4.806 GeV and 1.2553 GeV. At each beam energy, electron were detected in the HRSe at a fixed scattering angle and momentum. Kinematics are centered at the quasielastic knockout of protons with transferred momentum $\mathrm{q} = 1.5\ \mathrm{GeV/c}$ and transferred energy $\omega = 837\ \mathrm{MeV}$.

The knocked out proton was detected in coincidence with the ejected electron in the HRSh, in perpendicular coplanar $(\mathrm{e},\mathrm{e}'\mathrm{p})$ kinematics.

Two dimensional plots of missing momentum versus missing energy for the recorded data are represented in Figs. 4.11, 4.12 and 4.13.

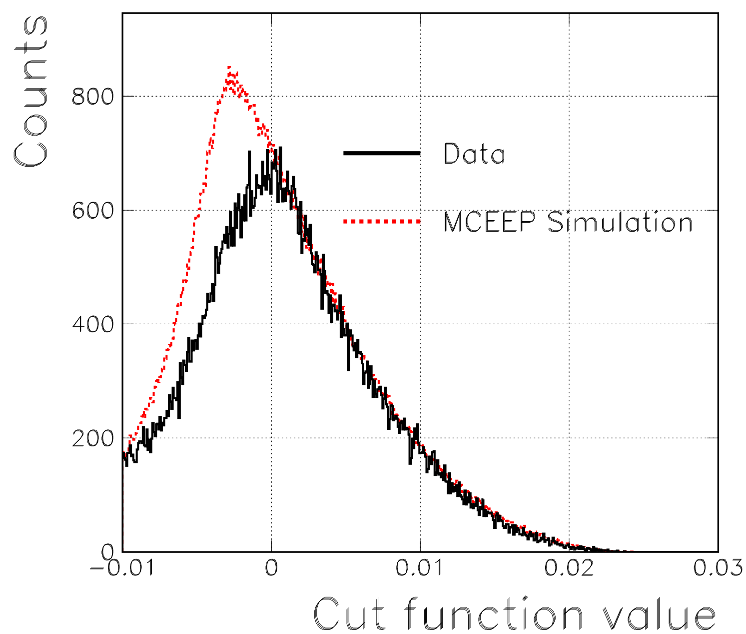

Figure 4.9: Distribution of the cut function for data (full histogram) and simulation (dotted histogram) at kinematics 10.

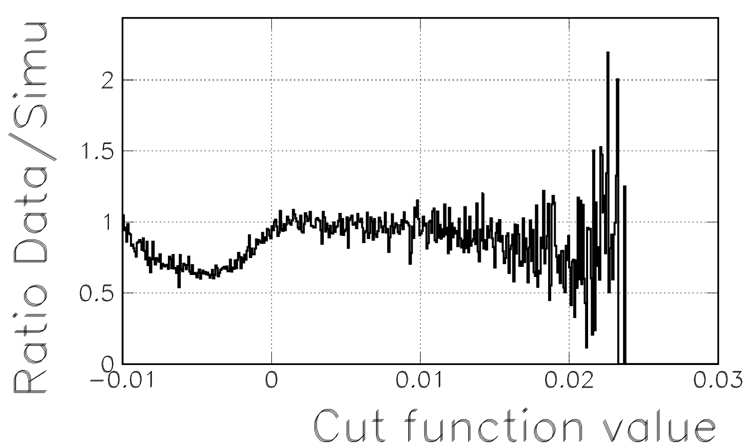

Figure 4.10: Ratio of the previous two cut function histograms (data over simulation).

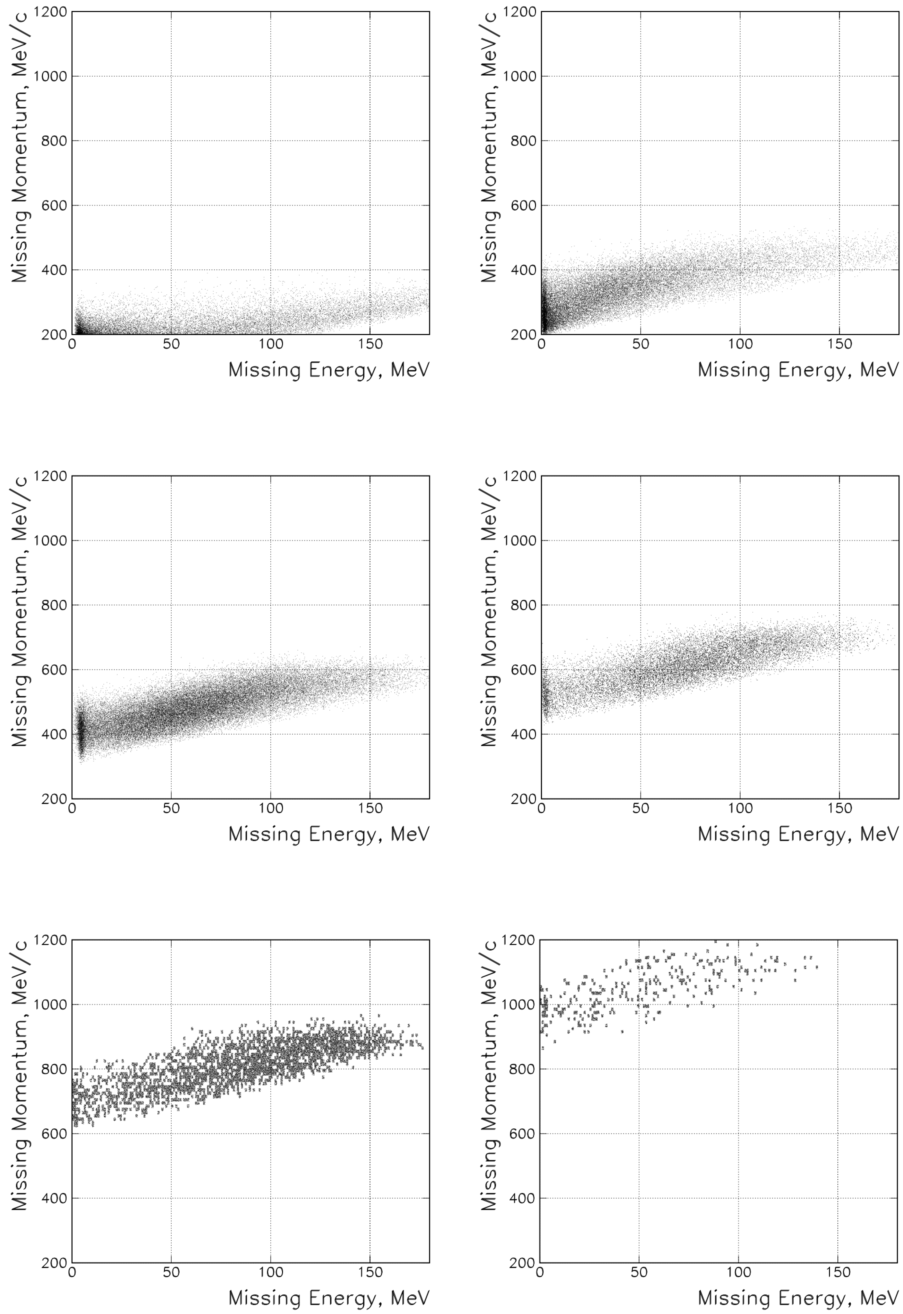

Figure 4.11: The range of missing energy and missing momentum spanned by the $^{3}\mathrm{He}(\mathrm{e},\mathrm{e}'\mathrm{p})$ measurements in each of the Σ_1 perpendicular kinematics. The beam energy is 4.8068 GeV and $\epsilon = 0.943$. The order of the kinematics is as follows: upper left kin4, upper right kin7, center left kin10, center right kin13, lower left kin28, and lower right kin29.

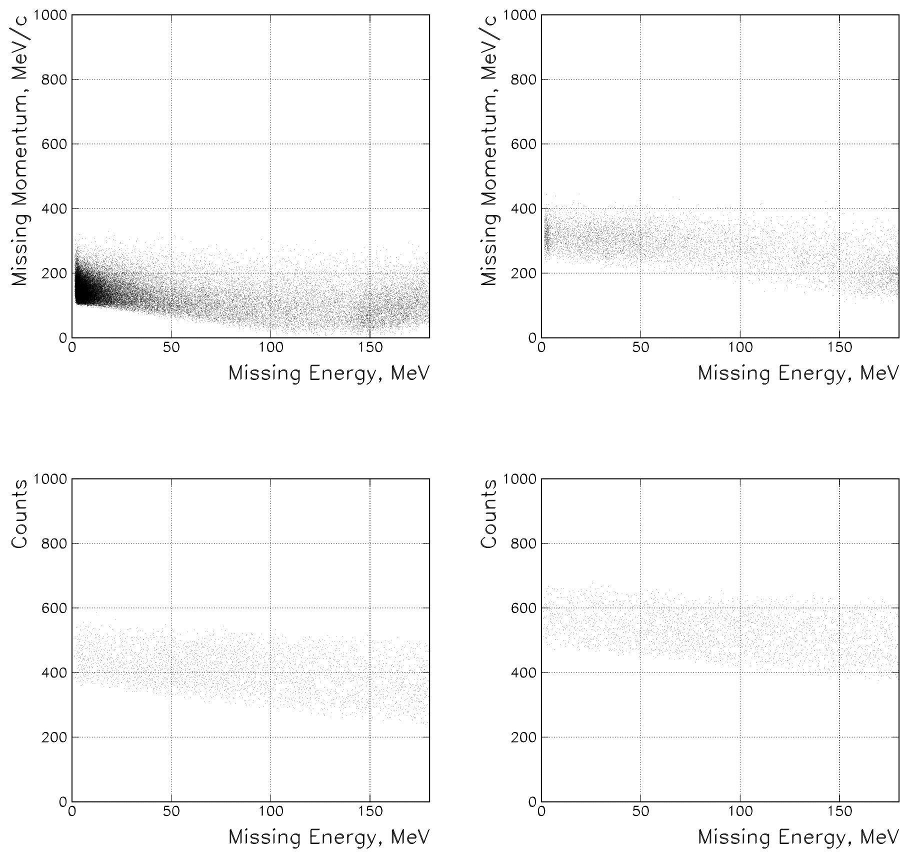

Figure 4.12: The range of missing energy and missing momentum spanned by the $^{3}\mathrm{He}(\mathrm{e},\mathrm{e}'\mathrm{p})$ measurements in each of the Σ_2 perpendicular kinematics. The beam energy is 4.8068 GeV and $\epsilon = 0.943$. The order of the kinematics is as follows: upper left kin5, upper right kin8, lower left kin11, and lower right kin14.

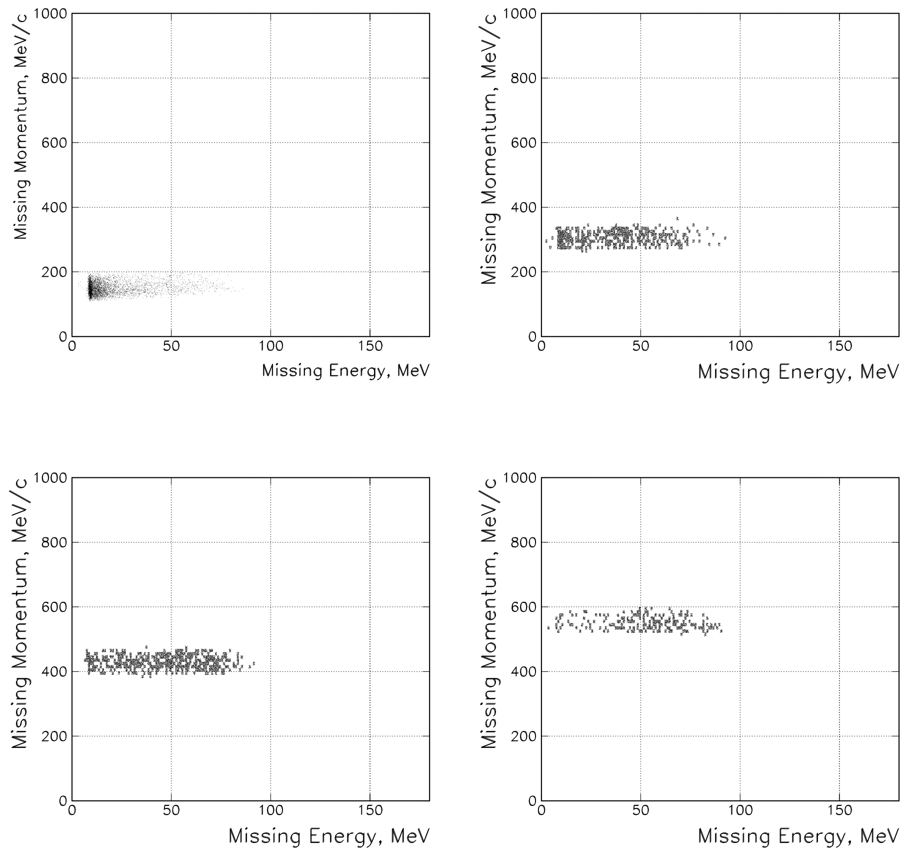

Figure 4.13: The range of missing energy and missing momentum spanned by the $^3\mathrm{He(e,e'p)}$ measurements in each of the Σ_3 perpendicular kinematics. The beam energy is 1.254 GeV and $\epsilon = 0.108$. The order of the kinematics is as follows: upper left kin6 upper right kin9, lower left kin12, and lower right kin15.

.

4.7 Normalization of the data

The extraction of the $^{3}\mathrm{He(e,e'p)}$ cross section requires a precise knowledge of integrated luminosities during the runs. The total cross section, σ, of the scattering into a kinematical bin, not corrected from radiative effects, is directly related to the integrated luminosity by the relation

$$\sigma = \frac{N}{\epsilon_{\mathit{eff}}} \frac{1}{\int L dt}, \tag{4.3}$$

where N is the number of events detected in the kinematic bin during the run, and ϵ_{eff} is a factor accounting for prescaling and the efficiency of particle detection.

The integrated luminosity for electrons of a total charge Q passing through a ^{3}He gas target of length l and density ρ, is given by:

$$\int L dt = \frac{Q}{e} \frac{N_A \rho}{A_{^3He}} l, \tag{4.4}$$

where: $e = 1.602 \cdot 10^{-19}$ Coulomb is the electron charge, $A_{^3He} = 3.016$ g/mole is the atomic mass of ^{3}He, and $N_A = 6.022 \cdot 10^{23}$ mole^{-1} is Avogadro's number.

For a given target nucleus and charge of incident particles, the integrated luminosity can also be expressed in units of [Coulomb·g/cm^2].

The charge Q passing through the ^{3}He target during a run is measured with a high precision from the two beam current monitors (BCMs) for which the upstream **u** and downstream **d** signals are integrated. For small currents, < 80 μA, the amplified signals **u3** and **d3** are used:

$$Q = \frac{1}{2} . (\frac{u3}{4139} + \frac{d3}{4141}) . 10^{-6} \tag{4.5}$$

4.8 Density measurement

The target length l of the ^{3}He "tuna can" target is 10.32 cm, but it can effectively be set to a smaller value by a software cut on the reconstructed interaction point along the beam.

The density ρ of ^{3}He gas in the target can in principle be found by application of the ^{3}He equation of state to pressure and temperature readings from sensors located in the target. At a temperature of 6.3 K and pressures from 122 psi to 160 psi, as used in the experiment, however, the ^{3}He equation of state is not known with a high precision.

A more precise approach to determination of the ^{3}He density in the target is based on normalization of the measured elastic ^{3}He(e,e) cross sections to the world data [41]. The density of ^{3}He in the simulation is adjusted to reproduce the measured yield in the elastic peak, after which both the ^{3}He density and the integrated luminosity for the analyzed elastic runs is known.

If the integrated luminosity is known for a run, it can be found for other runs taken at the same beam energy with a procedure known as "luminosity monitoring". This technique is based on the fact that for a given beam energy and a spectrometer setting, the number of particles passing through a spectrometer acceptance region in a given run is to a good approximation proportional to the integrated luminosity for that run. Hence, the integrated luminosity $\int Ldt$ for an "investigated" run can be determined from the known integrated luminosity $(\int Ldt)'$ during a "reference" run, with

$$\int Ldt = \frac{N}{\epsilon_{eff}} \frac{\epsilon'_{eff}}{N'} (\int Ldt)', \tag{4.6}$$

where N and N' are the number of events satisfying a fixed acceptance cut and detected in the investigated run and in the reference run, respectively. ϵ_{eff} and ϵ'_{eff} are correction factors for efficiency of particle detection and prescaling in the investigated run and in the reference run, respectively.

Originally it was planned to determine the ^{3}He density (and the integrated luminosity) at each beam energy with elastic ^{3}He(e,e) scattering runs, with the electron spectrometer located closest to the beam dump angular position, $\approx 12.5°$ (and hence the lowest Q^2 for a beam energy, where the ^{3}He elastic form factors are known better), and then to monitor the luminosity in all other runs of the same beam energy with a spectrometer fixed during kinematics change. For beam energies of 2 – 4.8 GeV and the scattering angle of 12.5° (5 fm$^{-2} < Q^2 < 27$ fm^{-2}), the ^{3}He form factors are known with only 2 – 10% precision. It was therefore intended to improve the knowledge of the ^{3}He elastic form factors at Q^2 values corresponding to the elastic normalization runs, in a set of ^{3}He(e,e) measurements at a lower beam energy of 0.644 GeV.

This original plan of normalization of the ^{3}He(e,e′p) data was subsequently modified to include a single measurement of the ^{3}He density at the beam energy of 0.644 GeV, as the following circumstances became apparent:

- At the beam energy of 4.8 GeV the measurement of the elastic ^{3}He(e,e) cross section with a high statistical precision at low scattering angles was not feasible, since the central momentum of the electron spectrometer could not be set above 4 GeV/c.

- The ^{3}He density obtained from the ^{3}He(e,e) elastic measurements at the beam energy of 1.2 GeV and an electron scattering angle of 12.5° had a substantially higher systematic uncertainty than the density deduced from the ^{3}He(e,e) measurements at a beam energy of 0.644 GeV and an electron scattering angle of 30.8°, due to a higher sensitivity of the elastic cross sections to the scattering angle at lower scattering angles, and higher than expected uncertainty in determination of scattering angles.

- The density of ^{3}He in the target was observed to be stable to ~ 0.5% over periods of weeks; the stability of the ^{3}He target density could be further reliably monitored by temperature and pressure sensors.

4.9 $^3\mathrm{He}(\mathrm{e},\mathrm{e}')$ cross section

The $^3\mathrm{He}(\mathrm{e},\mathrm{e}')$ cross section is normalized to the world data [41] in order to extract the density of the ^{3}He target.

A first extraction of the density from the E89044 set of $^{3}\mathrm{He(e,e')}$ elastic measurements made at the beam energy of 644 MeV was performed by K. Aniol and his collaborators at Cal. State L. A. They used radiative, computer deadtime and beam heating corrections; and a PWBA calculation of the elastic cross sections, using the ^{3}He form factors from [42]. From the elastic scattering measurements at four angular settings of the electron spectrometer with 1.59 fm^{-2} $< Q^2 < 2.91$ fm^{-2}, with the hadron spectrometer used as a luminosity monitor, they obtained the density of 0.0712 g/cm^3 $\pm$ 1.3% statistical uncertainty. Later, however, an error was found in this analysis; after reanalysis, which is currently pending, their estimate of the ^{3}He density is expected to increase by $\sim$ 4%.

The ^{3}He density was also extracted by an independent method from a MCEEP simulation using the ^{3}He(e,e) elastic form factors from the Amroun *et al.* [41] fit to world ^{3}He elastic data, and a simple approximation to DWIA through the calculation of effective momentum transfer [43]. Acceptance cuts were: $|\phi_{tge}| < 20$ mr, $|\theta_{tge}| < 40$ mr, and $-0.035 < \delta_{tge} < 0.03$. Contributions from aluminum walls were removed by the reconstructed interaction point along the beam, $|reactez| < 3.5$ cm. The average ^{3}He gas density extracted was 0.07197 g/cm^3$\pm$ 1% statistical uncertainty.

4.10 Luminosity monitoring

The integrated luminosity for each run selected for the ^{3}He(e,e′p) cross section analysis was determined with the formula 4.6, which in an expanded form can be written as

$$\int Ldt = \left(\frac{N_1 P_1}{\epsilon_{cdt1}\epsilon_{edt1}\epsilon_{tr1}} + \frac{N_5 P_5}{\epsilon_{cdt5}\epsilon_{edt5}\epsilon_{tr5}}\right) \frac{(\int Ldt)'}{\frac{N_1' P_1'}{\epsilon_{cdt1}'\epsilon_{edt1}'\epsilon_{tr1}'} + \frac{N_5' P_5'}{\epsilon_{cdt5}'\epsilon_{edt5}'\epsilon_{tr5}'}}. \tag{4.7}$$

In this formula primed (′) quantities refer to the "reference" run for which the integrated luminosity is known, and unprimed quantities refer to the run for which the integrated luminosity is being measured. The notation is as follows:

- $\int Ldt$ is the integrated luminosity,

- N_i is the number of events of trigger type i passing the cut on the reconstructed reaction point along the beam, $|z_{labe}| < 3.5$ cm, and
- P_i, ϵ_{cdti}, ϵ_{edti}, ϵ_{tri} are the prescale factor, computer livetime, electronic livetime and tracking efficiency, respectively, for trigger type i.

In the formula 4.7 HRSE singles events (trigger type 1) and coincidence events (trigger type 5) are summed, and events of both types are corrected for the prescaling and efficiencies. This addition is necessary since the HRSE singles trigger and the coincidence trigger are exclusive. The HRSE trigger efficiency was stable the whole experiment and equal to 99.9%, it is therefore the the same for the reference and the investigated runs. Hence, it is canceled out in the formula 4.7.

The integrated luminosities $(\int Ldt)_i$ determined with the formula 4.7 for individual runs i taken at a ^{3}He(e,e′p) kinematic setting can be summed to give the total integrated luminosity $(\int Ldt)_{tot}$ for the kinematic setting, as

$$(\int Ldt)_{tot} = \sum_i (\int Ldt)_i. \tag{4.8}$$

The total integrated luminosity determined by 4.8 can be used in a "100% efficient" simulation of the ^{3}He(e,e′p) yield. Then, the simulated yield in a kinematic bin B can be directly compared to the number of detected events in the same bin B, if the detected events are corrected for prescaling and efficiencies. The correction for prescaling and efficiencies is made with the formula:

$$N_{tot,eff} = \sum_i \frac{N_i}{\epsilon_i}, \tag{4.9}$$

where N_i is the number of detected events in run i in the kinematic bin B, and ϵ_i is given by $\epsilon_i = \epsilon_{cdt5}\epsilon_{edt5}\epsilon_{tr5}/P_5$.

Alternatively, one can simulate the experiment with an "effective" (corrected for prescaling and efficiencies) integrated luminosity, defined as

$$(\int Ldt)_{tot,eff} = \sum_i (\int Ldt)_i \epsilon_i, \tag{4.10}$$

and then compare the yield simulated in a kinematic bin B to the number of experimentally detected in the same bin B events, uncorrected for prescaling and efficiencies:

$$N_{tot} = \sum_i N_i. \tag{4.11}$$

In fact, it can be shown that the two methods are identical (up to an insignificant multiplicative coefficient), if prescaling and efficiencies are the same for all runs at a kinematic setting. This was demonstrated in [23].

In this experiment the coincidence trigger was not prescaled, P_5 = 1, and the efficiencies of particle detection were very similar for runs taken at the same kinematic setting. Hence, both methods of calculation for the integrated luminosities and comparison of data to simulation should give identical cross section results.

In the analysis of this experiment, the second normalization approach was adopted and the calculated luminosities for the kinematics studied in this thesis are summarized in Table 4.1 [1].

4.11 Simulation of experiment

4.11.1 MCEEP

The experiment was simulated with a modified version of MCEEP [39], written by P. Ulmer with contributions from others. D. Higinbotham updated ^{3}He form factor calculation using the global fit of Amroun *et al.* [41], and coded in an approximation to DWIA through calculation of effective momentum transfer [43]. MCEEP simulates ^{3}He(e,e$'$p)d and ^{3}He(e,e$'$p)pn (three-body breakup, or 3bbu) processes separately, by 5-dimensional and 6-dimensional sampling of the phase space respectively. Ntuples simulated for the two processes are merged.

MCEEP calculates the average energy losses of electrons and protons with the

---

[1] A complete list of the runs recorded during experiment E89044 can be found in [44].

Table 4.1: Total effective luminosity used in the cross section analysis at each $^3\mathrm{He}(\mathrm{e},\mathrm{e}'\mathrm{p})$ kinematic setting.

Kinematics number	Σ	Nominal P_m, MeV/c	Number of good runs	Total effective $\int Ldt$, Coul g/cm^2
4	Σ_1	150	4	0.4855
7	Σ_1	300	15	2.2497
10	Σ_1	425	16	3.004
13	Σ_1	550	28	5.195
28	Σ_1	750	11	2.126
29	Σ_1	1000	13	2.003
5	Σ_2	150	4	0.3441
8	Σ_2	300	12	1.175
11	Σ_2	425	20	1.207
14	Σ_2	550	52	2.164
3	Σ_3	0	5	0.4245
6	Σ_3	150	11	1.767
9	Σ_3	300	31	6.031
12	Σ_3	425	31	11.57
15	Σ_3	550	53	14.15

Bethe-Bloch formula [45], with additional corrections for density and shell effects [45, 46]. Energy loss straggling is approximated by either a Landau, Vavilov, or Gaussian distribution, underway on the ratio between mean energy loss and maximum energy loss in a single collision [39]. In a final stage of event simulation, the mean energy losses of either the incident or scattered electron and protons are subtracted to allow comparison with data corrected for the mean energy losses.

Average energy losses, internal radiation and external radiations are taken into account in the simulation and are presented in detail in the next chapter, see section 5.3.

MCEEP simulates spectrometer resolutions by:

1. Transport of particles generated at the target to the focal plane, by application of spectrometer forward transfer functions [47].

2. Simulation of multiple scattering in the spectrometer exit window and air, by addition of Gaussian functions to particle transport coordinates.

3. Simulation of position resolution of VDCs.

4. Transport of particles back to the target with reverse transfer functions.

MCEEP simulates spectrometer acceptance by transport of particles to 5 internal spectrometer apertures, elimination of particles hitting the apertures, and reverse transport of particles to target. In the analysis of elastic scattering from ^{3}He (Sec. 4.9), it was found, however, that MCEEP's model of the spectrometer acceptance substantially differs from the experimentally reconstructed acceptance. Therefore, MCEEP's model of the spectrometer acceptance was not employed. Instead, in the ^{3}He(e,e$'$p) cross section analysis the acceptance was defined by software R-function cuts; see Sec. 4.5

4.11.2 Spectrometer resolution

Momentum, angular and position resolution of both spectrometers was simulated by addition of Gaussian functions to reconstructed δ_{tg}, θ_{tg}, ϕ_{tg} and y_{tg} coordinates of the particles, with FWHM [23]:

- 2 mm for y_{tg},
- 2 mr for ϕ_{tg},
- 6 mr for θ_{tg}, and
- δ_{tg}: (0.042+0.001 $\cdot$ δ_{tg}^2)% for target density 0.060 g/cm^3, but (0.045+0.001 $\cdot$ δ_{tg}^2)% for target density 0.072 g/cm^3,

where δ_{tg} is expressed in % deviation from the central momentum setting of the spectrometer.

Chapter 5

Cross Section

Five-fold differential $^3\mathrm{He(e,e'p)d}$ and six-fold differential $^3\mathrm{He(e,e'p)pn}$ coincidence cross sections were extracted by adjustments of the simple plane wave ^{3}He(e,e′p) cross section model in the simulation to reproduce the experimentally detected yield (or number of counts). In the following section, the steps of the extraction of the cross section are presented.

1. Normalization of a spectrometer setting is calculated with the luminosity monitoring procedure, and is corrected for efficiencies; see Sec. 4.10.

2. Real coincidence events are reconstructed with ESPACE [27], and the following cuts are applied:

   - VDC tracking cuts, to eliminate badly reconstructed events.

   - R-function acceptance cut, to select the events falling into flat acceptance regions of the spectrometers.

   - Cuts on the reconstructed reaction point along the beam, $|\mathrm{z_{lab}}| < 3.5\ \mathrm{cm}$, to remove contributions from the aluminum target walls.

   - A cut on the difference between reaction points along the beam reconstructed by the two spectrometers, $|\mathrm{z_{labe}} - \mathrm{z_{labh}}| < 2\ \mathrm{cm}$, to remove part of accidental coincidences was applied.

   - A cut on the sum of Gas Cerenkov ADC channels, to remove the contribution from the real coincident π^-. Cuts on shower and preshower detectors were used when needed; parallel kinematics are tended to be the more affected with pions, see [24].

- Cuts on corrected coincidence time between the spectrometers selecting the real (e,e′p) coincidence data.

3. Full MCEEP simulation of the spectrometer setting is made. The study included energy losses, internal and external radiation, multiple scattering in the target, and spectrometer resolutions. Cuts identical to those imposed on data are applied to simulated events (except for cuts on Gas Cerenkov, coincidence time of flight, particle time of flight in hadron arm and VDC tracking cuts).

4. For Σ_1 and Σ_2 kinematic settings, the position of the ^{3}He(e,e′p)d two-body breakup (2bbu) peaks reconstructed in data and in simulation are adjusted to coincide with the theoretical value of $E_{miss} = 5.49$ MeV; the continuum contribution was then moved by the same amount in the $^3\mathrm{He(e,e'p)pn}$ simulation.

5. Coincident events both in data and in simulation are binned in missing momentum P_{miss} for the $^3\mathrm{He(e,e'p)d}$ reaction channel and in missing momentum and missing energy (P_{miss}, E_{miss}) for the $^3\mathrm{He(e,e'p)pn}$ channel.

After these preliminary steps, a fitting procedure iteratively adjusted the radiated ^{3}He(e,e′p) cross sections in simulation bins until the number of counts in each bin in the simulation and the data agreed. After adjustment, the unradiated ^{3}He(e,e′p) cross sections are extracted at the vertex. These vertex cross sections are then compared to the available theoretical models.

The ^{3}He(e,e′p) cross section model used in the analysis of the continuum data was based on the factorization of the cc1 prescription for electron-nucleon cross section [19] with spectral functions fitted to data.

Full simulation of the experiment with MCEEP [39] provides two sets of kinematic variables (E_{miss}, P_{miss}, Q^2, ω and others) for each simulated ^{3}He(e,e′p) event. One set is the "asymptotic", or "radiated" kinematic variables. These variables are analogous to the experimentally reconstructed kinematic variables and are calculated based on:

- 4-momentum of the incident electron after subtraction of the mean energy losses before the interaction point.
- 4-momenta of the scattered electron and the proton after simulation of the energy losses, radiation, multiple scattering and spectrometer resolution.

Another set of MCEEP kinematic variables is named "vertex", or "unradiated" variables. The "vertex" variables are calculated on the ^{3}He(e,e$'$p) reaction vertex in the simulation. That is, these variables are calculated based on

- 4-momentum of the incident electron after simulation of the energy losses, radiation and multiple scattering and
- 4-momenta of the scattered electron and the proton before simulation of the energy losses, radiation, mulitple scattering and spectrometer resolution.

5.1 Extraction of the $^3\mathrm{He(e,e'p)pn}$ cross section

The $^3\mathrm{He(e,e'p)d}$ cross sections were extracted by M. Rvachev [23]. His method is based on normalizing the vertex $^3\mathrm{He(e,e'p)d}$ cross section bin by bin on P$_{miss}$ until the radiated yield in the simulation reproduces the yield in the data. His most important results are summarized in Section 6.1 and in [48]. In this thesis, the extracted $^3\mathrm{He(e,e'p)d}$ experimental spectral function is used in the simulation of this channel, so the extraction of the two-body radiative tail underneath the continuum was possible.

The six fold differential $^3\mathrm{He(e,e'p)pn}$ cross section, subject of this thesis, is extracted by fitting the radiated simulation to the data, bin by bin on P$_{miss}$ and E$_{miss}$ then correcting for the radiative effects.

From the real data, we measure the number of events $N(E^i_m, P^j_m)$ falling into a missing energy and momentum bin $B_{ij}(E^i_m, P^j_m)$. The bin spans a range of missing energy and missing momentum given by:

$$E_{miss} = E_m^i \pm \frac{\Delta E_m}{2},\ P_{miss} = P_m^j \pm \frac{\Delta P_m}{2}. \tag{5.1}$$

The experimental cross section is obtained from normalizing the PWIA cross section in the simulation by:

$$\frac{d^6\sigma^{Exp}}{dE_f dE_p d\Omega_e d\Omega_p}(P_m, E_m) = KS(i,j)\prod_{k=1}^{k=n} w^k(i,j), \tag{5.2}$$

where w^k is the adjusted weight during the iteration k:

$$w^k = \frac{N(E_m^i, P_m^j)}{N^k(E_m^i, P_m^j)} \tag{5.3}$$

where $N^k(E_m^i, P_m^j)$ is the number of events falling into the same missing energy and momentum bin (E_m^i, P_m^j) in the radiated simulation, corresponding to the iteration k.

In fact, one pass is not enough for the normalization, because of the radiation effects which tend to mislead the reading of missing energies and missing missing momenta; see section 5.3.

The normalization is stopped when all the weighting factors are close enough to one, (1 ±0.001). During the analysis, three or four iterations were enough to reproduce the correct number of counts, depending on the statistics and on the kinematics.

With the new spectral function, we run the simulation at the vertex and extract the vertex cross section. This vertex cross section is then compared to the available theoretical models.

5.2 Details of the normalization

The steps of the normalization are summarized below:

1. Construct an ESPACE missing energy spectrum, within the spectrometer acceptance cut (R-function $>$ 0.002) and clean it from all possible contamination using the software cut described in Sec. 4.5.

2. A PWIA momentum distribution, using Salme's model [49] for the two-body break up and for the continuum spectral functions along with σ_{cc1} electron-proton off-shell cross section, is used to generate the number of events passing through the cuts as a function of missing momentum and missing energy for a considered bin $B_{ij}(\omega, q, E_m^i, P_m^j)$ for all the kinematics. Salme's spectral function does not go further than $\mathrm{E_m} = 127\,\mathrm{MeV}$, so a linear extrapolation was adopted to consider the missing region up to 200 MeV; see section 5.2.1.

   The generated number of counts passing through the spectrometer acceptance is normalized to the measured cross-sections within the measured regions; the same binning is used for both data and simulation. The simulation is run with radiations on, in order to compare the resulting number of counts to the real counts from the data. All the cuts applied in the data analysis are applied in the simulation, except for the coincidence time of flight cut and particle identification cuts, and VDC tracking cuts.

3. Add the resulting $^3\mathrm{He(e, e'p)d}$ and $^3\mathrm{He(e, e'p)pn}$ missing energy spectra to reproduce the total missing energy spectrum which has to be normalized to the experimental spectra given by ESPACE. Figures 5.1 and 5.2 represent three dimensional plots of the number of counts versus missing momentum and missing energy for the simulation after the normalization and the data respectively. The contributions of the two-body and the three body were simulated separately and the normalized yields are represented in Figs. 5.3 and 5.4.

5.2.1 Extrapolation and interpolation of Salme's PWIA spectral function

Salme's PWIA is incorporated in the simulation code MCEEP. It is a function of missing momentum $\mathrm{P_{miss}}$ for the two-body reaction channel and of $\mathrm{P_{miss}}$ and missing energy $\mathrm{E_{miss}}$ for the continuum channel.

Salme's spectral function is a one dimensional vector with 81 values on $\mathrm{P_{miss}}$ for the two-body case, and it is two dimensional 81 $\times$ 139 on $\mathrm{P_{miss}}$ and $\mathrm{E_{miss}}$, respectively. The spectral function spans missing momenta up to 1500 MeV/c but does not go further than 127 MeV on missing energies. The E89044 continuum data goes up to 1200 MeV/c on $\mathrm{P_{miss}}$ and up to 180 to 200 MeV on $\mathrm{E_{miss}}$, depending on the kinematics. Also, the binning on missing momentum in the original Salme's spectral function in the simulation was 20 MeV/c, when the binning on the data for kinematics of rich statistics was 10 MeV/c (but we opened this window for kinematics of low statistics). Therefore, not only the original Salme's $\mathrm{^3He(e,e'p)pn}$ spectral function was extrapolated up to 190 MeV on missing energies, but it was also interpolated with a binning of 10 MeV/c on missing momenta. The resulting spectral function is a 162 $\times$ 200 two dimensional vector on $\mathrm{P_{miss}}$ and $\mathrm{E_{miss}}$, respectively. The fit of the simulation to the data was then possible by normalizing the number of counts in each bin in the simulation to same bin in the data.

The extrapolation beyond $\mathrm{E_{miss}} = 127\,\mathrm{MeV}$ was a linear extrapolation. For Σ_1 and Σ_3 kinematics, a constant value of the spectral function was taken for missing energies $\mathrm{E_{miss}} > 127\,\mathrm{MeV}$ so that $\mathrm{S(P_{miss},\, E_{miss}) = S(P_{miss},\, 127\,MeV)}$. The missing energy spectrum obtained by this new starting "PWIA" spectral function for kinematics 10, for example, is shown in Fig. 5.5.

In the Σ_2 perpendicular kinematics, the pion production region appears for missing energies beyond $\mathrm{E_{miss}} = 140\,\mathrm{MeV}$. Therefore, and in order to accelerate the procedure of the normalization, a study of the shape of the extrapolation function was done. The final choice was a linear extrapolation with a positive slope. The missing energy spectrum obtained by this new starting "PWIA" spectral function for kinematics 8, for example, is represented in Fig. 5.6.

A Fortran based program for the interpolation and the extrapolation of the two dimensional spectral function $\mathrm{S(P_{miss},\, E_{miss})}$ in the continuum region is given in Appendix B.

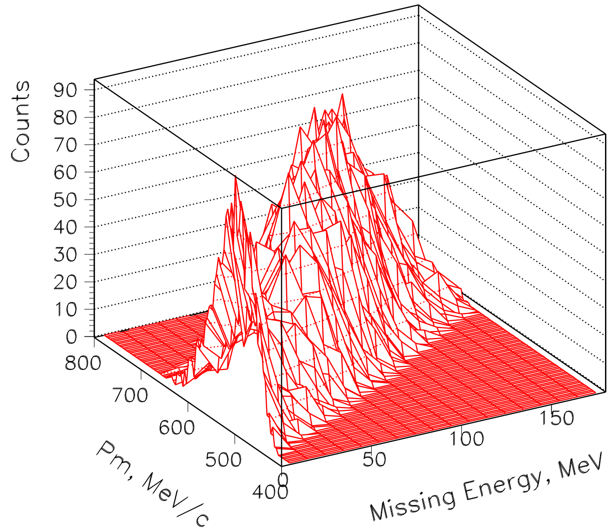

Figure 5.1: A three dimensional plot representing number of counts versus missing momentum and missing energy for kin13. This plot is obtained from the real data.

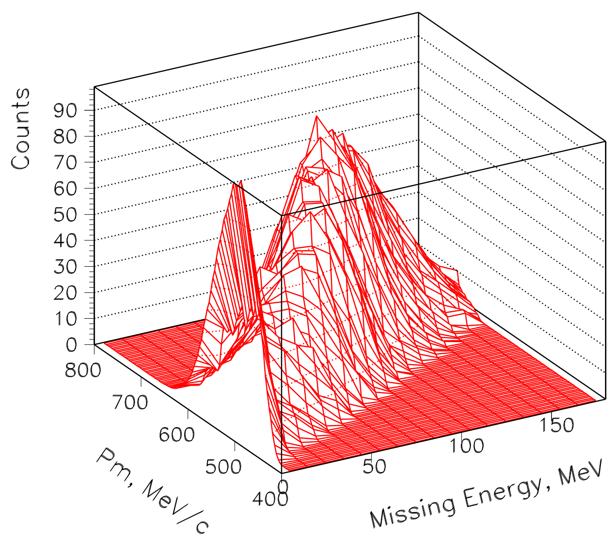

Figure 5.2: A three dimensional plot representing number of count versus missing momentum and missing energy for kin13. This plot is obtained from the simulation by adding the 2bbu and the 3bbu contributions.

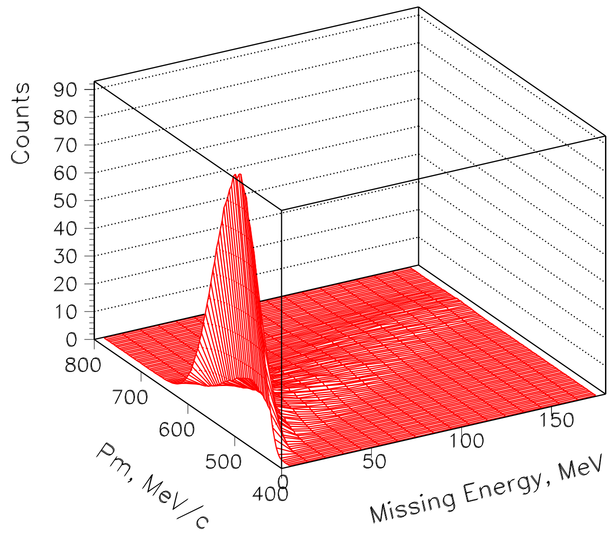

Figure 5.3: A three dimensional plot representing number of counts versus missing momentum and missing energy for kin13. This plot is the normalized number of counts of the simulation to the number of count of the data for the 2bbu channel.

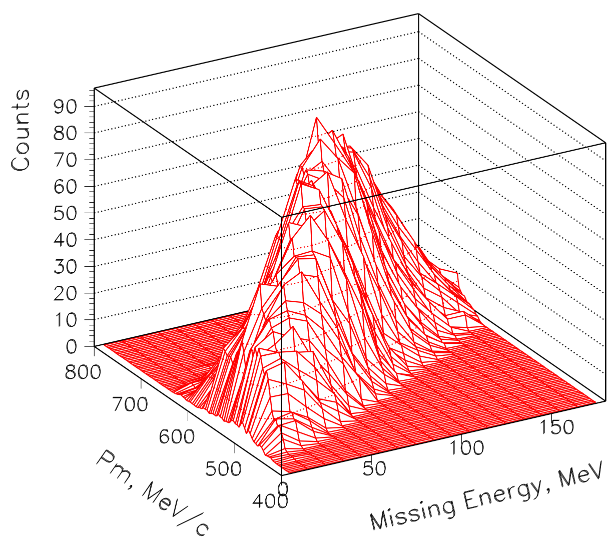

Figure 5.4: A three dimensional plot representing number of count versus missing momentum and missing energy for kin13. This plot is the normalized number of counts of the simulation to the number of count of the data for the continuum channel.

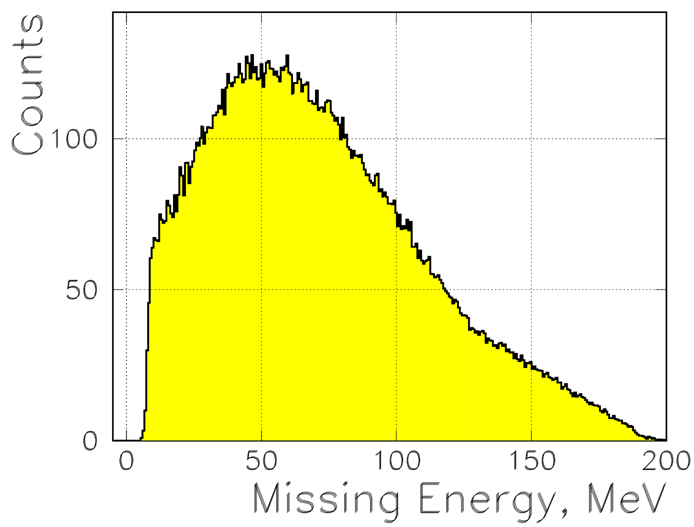

Figure 5.5: PWIA missing energy spectrum for kinematics 10. A constant extrapolation of the spectral function was adapted for $\mathrm{E_{miss}} > 127\ \mathrm{MeV}$, leading to the predicted shape shown for the counts.

.

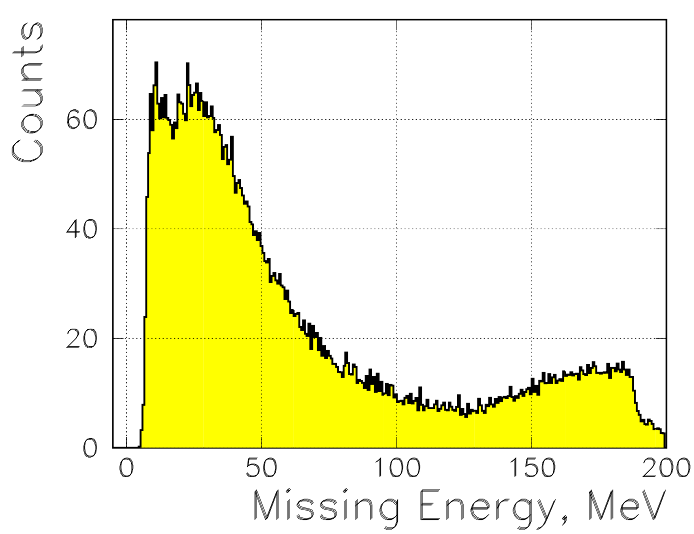

Figure 5.6: PWIA missing energy spectrum for kinematics 8. A linear extrapolation of the spectral function with a positive slope was adapted for $\mathrm{E_{miss}} > 127\ \mathrm{MeV}$, leading to the predicted shape shown for the counts.

.

5.3 Radiative corrections

Unfortunately, the $(\mathrm{e},\mathrm{e}'\mathrm{p})$ reaction does not only proceed through a simple one photon exchange diagram shown in Fig. 1.3. In reality, the incoming and the outgoing charged particles radiate real and virtual photons. This changes not only the cross section for the reaction, but also the apparent energy and momentum transfer [70]. Further, while these radiative corrections are an integral part of (e,e'p) reaction, theoretical work simply does not include these effects. Therefore, it is the responsibility of the experimentalist to correct the measured cross sections for radiative losses in order to perform a meaningful comparison between the experiment and the theory.

The radiative corrections for the present experiment were included in the simulation program MCEEP. Radiative processes may be grouped into two categories:

- Internal radiation: The electron radiates real and virtual photons in the presence of the Coulomb field of the target nucleus involved in the $(e,e'p)$ reaction. See Figs. 5.7 and 5.8.

- External radiation: The electron radiates real and virtual photons in the presence of the Coulomb fields of nuclei other than the target nucleus.

Figure 5.9 represents $^3\mathrm{He}(\mathrm{e},\mathrm{e}'\mathrm{p})\mathrm{pn}$ missing energy spectra obtained in MCEEP at kinematics 10. In the full line histogram all the radiation effect cited above are taken into account. The dash-dotted histogram is corrected for radiative effects. The radiation factor can vary from one kinematics to an other, and it can vary within the same kinematics for different bins on E_{miss}; see lower Figure 5.10.

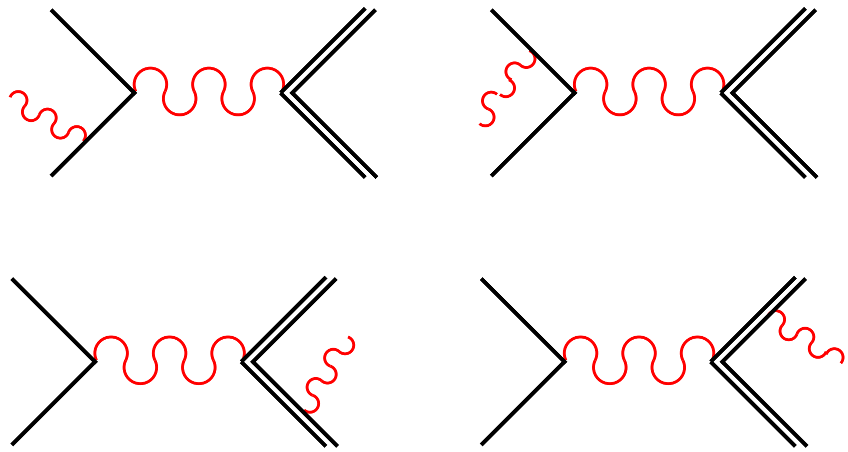

Figure 5.7: Real photon radiation.

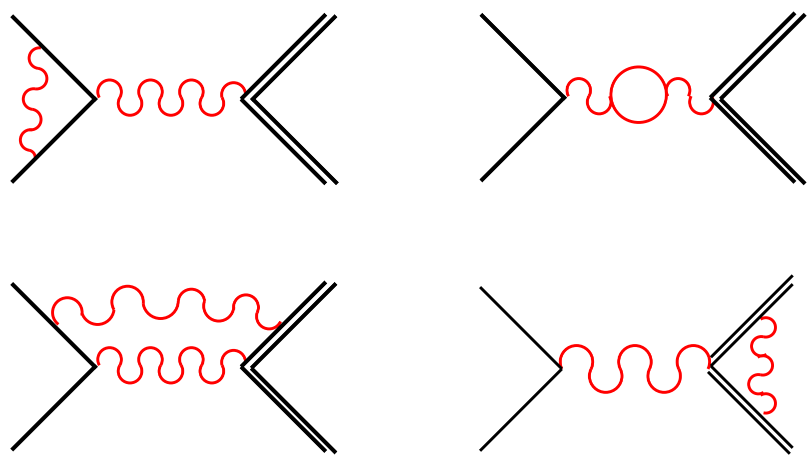

Figure 5.8: Virtual photon radiation.

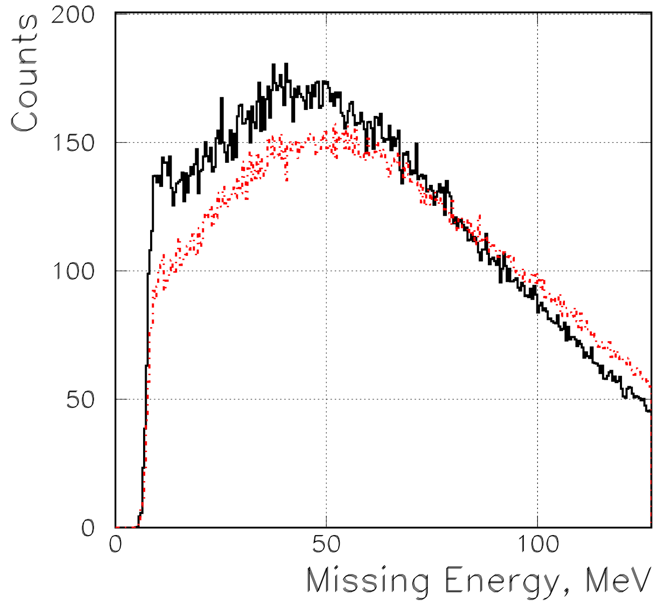

Figure 5.9: Missing energy spectrum for the PWIA. The continuous histogram is affected by radiations. The dash-dotted histogram is corrected for radiative effects.

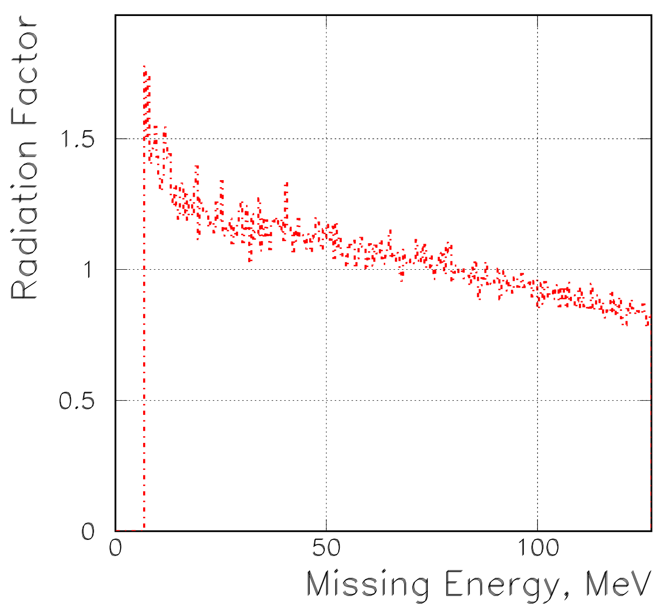

Figure 5.10: Ratio of the radiated to the unradiated missing energy spectra obtained at kinematics 10.

5.3.1 Internal radiations

The processes involving the radiation of a single bremsstrahlung photon are represented in the four Feynman diagrams in Fig. 5.7.

The radiation of soft photons (real photons with energies below the photon cutoff energy) and virtual photons contribute in the "Schwinger" correction to the cross section. The emission of hard photons (real photons with energy above the cutoff energy) leads to the radiative tail.

Schwinger correction

The Schwinger correction [50, 51] is given in terms of soft photon and virtual photon corrections, δ_r and δ_v respectively, as:

$$C_{Schwin} = e^{-\delta_r}(1 - \delta_v) \tag{5.4}$$

Radiative tail

The radiation of a hard photon can affect the kinematics by changing the yield distribution in the missing energies. The peaking approximation is used; in this approximation the photon is assumed to be radiated either along the incident or the scattered electron directions. The radiative tail of the $^3\mathrm{He}(\mathrm{e},\mathrm{e}'\mathrm{p})\mathrm{d}$ reaction is simulated with MCEEP using the Borie and Drechsel [53] prescription in peaking approximation.

Multi-photon correction

The full multi-photon contribution to the radiative tail in MCEEP is given by:

$$f_{mp} = (1 - \delta_v)\frac{(1 - e^{-\delta_r})}{\delta_r} \tag{5.5}$$

This factor is applied to the tail cross section for each event. Vertex kinematics are used in the calculation of δ_r and δ_v.

5.3.2 External radiation

MCEEP calculates the average energy losses by collisions in the target for electrons and protons with the Bethe-Bloch formula, [45], with additional corrections for density and shell effects [45, 46, 52]. Energy loss straggling is approximated by either Landau, Vavilov, or Gaussian distributions, depending on the ratio between mean energy loss and maximum energy loss in a single collision [39]. In a final stage of event simulation, the mean energy losses of electrons and protons are subtracted to allow comparison with data.

5.3.3 Procedure of the radiative corrections.

Comparison of the number of events coming from the experimental data (experimental data are obviously affected by the radiations and the goal here is to correct for them), for a bin B_{ij}(ω, Q^2, E^i_m, P^j_m) and the number of events coming from the simulation with no radiation gives a factor $R(i, j)$ correcting for the classical internal and external bremsstrahlung radiation to this bin.

$$N_0(E^i_m, P^j_m) = N_{exp}(E^i_m, P^j_m)\ R(i, j) \tag{5.6}$$

This is not enough to deal with the radiative corrections, the second step is to subtract the tails from this bin, ie, the contribution of the radiative tails of the higher energy neighboring bins to this bin. This is because missing energy and missing momenta are modified with the contribution of the energy and the momentum of the radiated photon respectively.

The amount that should be subtracted from the i^{th} bin due to the radiative tail coming from the closest previous bin ; ie $(i-1)^{th}$ bin, is:

$$\Delta N^{i,j}_{i-1} = N_0(E^i_m, P^j_m)\ \left(\frac{1}{R(i, j)} - \frac{1}{R(i-1, j)}\right) \tag{5.7}$$

and the amount which should be subtracted from the $(i-1)^{th}$ bin due to the radiative tail coming from its closest bin the $(i-2)^{th}$; which is the second closest bin to the i^{th}:

$$\Delta N_{i-2}^{i-1,j} = N_0(E_m^{i-1}, P_m^j)\ \left(\frac{1}{R(i-1,j)} - \frac{1}{R(i-2,j)}\right) \tag{5.8}$$

This process is then repeated for the subsequent (E_m^{i-k}, P_m^j) bins for a fixed j.

Hence, the contribution of the k^{th} bin to the i^{th} bin will be:

$$\Delta N_k^{i,j} = N_0(E_m^i, P_m^j)\ \left(\frac{1}{R(i-k,j)} - \frac{1}{R(i-k-1,j)}\right) \tag{5.9}$$

The contribution of all the bins to the i^{th} bin is therefore given by the sum over k from the first bin to the $(i-1)^{th}$ bin.

$$\Delta N^{i,j} = \sum_{k=1}^{k=i-1} N_0(E_m^i, P_m^j)\ \left(\frac{1}{R(i-k,j)} - \frac{1}{R(i-k-1,j)}\right) \tag{5.10}$$

The contribution of the tails becomes smaller if they are coming from bins located far from the i^{th} bin. Hence few terms in the series will be enough for the convergence.

The next step is to increment the missing momentum to P_m^{j+1} and repeat the previous procedure, then go to higher missing energy channels and repeat the same work.

5.3.4 Importance of iterating the normalization method

The method of the radiative tail subtraction, described in the previous section, is implemented in the simulation program MCEEP. In practice, comparing the data to the simulation allows the determination of the normalization factors $R(i, j)$. One pass is not enough for the simulation to reproduce the data, a few iterations are necessary.

Figure 5.11 shows the steps followed in the normalization of kin10. First the height and width of the two-body were normalized bin by bin on $\mathrm{P_{miss}}$. Then using the normalized 2bbu spectral function, along with the extrapolated PWIA spectral function for the continuum channel, the continuum simulation was normalized to the data bin by bin on $\mathrm{P_{miss}}$ and $\mathrm{E_{miss}}$. The normalization was repeated many times until we got the complete agreement between the simulation and the data. In each pass normalization weights are extracted for each bin on $\mathrm{P_{miss}}$ and $\mathrm{E_{miss}}$. The normalization is complete when the normalization factors stabilize at the value of 1. For a given bin on $\mathrm{P_{miss}}$, suppose the model spectral function (unradiated) is a function of only two non-zero values: $\mathrm{S_u(1)} = 20,\ \mathrm{S_u(2)} = 10$. This example was proposed by P. Ulmer [54], to investigate the validity of the proposed method [1]. Take a simple formula for the radiation effect: $\mathrm{S_r(i)} = 0.8\,\mathrm{S_u(i)} + 0.2\,\mathrm{S_u(i-1)}$. where $\mathrm{S_r(i)}$ is the radiated spectral function for bin i and $\mathrm{S_u(i)}$ is the unradiated one. Then the radiated model spectral function becomes: $\mathrm{S_r(1)} = 16,\ \mathrm{S_r(2)} = 12, \mathrm{S_r(3)} = 2$. Now suppose the data gives: $\mathrm{S_d(1)} = 32,\ \mathrm{S_d(2)} = 36,\ \mathrm{S_d(3)} = 8$.

[1] It is the first time ever that this method of normalization of the continuum data is used. This method is very efficient and can be with a big help for future analysis of other experiments.

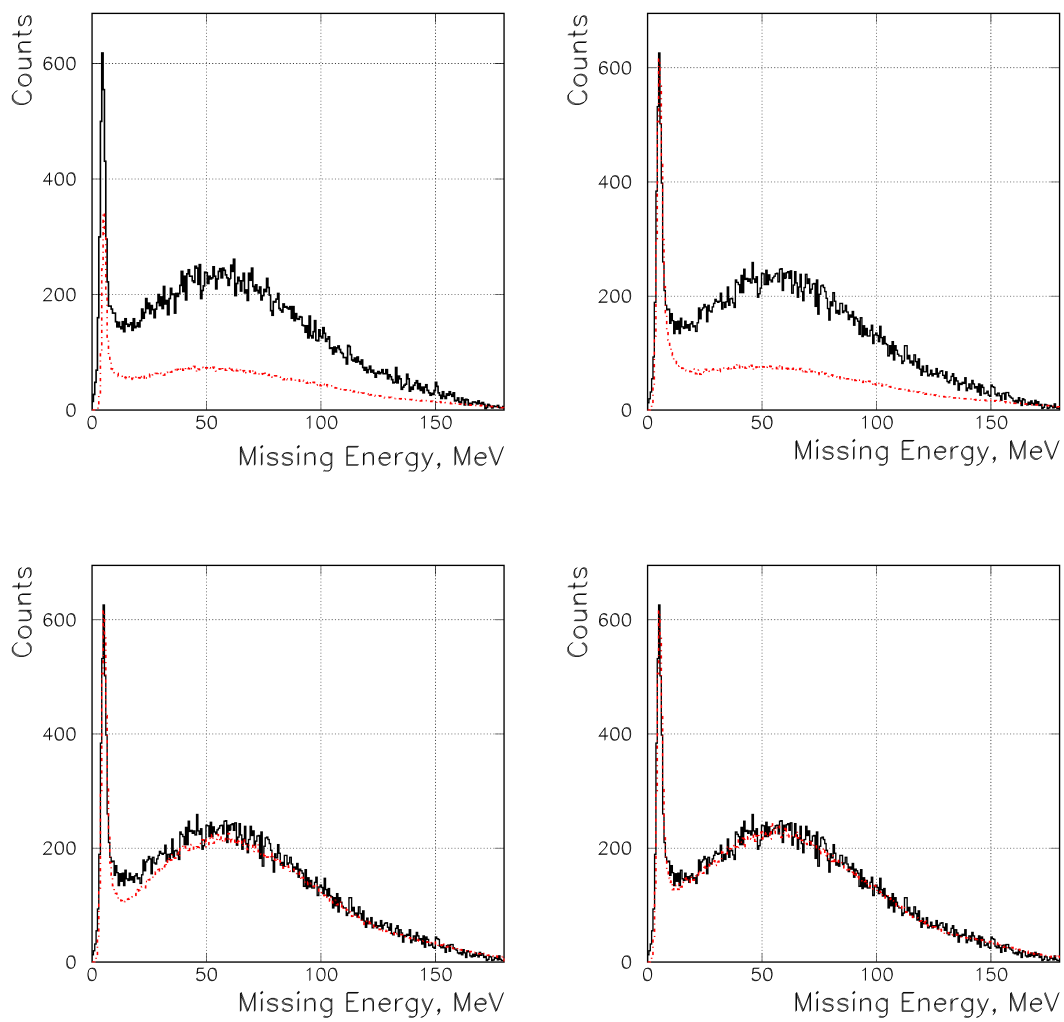

Figure 5.11: Steps of the normalization at kinematics 10. $\mathrm{P_{miss}} = 450\,\mathrm{MeV/c}$ the beam energy is 4.8068 GeV. The dashed dotted red histogram is the missing energy spectrum in the PWIA with Salme's spectral function. The solid black line is the data.

Then the scaling factors for the three bins are: 2, 3, 4. This gives a new model spectral function: $\mathrm{S_{u1}}(1) = 40$, $\mathrm{S_{u1}}(2) = 30$ and all others are zero. If this is the correct spectral function, then radiating it should yield the data values. By applying the same radiation prescription as before: $\mathrm{S_{r1}}(1) = 32, \mathrm{S_{r1}}(2) = 32$, $\mathrm{S_{r1}}(3) = 6$. These are "NOT" the values given by the data. So, one pass is not enough for the normalization.

Second iteration:

The new scaling factors are: $1,\ \frac{9}{8}$ and $\frac{4}{3}$.

The new model spectral function is: $\mathrm{S}_{u2}(1) = \mathrm{S}_{u1}(1) = 40$,

$\mathrm{S}_{u2}(2) = \frac{9}{8}\ \mathrm{S}_{u1}(2) = \frac{135}{4}$ and

$\mathrm{S}_{u2}(3) = 0$.

The radiated spectral function is:

$\mathrm{S}_{r2}(1) = 0.8\,\mathrm{S}_{u2}(1) = 32$,

$\mathrm{S}_{r2}(2) = 0.8\,\mathrm{S}_{u2}(2) + 0.2\,\mathrm{S}_{u2}(1) = 35$ and

$\mathrm{S}_{r2}(3) = 0.2\,\mathrm{S}_{u2}(2) = \frac{27}{4} = 6.75$.

Third iteration

The new scaling factors are: $1,\ \frac{36}{35}$ and $\frac{32}{27}$.

Giving the new model spectral function:

$\mathrm{S}_{u3}(1) = \mathrm{S}_{u2}(1) \times 1 = 40$,

$\mathrm{S}_{u3}(2) = \mathrm{S}_{u2}(2) \times \frac{36}{35} = \frac{1215}{35} = 34.71$ and

$\mathrm{S}_{u3}(2) = 0$.

The radiated spectral function is:

$\mathrm{S}_{r3}(1) = 0.8\,\mathrm{S}_{u3}(1) = 32$,

$\mathrm{S}_{r3}(2) = 0.8\,\mathrm{S}_{u3}(2) + 0.2\,\mathrm{S}_{u3}(1) = 35.77$ and

$\mathrm{S}_{r3}(3) = 0.2\,\mathrm{S}_{u3}(2) = 6.942$.

We can see that the scaling factors become closer and closer to one in each new iteration, this means that the new radiated spectral function converges to the data.

5.4 Missing energy spectra

This section presents spectra of missing energy obtained at some of the kinematic settings analyzed in this thesis.

Each of the figures, from Fig. 5.12 to Fig. 5.4, presents E_{miss} spectra for one spectrometer setting and contains:

1. E_{miss} spectrum reconstructed from the data (solid line).

2. E_{miss} separated spectra obtained in MCEEP simulation of the ^{3}He(e,e′p)d and $^3\mathrm{He(e,e'p)pn}$ reactions (both dash-dotted lines).

3. Sum of the two simulation E_{miss} spectra (dashed line).

The ^{3}He(e,e′p) cross section model used in MCEEP was the factorization of spectral functions fitted to the data with the cc1 prescription for the off-shell electron-nucleon cross section. The following cuts were applied both to data and simulation spectra: R-function acceptance cuts, target length cuts, and the cut on the difference between reaction points reconstructed by the two spectrometers. VDC tracking cuts and the cut on gas Cerenkov ADCs were applied to data spectra. Accidental coincidences were subtracted from data.

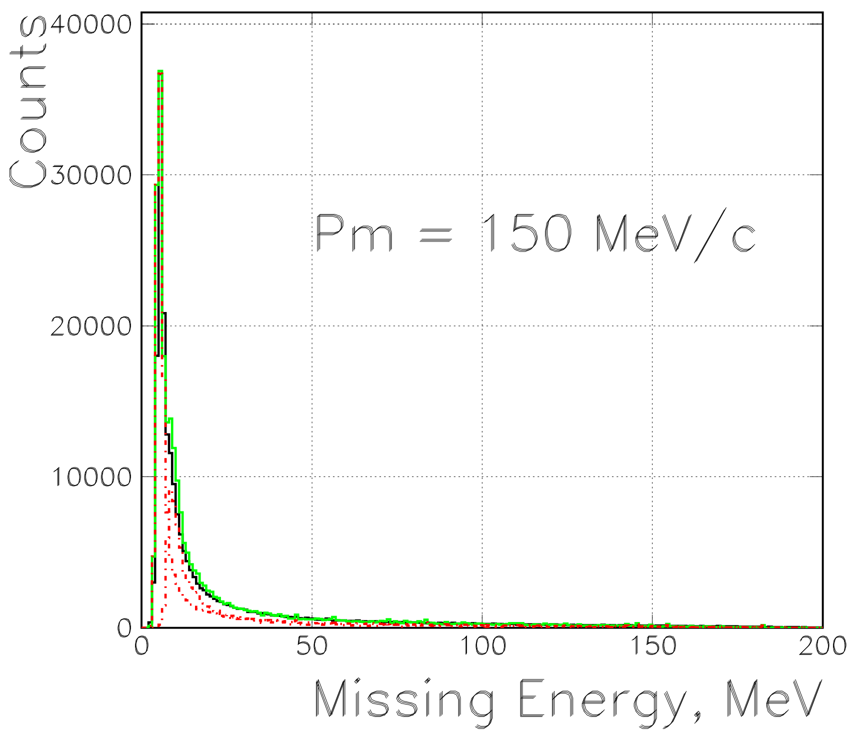

Figure 5.12: ^{3}He(e,e′p) missing energy distribution in kinematics 4. $E_{beam} = 4.8$ GeV, the detected proton is backward of $\vec{q}$. Black solid histogram represents the data, the red dash-dotted line is the simulation of the two-body and the continum seperately and the green dashed line is the sum of the two previous contributions.

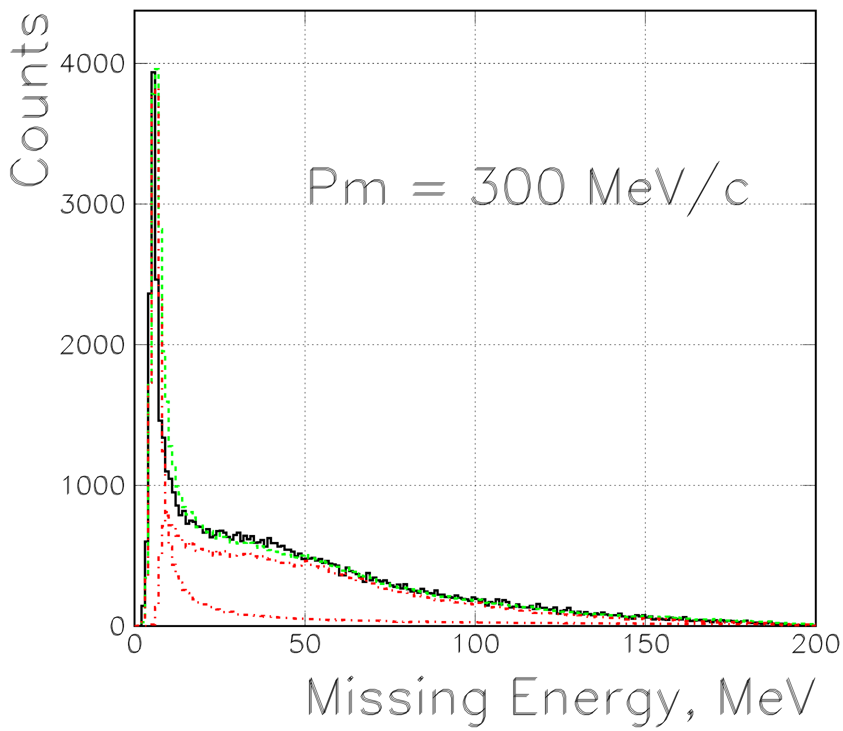

Figure 5.13: ^{3}He(e,e′p) missing energy distribution in kinematics 7. $E_{beam} = 4.8$ GeV. The detected proton is backward of $\vec{q}$. Curves are the same as in Fig. 5.12.

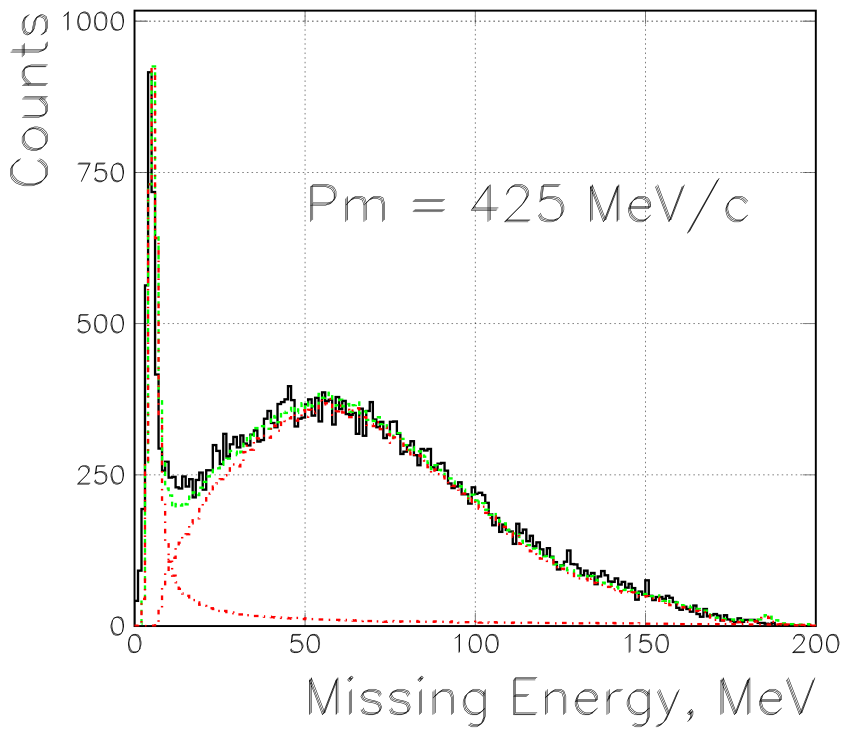

Figure 5.14: ^{3}He(e,e′p) missing energy distribution in kinematics 10. $E_{beam} = 4.8$ GeV. The detected proton is backward of $\vec{q}$. Curves are the same as in Fig. 5.12.

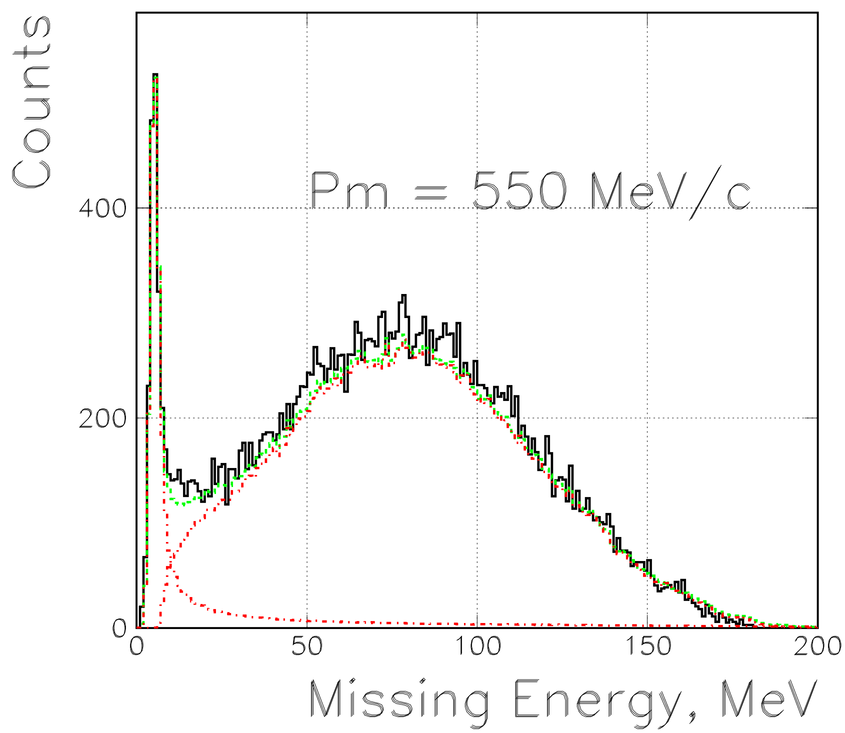

Figure 5.15: ^{3}He(e,e′p) missing energy distribution in kinematics 13. $E_{beam} = 4.8$ GeV. The detected proton is backward of $\vec{q}$. Curves are the same as in Fig. 5.12.

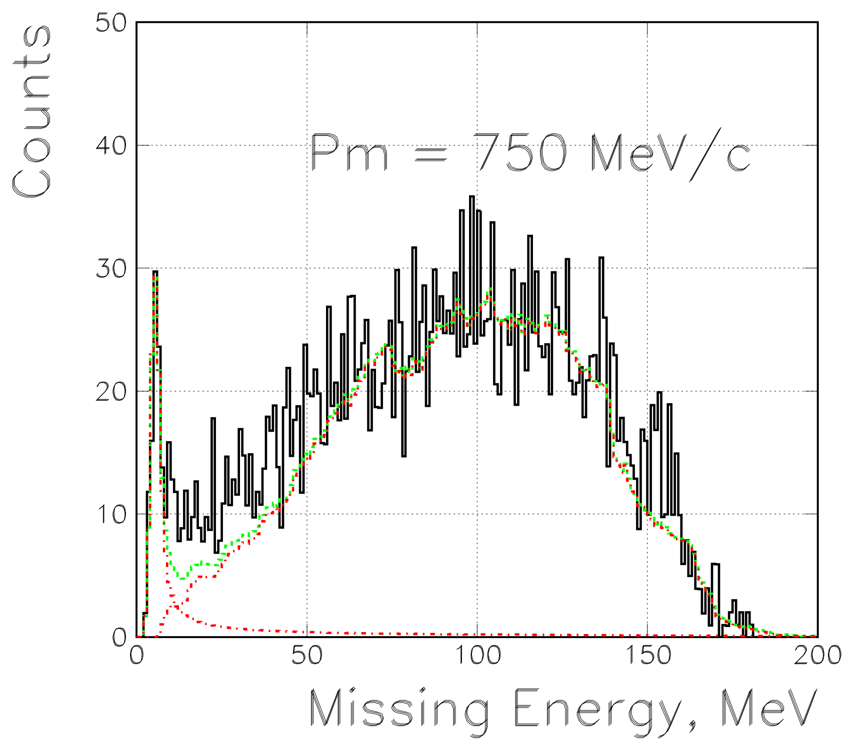

Figure 5.16: ^{3}He(e,e′p) missing energy distribution in kinematics 28. $E_{beam} = 4.8$ GeV. The detected proton is backward of $\vec{q}$. Curves are the same as in Fig. 5.12.

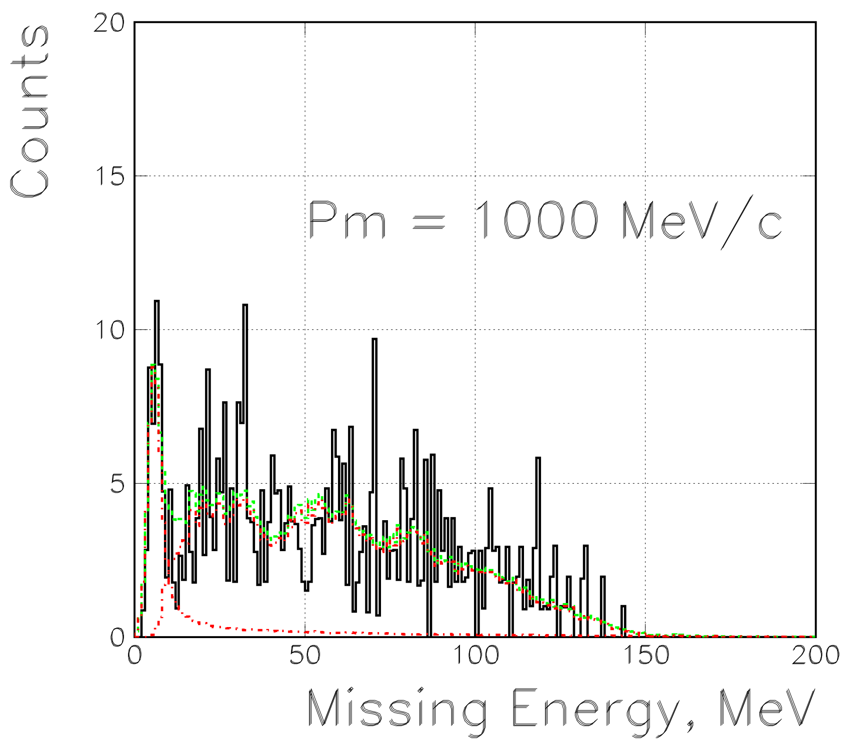

Figure 5.17: ^{3}He(e,e′p) missing energy distribution in kinematics 29. $E_{beam} = 4.8$ GeV, the detected proton is backward of $\vec{q}$. Curves are the same as in Fig. 5.12.

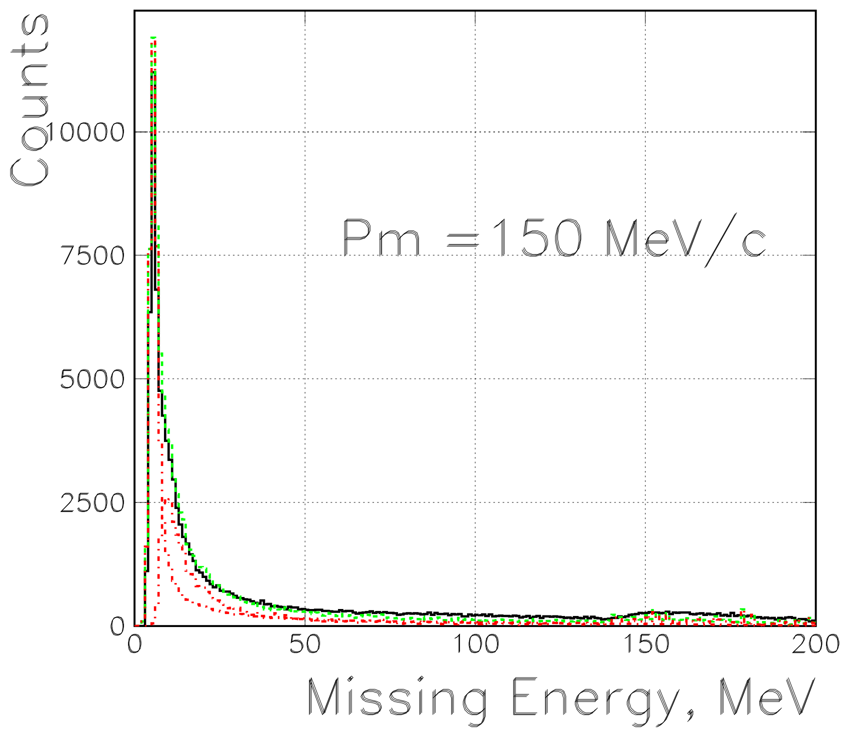

Figure 5.18: ^{3}He(e,e′p) missing energy distribution in kinematics 5. $E_{beam} = 4.8$ GeV, the detected proton is forward of $\vec{q}$. Curves are the same as in Fig. 5.12.

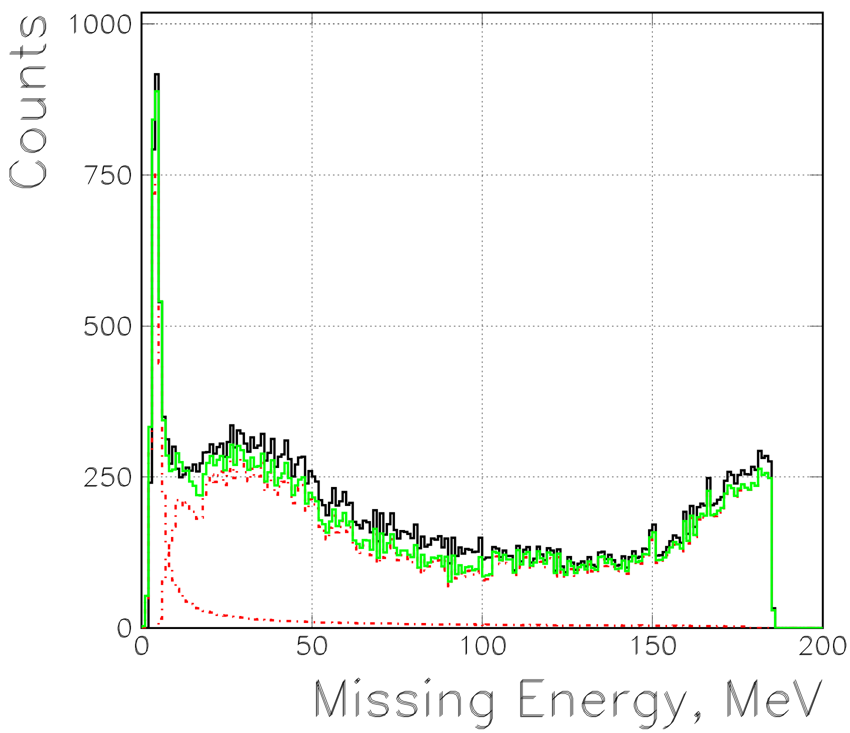

Figure 5.19: ^{3}He(e,e′p) missing energy distribution in kinematics 8. $E_{beam} = 4.8$ GeV. The detected proton is forward of $\vec{q}$. Note the appearence of the pion region around 140 MeV. Curves are the same as in Fig. 5.12.

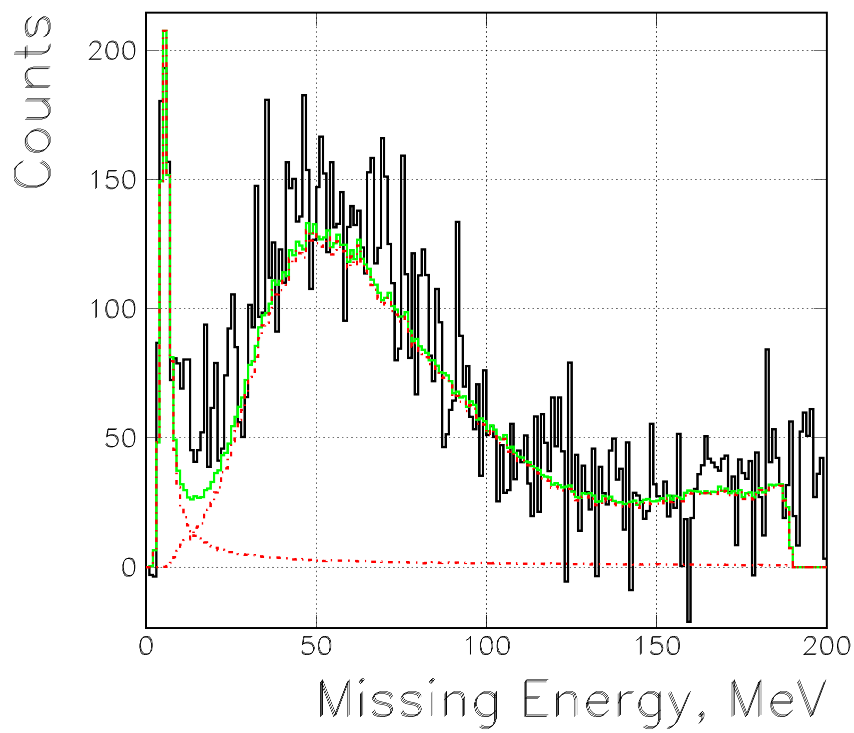

Figure 5.20: ^{3}He(e,e′p) missing energy distribution in kinematics 11. $E_{beam} = 4.8$ GeV. The detected proton is forward of $\vec{q}$. Curves are the same as in Fig. 5.12.

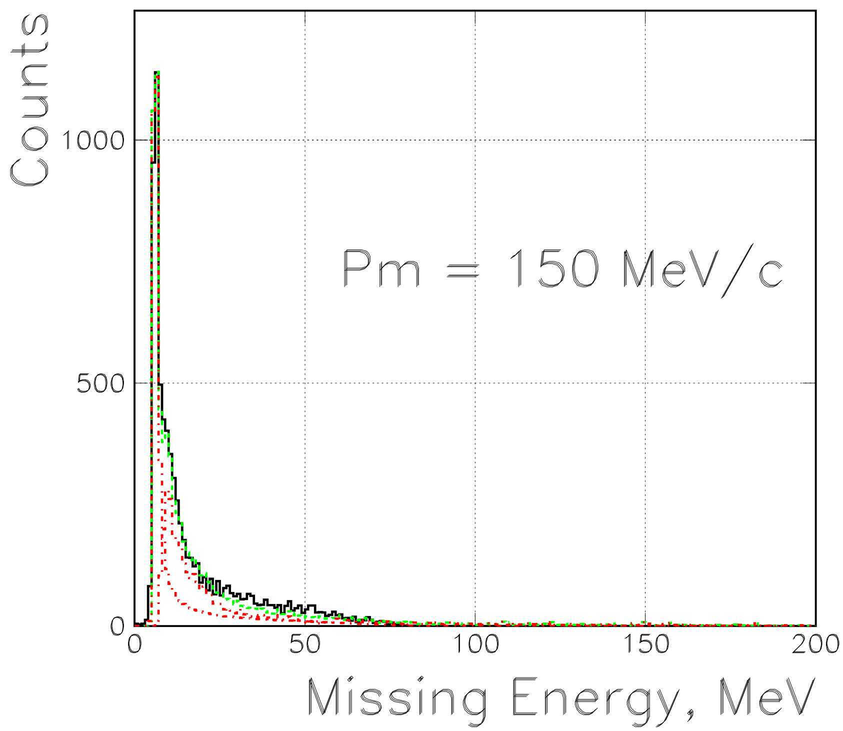

Figure 5.21: ^{3}He(e,e′p) missing energy distribution in kinematics 6. $E_{beam} = 1.2$ GeV. The detected proton is backward of $\vec{q}$. Curves are the same as in Fig. 5.12.

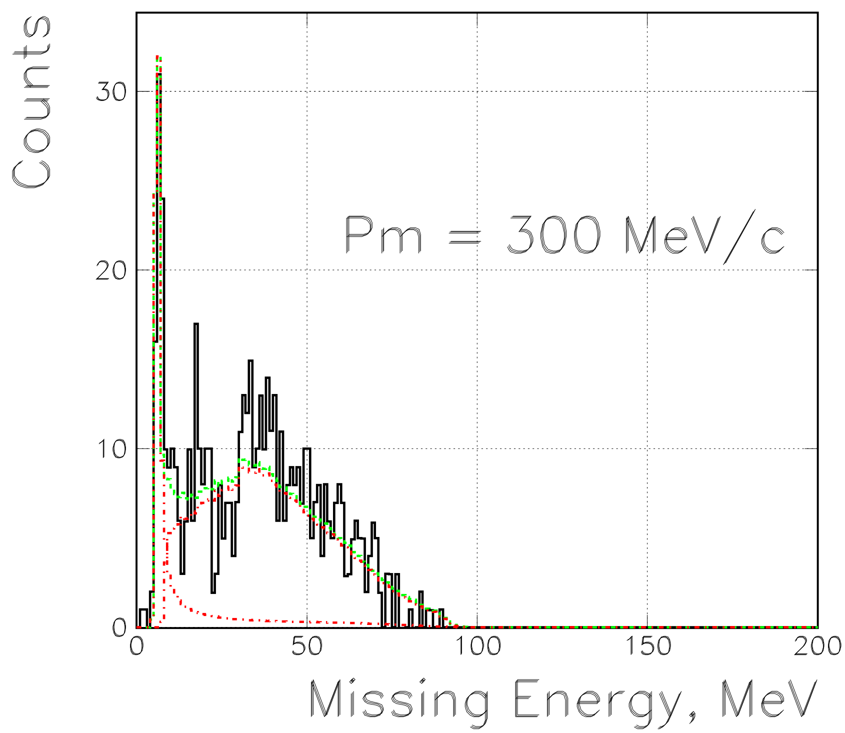

Figure 5.22: ^{3}He(e,e′p) missing energy distribution in kinematics 9. $E_{beam} = 1.2$ GeV. The detected proton is backward of $\vec{q}$. Curves are the same as in Fig. 5.12.

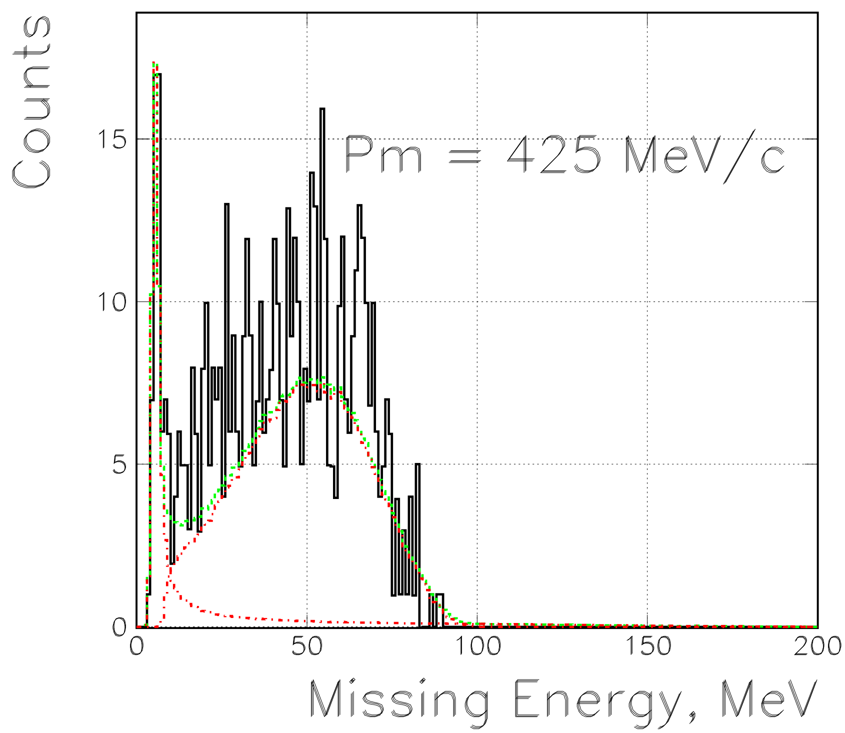

Figure 5.23: ^{3}He(e,e′p) missing energy distribution in kinematics 12. $E_{beam} = 1.2$ GeV. The detected proton is backward of $\vec{q}$. Curves are the same as in Fig. 5.12.

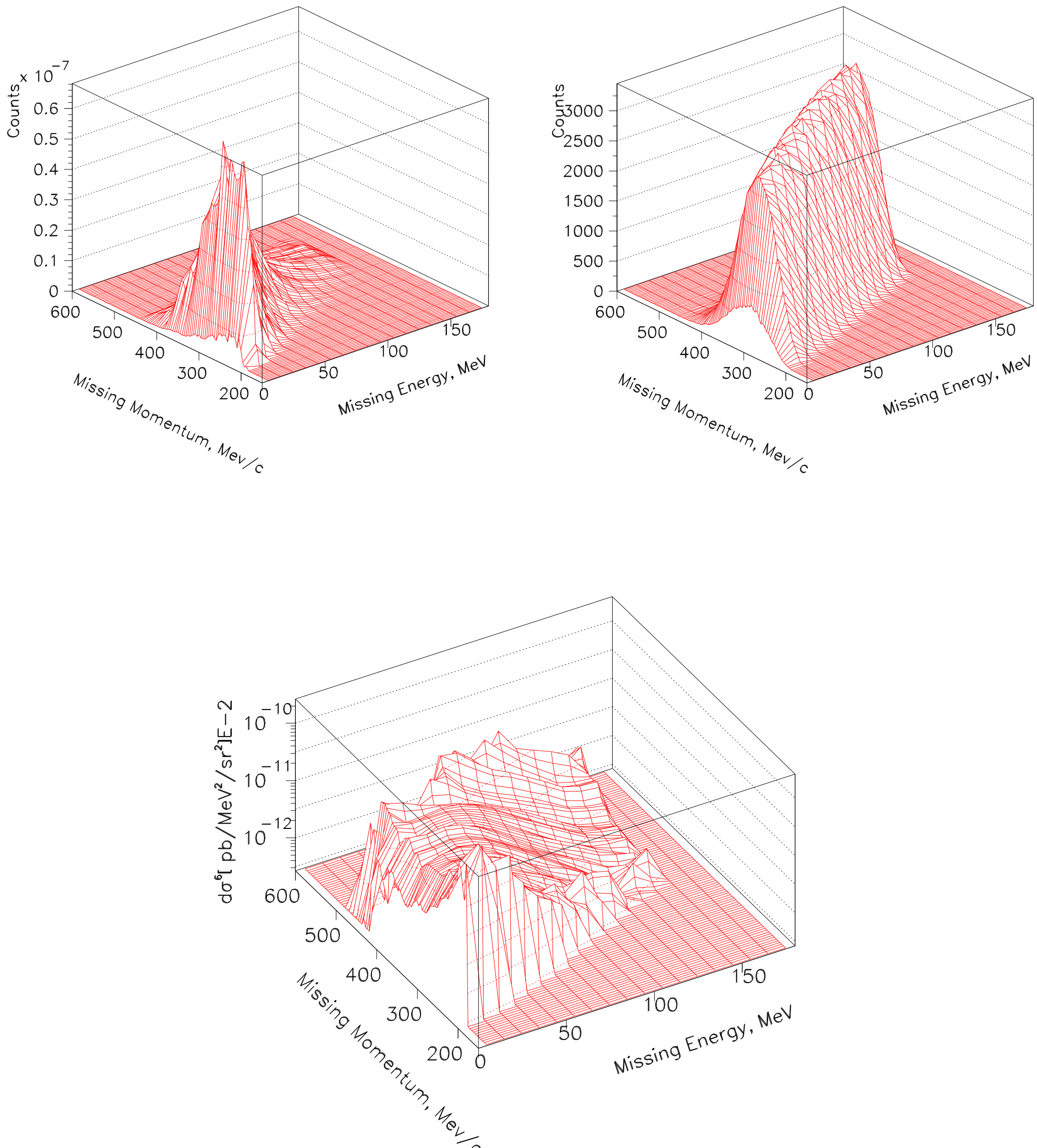

Figure 5.24: Three dimensional diagrams of the the yield (upper left), the phase space (upper right) in arbitrary units and the cross section (center) extracted with MCEEP simulation for kinematics. 7.

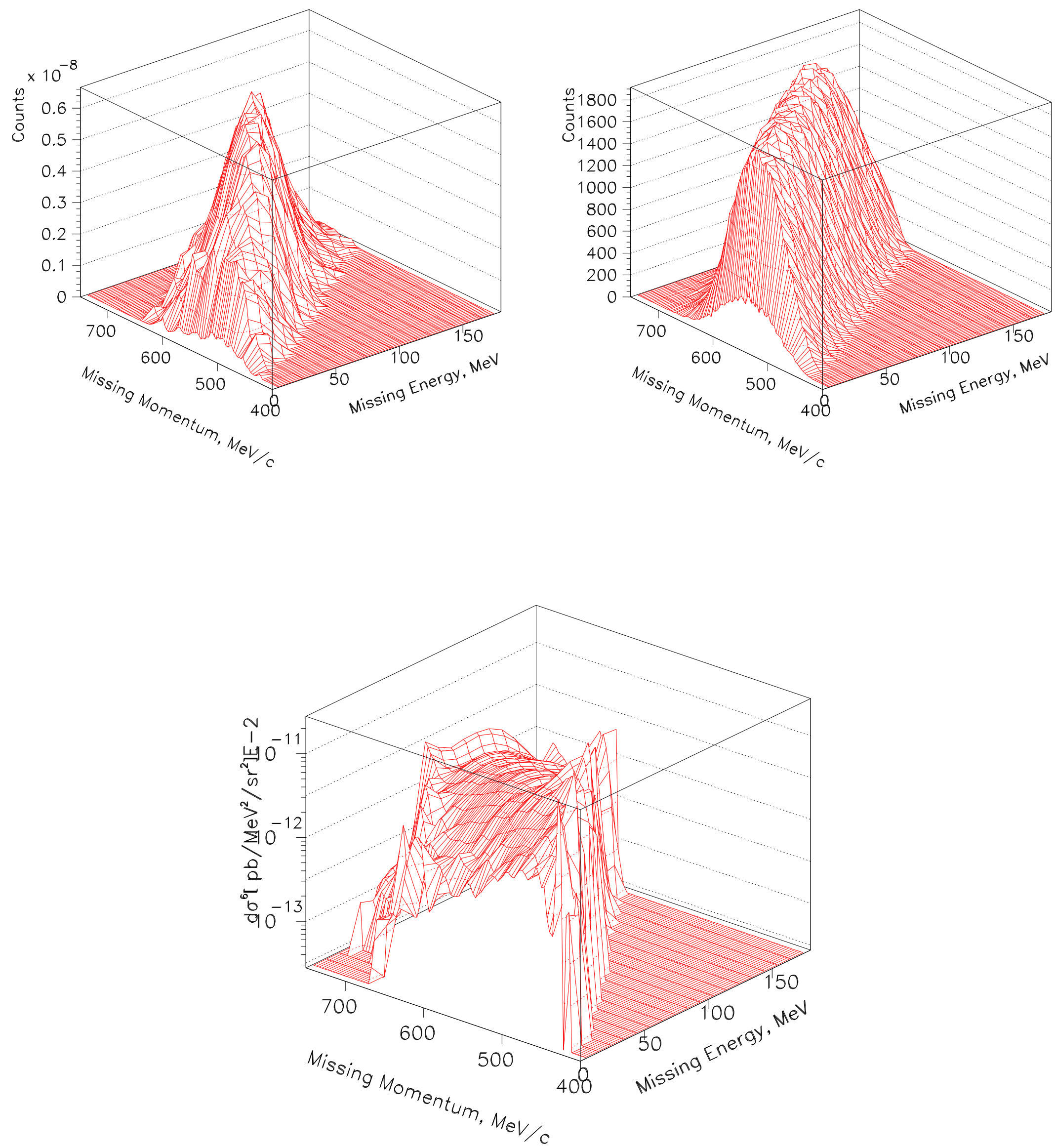

Figure 5.25: Three dimensional diagrams of the the yield (upper left), the phase space (upper right) in arbitrary units and the cross section (center) extracted with MCEEP simulation for kinematics 13.

5.5 Effective momentum density distribution

Another way to compare the results of the experiment to the theoretical predictions is the study of the effective momentum density distribution of the $^{3}\mathrm{He(e,e'p)pn}$ reaction. The momentum density distribution is defined as the integral of the experimental distorted spectral function over missing energy. It can be, therefore, calculated from the cross section as follows:

$$\eta(p_{miss}) = \int_{E_{min}}^{E_{max}} \frac{\frac{d^6\sigma}{dE_f dE_p d\Omega_e d\Omega_p}}{\sigma_{ep}} \; dE_{miss} \tag{5.11}$$

where

$$\frac{d^6\sigma}{dE_f dE_p d\Omega_e d\Omega_p} = K\sigma_{cc1} S(E_{miss}, P_{miss}), \tag{5.12}$$

The lower limit of the integral $\mathrm{E_{min}}$ was taken slightly below the $^{3}\mathrm{He(e,e'p)pn}$ threshold; $\mathrm{E_{min}} = 7$ MeV, and $\mathrm{E_{thr}} = 7.72\ \mathrm{MeV}$, to include the data that, because of resolution effects, appear just below the 3-body breakup threshold. The upper limit of the integral, $\mathrm{E_{max}}$ was taken equal to the pion production threshold, $\mathrm{E}_{max} = 140$ MeV.

The off-shell electron-proton cross section was extracted from the simulation at exactly the same conditions as the experimental cross section. In fact, one has just to run the simulation under the same conditions and the only difference is that for σ_{ep} the input spectral function is taken equal to unity, $\mathrm{S(P_{miss}, E_{miss})} = \mathrm{I}$. σ_{ep} is given by:

$$\sigma_{ep} = \frac{d^6\sigma_{ep}}{dE_f dE_p d\Omega_e d\Omega_p} = K\sigma_{cc1} I \tag{5.13}$$

Figure 5.26 represents the cross section (in arbitrary units) for $\mathrm{P_{miss}} = 470 \pm 5$ MeV/c versus missing energy. This bin was taken from a data set in kinematics 10. The corresponding σ_{ep} cross section is represented in Figure 5.27. By diving these two histograms, Figure 5.28 results. The effective momentum density distribution is obtained by integrating this histogram.

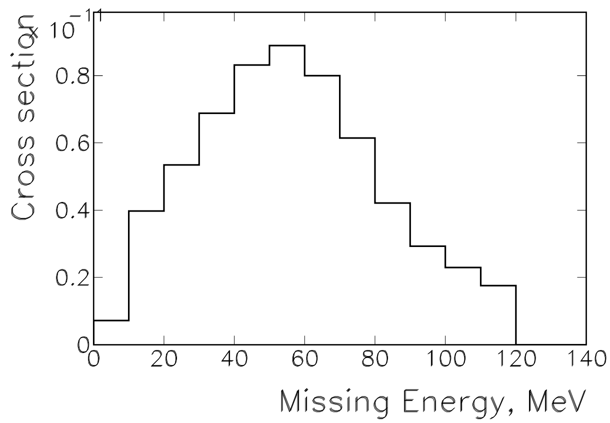

Figure 5.26: Extracted $^3\mathrm{He}(\mathrm{e},\mathrm{e'p})\mathrm{pn}$ cross section, in arbitrary units, for missing momentum bin P$_{miss} = 470 \pm 5$ MeV/c. Bin taken from kinematics 10.

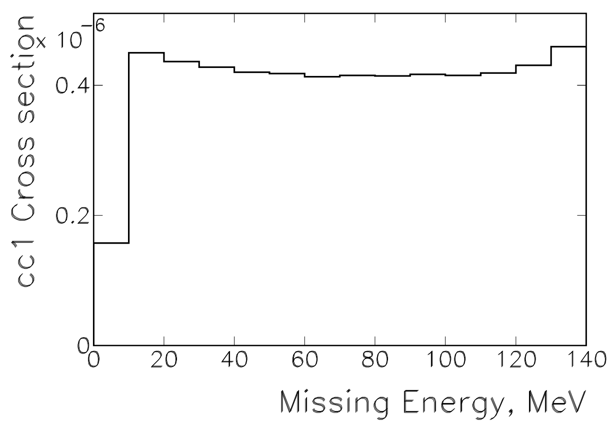

Figure 5.27: The σ_{ep} cross section obtained by the simulation for the same bin on $\mathrm{P_{miss}}$ at kinematics 10.

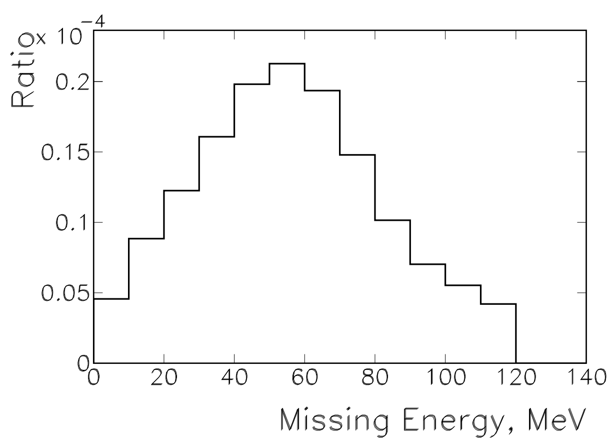

Figure 5.28: Ratio of the two previous histograms. The integral of this new histogram leads to the effective momentum density distribution corresponding to this missing momentum bin.

The momentum density distribution was extracted for Σ_1 and Σ_2 kinematics is are presented in Fig. 5.29 and Fig. 5.30. These results will be discussed and compared to the available theoretical calculations in the next chapter.

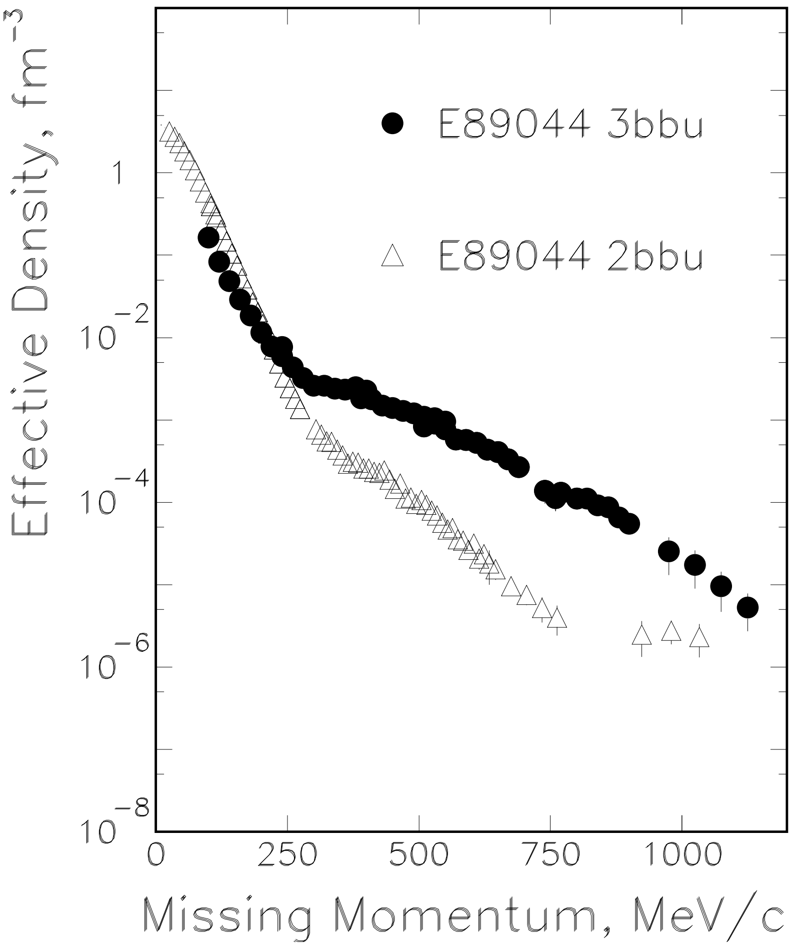

Figure 5.29: Extracted $(\mathrm{e},\mathrm{e}'\mathrm{p})$ effective momentum density distribution for Σ_1 kinematics.

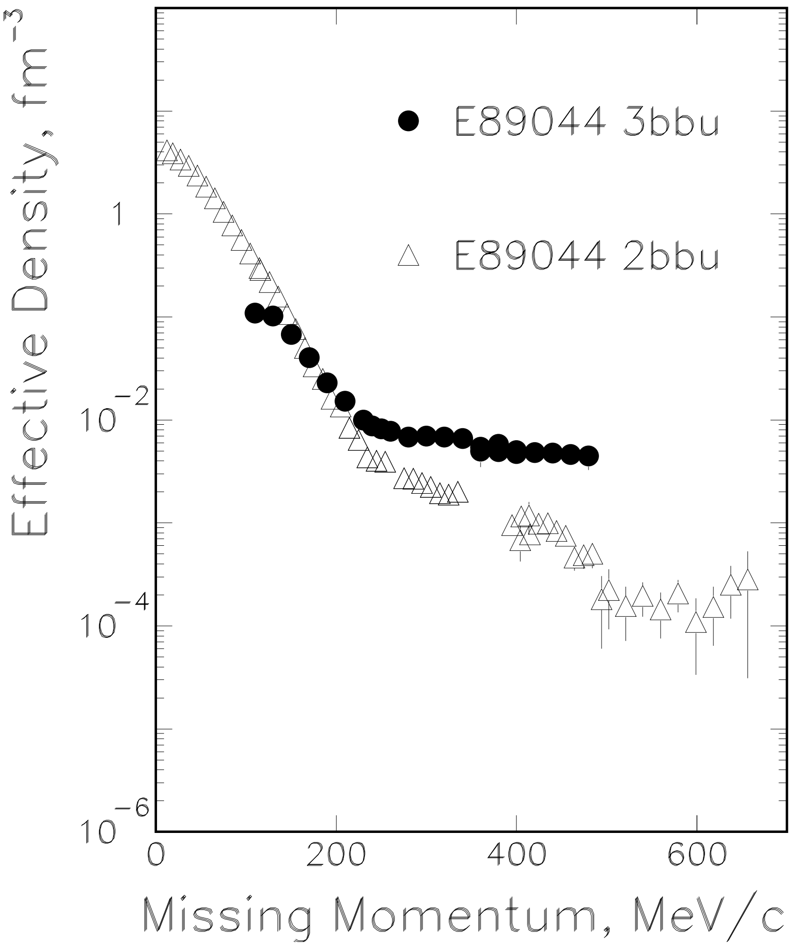

Figure 5.30: Extracted $(\mathrm{e}, \mathrm{e}'\mathrm{p})$ effective momentum density distribution for Σ_2 kinematics.

5.6 Transverse-longitudinal asymmetry A_{TL}

At the beam energy of 4.8 GeV, ^{3}He(e,e′p) data was collected on both sides of $\vec{q}$ up to $P_{miss} \sim 650$ MeV/c. This data was used for the extraction of A_{TL}, defined as

$$A_{TL} = \frac{\sigma_2 - \sigma_1}{\sigma_2 + \sigma_1}, \tag{5.14}$$

where σ_1 and σ_2 are coplanar ^{3}He(e,e′p)d or ^{3}He(e,e′p)pn cross sections measured backward and forward of $\vec{q}$ respectively.

In this section, the extraction of A_{TL} at $E_{beam} = 4.8$ GeV kinematic settings is described.

For each $(\mathrm{P_{miss}}, \mathrm{E_{miss}})$ bin selected both at Σ_1 and Σ_2 kinematic settings, a contour cut imposed in (ω, $|\vec{q}|$) space restricted events to a common Q^2 and ω region for both forward and backward of $\vec{q}$ bin.

The statistical uncertainties on calculating A_{TL} are propagated as

$$\delta A_{TL} = \frac{2 \cdot \sqrt{(\sigma_2 \delta\sigma_1)^2 + (\sigma_1 \delta\sigma_2)^2}}{(\sigma_2 + \sigma_1)^2}, \tag{5.15}$$

where $\delta\sigma_1$ and $\delta\sigma_2$ are standard deviations of σ_1 and σ_2.

In Fig. 5.31, three dimensional histograms of the Σ_1 kinematics 7 and the Σ_2 kinematics 8 cross sections are displayed. From these two histograms, the transverse-longitudinal asymmetry A_{TL} is extracted. The present the results, one can chose to fix P_m and vary E_m or fix E_m and vary P_m. The first presentation was adopted, and the results are compared to the available theoretical calculations. Some results are presented in Sec. 6.4.

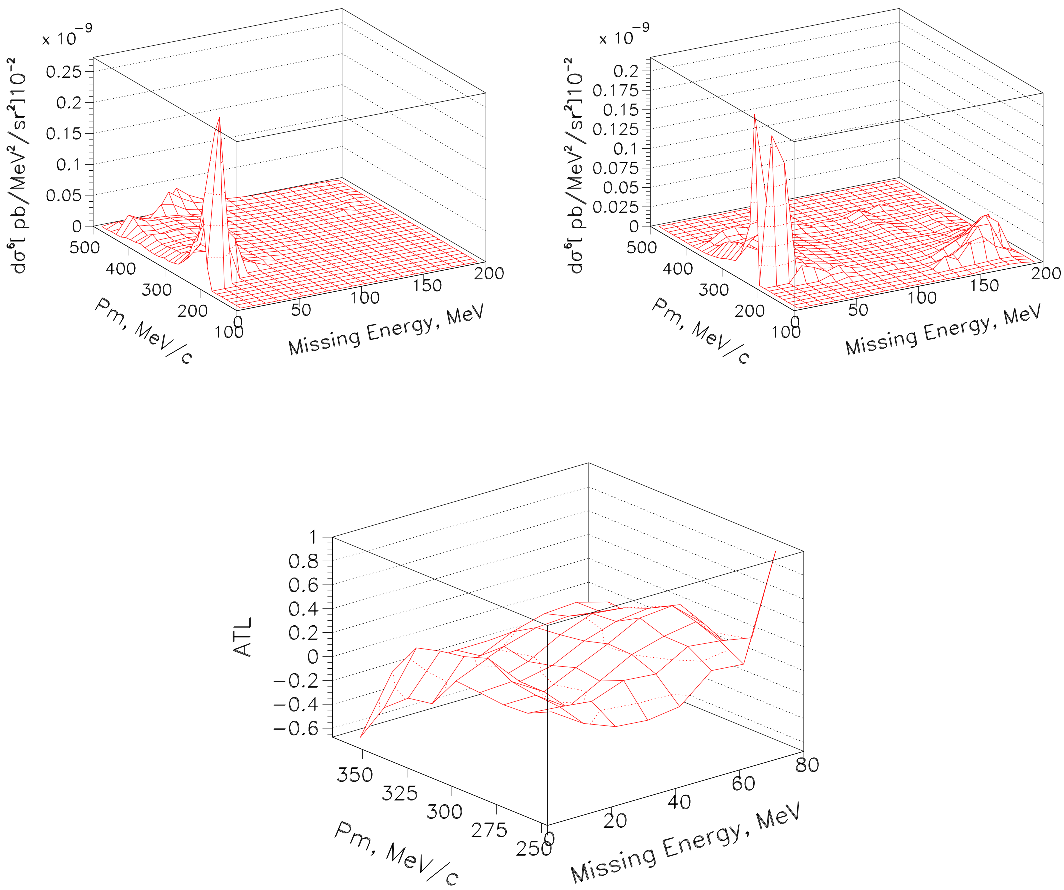

Figure 5.31: Three dimensional histograms of the measured $^3\mathrm{He}(\mathrm{e},\mathrm{e}'\mathrm{p})\mathrm{pn}$ cross section at kinematics 7 and 8, upper left and upper right, respectively. Three dimensional histogram of the $^3\mathrm{He}(\mathrm{e},\mathrm{e}'\mathrm{p})\mathrm{pn}$ transverse-longitudinal asymmetry.

5.7 Systematic uncertainties

A study of systematic uncertainties in the E89044 experiment was performed by M. Rvachev [23] during his analysis of the reaction channel for perpendicular kinematics.

The most important part in the systematic uncertainties comes from the “normalization” uncertainties, which propagate as a multiplicative correction to the extracted cross sections and momentum density distribution. The transverse-longitudinal asymmetry, A_{TL}, is not subject to the overall normalization uncertainty, since this uncertainty cancels in the ratio. Other uncertainties exist as well.

5.7.1 Normalization uncertainties

The normalization uncertainties of the ^{3}He(e,e$'$p) data (i.e. the procedure for determination of the integrated luminosities during the ^{3}He(e,e$'$p)) are from different origins:

1. The uncertainty in the measured density of the ^{3}He gas in the target.
2. The uncertainty in assuming the stability of the ^{3}He density during changes in the beam energy.
3. The uncertainty associated with the luminosity monitoring procedure.

The kinematic uncertainties were determined with the code "systerr" [55], written by K. Fissum and P. Ulmer. This code works in conjunction with MCEEP. Table 5.7.1 summarizes the "kinematic uncertainties" for the elastic ^{3}He(e,e) scattering setting with $E_{beam} = 644$ MeV and $Q^2 = 2.9$ fm^{-2}. The kinematic uncertainties are those due to the sensitivity of the elastic ^{3}He(e,e) cross section to E_i, ϕ_i, θ_i, ϕ_e and θ_e, and uncertainties in these quantities.

Table 5.3 and 5.4 summarizes non-kinematic uncertainties associated with the ^{3}He density measurements. These uncertainties are added in quadrature with the kinematic systematic uncertainty to yield the estimate of 2.9% for the total uncertainty in the measured ^{3}He density.

Table 5.1: Kinematic systematic uncertainty averaged over acceptance in the ^{3}He(e,e) elastic measurements.

Quantity	Sensitivity	Uncertainty	Uncertainty
E_i	1.1%/(10^{-3} rel.)	$2 \cdot 10^{-4}$	0.22%
ϕ_i	1.7 %/mr	0.1 mr	0.17%
θ_i	0.006%/mr	0.1 mr	0%
ϕ_e	1.7 %/mr	0.3 mr	0.51%
θ_e	0.005 %/mr	2 mr	0.01%
Sum in quadr.			0.6%

Table 5.2: Non-kinematic uncertainties associated with the ^{3}He(e,e) elastic measurements, and the total uncertainty of the measurements.

Quantity	Uncertainty
Deadtime	1%
Solid angle	1%
Cut on target length	1.4%
Cut on elastic peak	0.2%
Stat. uncertainty	0.5%
^{3}He form factor uncertainty	1.5%
Tracking efficiencies	0.5%
Radiative corrections	1%
Accum. beam charge	0.5%
Sum in quadr.	%
Kinematic uncertainty	0.6%
Total kin+non-kin in quadr.	2.9%

Table 5.3: Top part of the table: sensitivities of extracted $^3\mathrm{He(e,e'p)pn}$ cross sections to uncertainties in kinematic parameters, averaged over acceptance. The fifth from the last row gives kinematic uncertainties added in quadrature, assuming uncertainties in the right column. The last row gives total systematic errors of the $^3\mathrm{He(e,e'p)pn}$ measurements, for Σ_1 kinematics.

Kinematic quantity	Kinematic setting						Nominal uncert.
	4	7	10	13	28	29	
E_i, %/(10^{-3} rel.)	11.7	6.1	2.4	7.5	1.9	1.7	$2 \cdot 10^{-4}$
ϕ_i, %/mr	4.1	1	1.4	0.01	2.4	2.7	0.1 mr
θ_i, %/mr	0.1	0.1	0.1	0.2	0.1	0.2	0.1 mr
E_e, %/(10^{-3} rel.)	9.9	5.2	1.6	5.9	1	0.8	$5 \cdot 10^{-4}$
ϕ_e, %/mr	0.1	1.1	2.1	2.1	2.8	3	0.3 mr
θ_e, %/mr	0.04	0.1	0.1	0.2	0.1	0.05	2 mr
P_p, %/(10^{-3} rel.)	0.4	0.02	0.005	0.04	0.1	0.2	$1 \cdot 10^{-3}$
ϕ_p, %/mr	3.8	2	0.6	2.1	0.4	0.3	0.3 mr
θ_p, %/mr	0.008	0.04	0.02	0.1	0.01	0.005	2 mr
Sum in quadr., %	5.6	3	1.2	3.5	1.1	1.1	
Non-kin. error, %	3.4	3.4	3.4	3.4	3.4	3.4	
Sum in quadr., %	6.6	4.5	3.6	4.9	3.6	3.6	
Normal. error, %	2.9	2.9	2.9	2.9	2.9	2.9	
Total error, %	7.2	5.4	4.6	5.7	4.6	4.6	

5.7.2 Uncertainties in the $^3\mathrm{He(e,e'p)pn}$ analysis

Tables 5.3 and 5.4 summarizes the kinematic uncertainties for this thesis. The non kinematic uncertainties are reported in Table 5.5.

Table 5.4: Same as Table 5.3 for Σ_2 and Σ_3 kinematics.

Kinematic quantity	Kinematic setting									Nominal uncert.
	5	8	11	14	3	6	9	12	15	
E_i, %/(10^{-3} rel.)	13.6	3.6	3.3	1.7	1.2	1	1	0.6	1.4	$2 \cdot 10^{-4}$
ϕ_i, %/mr	11.2	5.7	6.7	5	0.7	3.2	1.3	0.2	1.3	0.1 mr
θ_i, %/mr	0.2	0.04	0.05	0.03	0.02	0.1	0.03	0.006	0.02	0.1 mr
E_e, %/(10^{-3} rel.)	13.5	3.8	4	2.2	0.01	0.7	0.2	0.1	0.1	$5 \cdot 10^{-4}$
ϕ_e, %/mr	6.3	3.9	4.9	3.6	0.2	1.1	0.7	0.4	0.9	0.3 mr
θ_e, %/mr	0.2	0.03	0.04	0.02	0.008	0.02	0.01	0.003	0.006	2 mr
P_p, %/(10^{-3} rel.)	1.2	0.3	0.1	0.1	1.9	0.7	0.2	0.03	0.01	$1 \cdot 10^{-3}$
ϕ_p, %/mr	4.9	1.6	1.9	1.2	1	4.3	2.1	0.6	2.1	0.3 mr
θ_p, %/mr	0.1	0.01	0.007	0.005	0.02	0.1	0.04	0.009	0.02	2 mr
Sum in quadr., %	7.8	2.5	2.7	1.7	1.9	1.6	0.7	0.3	0.8	
Non-kin. error, %	3.4	3.4	3.4	3.4	3.4	3.4	3.4	3.4	3.4	
Sum in quadr., %	8.5	4.2	4.3	3.8	3.9	3.8	3.5	3.4	3.5	
Normal. error, %	2.9	2.9	2.9	2.9	2.9	2.9	2.9	2.9	2.9	
Total error, %	9.0	5.1	5.2	4.8	4.9	4.8	4.5	4.5	4.5	

Table 5.5: Non-kinematic errors associated with the $^3\mathrm{He}(\mathrm{e},\mathrm{e}'\mathrm{p})\mathrm{pn}$ cross section measurements.

Quantity	Error
Deadtime	1%
Solid angle	2%
Cut on target length	1.4%
Subtraction of 2bbu Radiative tail.	2%
Transfer of ^{3}He density	0.5%
Tracking efficiency	1%
Luminosity monit. stat.	$< 0.1\%$
Radiative corrections	2%
Sum in quadrature	4.02%

Chapter 6

Results and Discussion

6.1 $^3\mathrm{He(e,e'p)d}$ results

The $^3\mathrm{He(e,e'p)d}$ data analysis was part of the PhD. thesis of M. Rvachev [23, 48]. A brief summary of the most important obtained results is given in this section.

The $^3\mathrm{He(e,e'p)d}$ cross section was extracted using the simulation program MCEEP [39], taking into account the effects of internal and external radiation, particles' energy loss, deviations from monochromaticity of the beam, and spectrometer resolutions. Simulated event yields were adjusted separately varying the $^3\mathrm{He(e,e'p)d}$ and $^3\mathrm{He(e,e'p)pn}$ cross sections in the simulation, until the simulated yield was equal to the detected yield in each (E_m, P_m) kinematic bin [23]. Cross sections were extracted from the re-weighted $^3\mathrm{He(e,e'p)d}$ yield, corrected for radiation, and for contributions from $^3\mathrm{He(e,e'p)pn}$ to each $^3\mathrm{He(e,e'p)d}$ kinematic bin (on average, these contributions were about 3%). Within each kinematic bin, the simulated $^3\mathrm{He(e,e'p)}$ cross section was assumed to vary as the cc1 prescription of de Forest [19] for the off-shell electron-proton cross section. This technique allows one to separate the P_m dependence of the reaction from the rapid dependence on the electron kinematics [23]. In addition to the over-all normalization uncertainty (3%, see above) the over-all systematic uncertainty was 3.4%, dominated by uncertainties in the solid angle (2.0%), the selection (E_m cut) of the two-body break-up reaction channel (1.5%) and the knowledge of the target length (1.4%).

The extracted $^3\mathrm{He(e,e'p)d}$ cross section is plotted in Fig. 6.1 as a function of P_m. We note that the range of P_m measured (resulting in measured cross-section magnitudes varying over six orders of magnitude), is significantly larger than in any other previous measurement. Moreover, contrary to previous experiments [20], our measurements over this entire range were performed at a fixed electron kinematics.

Also displayed in Fig. 6.1 are four theoretical curves by Laget. The Hannover calculations by Laget use the Hannover bound-nucleon wave function [56] corresponding to the solution to the three-body Faddeev equation with the Paris NN potential and no three-body forces. The AV18+UIX curves are the same PWIA and full calculations respectively, but with a bound-state nuclear wave function derived by a variational technique using the Argonne V18 NN potential and the Urbana IX three-body force [19]. All calculations use a diagrammatic approach. The kinematics as well as the nucleon and meson propagators are relativistic, and no restricted angular (Glauber type) approximation has been made in the various loop integrals. Details of the model can be found in [57]. The PWIA curves include only one-body interactions, while the full calculations include FSI, meson (π and ρ) exchange and intermediate Δ formation currents as well as three-body (three nucleon π double scattering) amplitudes. The FSI in these calculations uses a global parameterization of the NN scattering amplitude, obtained from experiments in LANL, SATURNE and COSY [58]. On this scale, the differences between the calculations using the two ground-state wave functions are very small. By far, FSI constitute the major difference between the full and PWIA calculations. Meson exchange and intermediate Δ current contributions are generally small (up to 20-25%), and the three-body FSI contributions are negligible [58].

Three regions of P_m are observed in Fig. 6.1. For $|\vec{P}_m|$ below ~150 MeV/c, where the recoiling deuteron can be viewed as only marginally involved in the interaction, the data are expected to be dominated by the single-proton characteristics of the ^{3}He wave function. As can be observed, both PWIA and full curves describe the data quite well, and the difference between them is rather small. For $|\vec{P}_m|$ between 150 and 750

MeV/c, the cross section is expected to be dominated by the dynamics of the reaction. Indeed, very large contributions from dynamical effects are observed. While Laget's full calculations describe the data very well, the PWIA curve over- (under-) predicts the data by up to an order of magnitude for $|\vec{P}_m|$ below (above) 300 MeV/c. This difference between the two curves is very much dominated by FSI. At x_B=1, the on-shell rescattering of the fast nucleon on a nucleon at rest is preferred and the contribution of FSI is maximal. Because the NN scattering amplitude is almost purely absorptive in the JLab energy range, the corresponding FSI amplitude interferes destructively with the PWIA amplitude below, and constructively above P_m ~300 MeV/c [57]. For P_m larger than 750 MeV/c, Laget's calculations grossly under-predict the measured cross section by more than an order of magnitude. Whether it is a consequence of the truncation of the diagrammatic expansion or a signature of other degrees of freedom is an open question. The sensitivity of the data to the details of the wave function at low $|\vec{P}_m|$ is shown in Fig. 6.2. In order to enhance the details, Fig. 6.2 displays the low $|\vec{P}_m|$ subset of the data from Fig. 6.1 as a ratio to Laget's full calculations using the Hannover ground-state wave function. Also displayed are the ratios to the same calculation of Laget's full AV18+UIX and the two corresponding PWIA curves. As already noted, in the low $|\vec{P}_m|$ region, reaction effects such as FSI and two-body currents are relatively small, and the curves are mainly sensitive to the details of the bound-nucleon wave function. For P_m below 50 MeV/c, the calculations are purely co-planar perpendicular kinematics whereas experimentally, because of the large $|\vec{q}|$, it is difficult to avoid contamination with parallel and out-of-plane components. For $|\vec{P}_m| > 50$ MeV/c, we observe that the best agreement with the data is of the full AV18+UIX curve. We suggest that this better agreement with the data is related to the fact that the wave function generated from the AV18+UIX potentials reproduces the correct ^{3}He binding energy, while the Hannover wave function that does not include three-body forces underbinds the ^{3}He by $\sim$ 0.7 MeV.

Thus the AV18+UIX wave function provides a generally better description of the

^{3}He nuclear structure.

The A_{TL} asymmetry was extracted for $0 \leq |\vec{P}_m| \leq 660$ MeV/c according to

$$A_{TL} = \frac{\sigma_{right} - \sigma_{left}}{\sigma_{right} + \sigma_{left}}, \tag{6.1}$$

where σ_{right} and σ_{left} are coplanar $^3\mathrm{He(e,e'p)d}$ cross sections measured right and left of the transferred-momentum $\vec{q}$ direction. In the extraction of A_{TL}, the phase-space acceptances of kinematic bins on both sides of $\vec{q}$ were matched in P_m, ω, and $|\vec{q}|$. The A_{TL} observable downplays the significance of the ground-state wave function, by virtue of the ratio involved in its definition [15] and there exist indications that it is sensitive to relativistic effects [59] and to mechanisms that break the simple factorization scheme of PWIA cross sections [60].

Figure 6.3 displays the extracted A_{TL} data with the PWIA and full calculations by Laget using the two ground-state wave functions described above. The difference in the two ground-state wave functions has a very small effect in the full calculations. In contrast to the PWIA calculations, the measured A_{TL} displays a structure characteristic of broken factorization [60]. Both of Laget's full calculations describe the data reasonably well by displaying similar structures. Such structure in A_{TL} was previously observed in the quasielastic removal of p-shell protons in the $^{16}\mathrm{O}(e,e'p)$ reaction [61], and was well reproduced by relativistic distorted-wave impulse approximation calculations by Udias *et al.* [62]. In that case, broken factorization was attributed to dynamical relativistic effects. However, these effects are marginal in our case because of the low nuclear density of ^{3}He [63]. Rather, in our case, the factorization is broken because of the strong interference between the PWIA and re-scattering amplitudes [57].

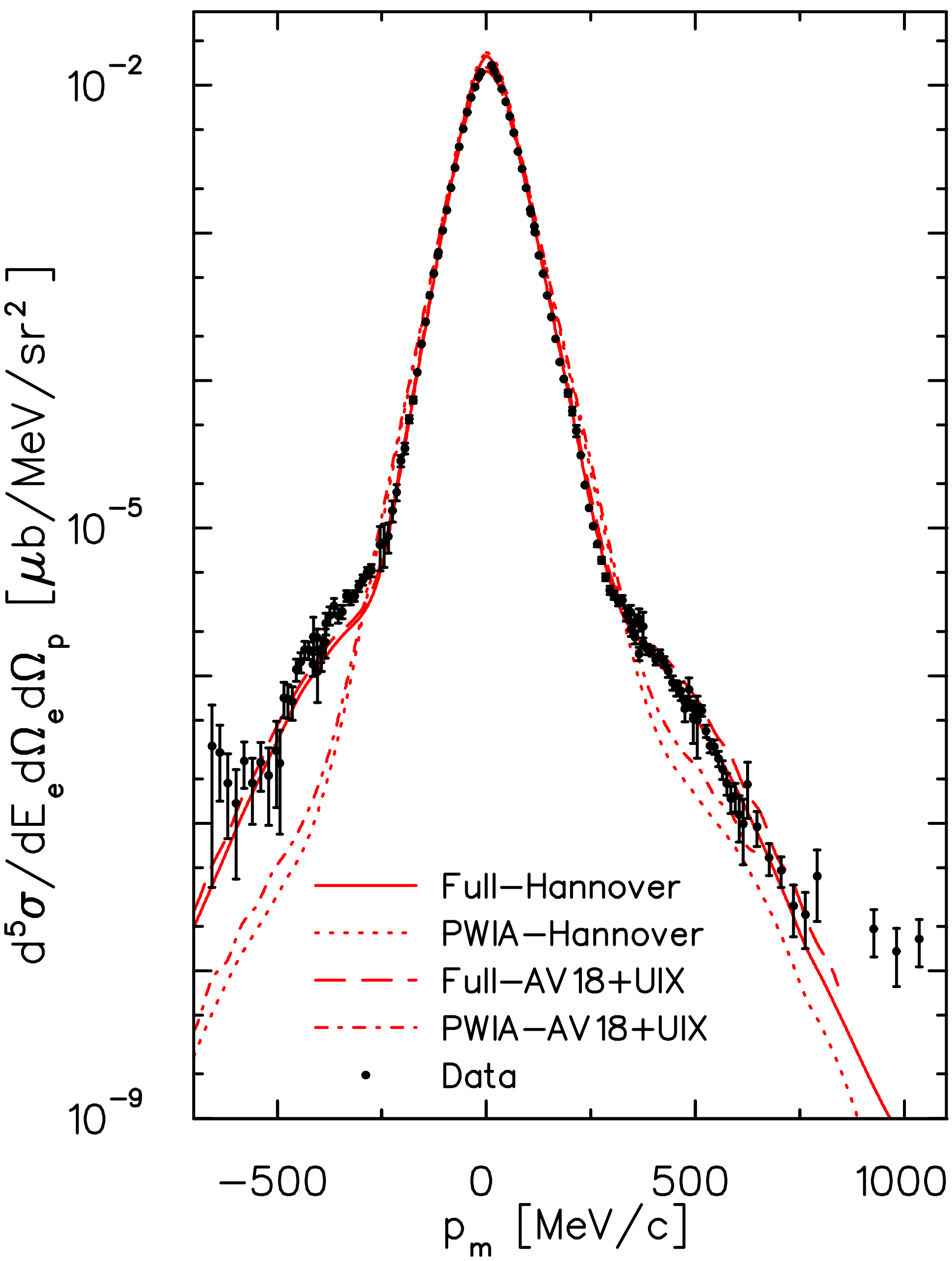

Figure 6.1: Measured $^3\mathrm{He}(\mathrm{e},\mathrm{e}'\mathrm{p})\mathrm{d}$ cross section as a function of the missing momentum, P_m. Negative (positive) P_m correspond to protons detected left (right) of $\vec{q}$. Also displayed are two pairs of PWIA and full calculations by Laget. The two pairs differ in the ground-state wave function. See text for details.

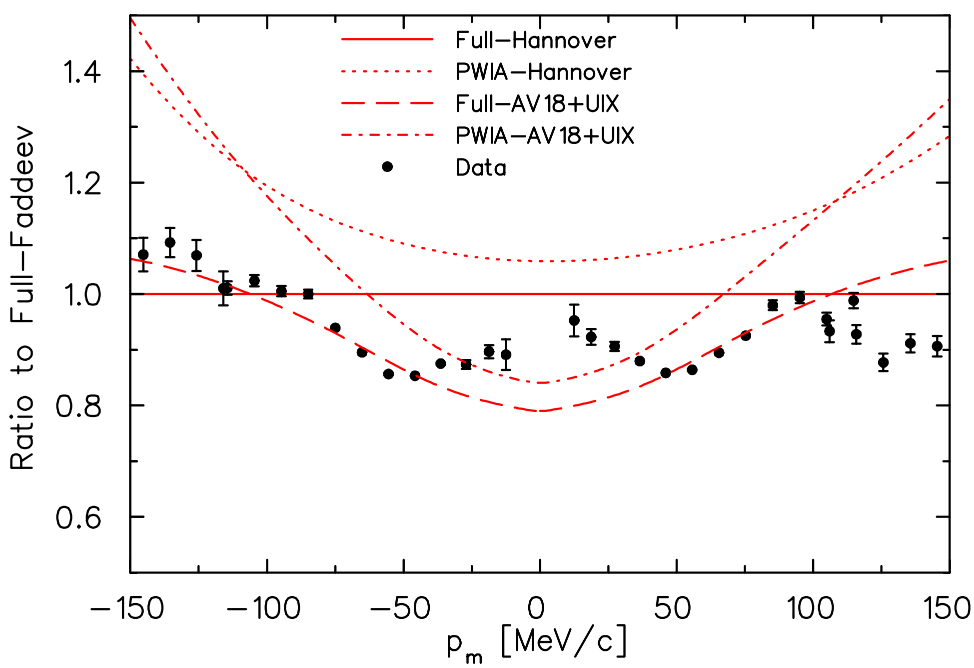

Figure 6.2: Same data as in Fig. 6.1 for low P_m only, but shown as a ratio to Laget's full calculations using the Hannover ground-state wave function (gswf). Also shown are the ratios to the full calculations that use the Hannover gswf of Laget's full calculations using the gswf generated from the AV18 NN potential and the Urbana IX three-nucleon force, as well as the two corresponding PWIA curves. See text for details.

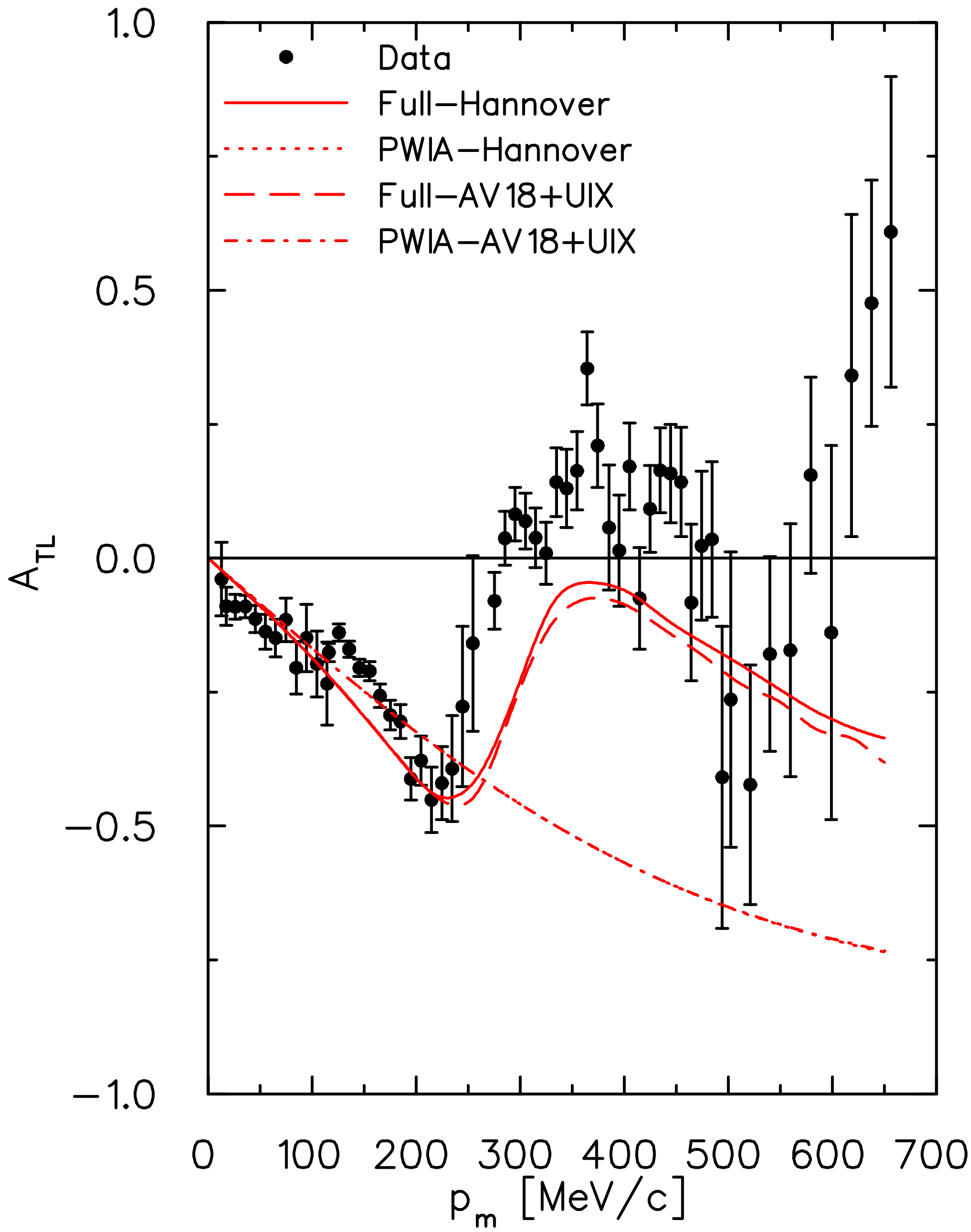

Figure 6.3: The measured A_{TL} asymmetry. The curves are the same four calculations by Laget used in Figs. 6.1 and 6.2; by definition, the two PWIA curves are indistinguishable.

6.2 $^3\mathrm{He}(\mathrm{e},\mathrm{e}'\mathrm{p})\mathrm{pn}$ results and discussion

Results of the JLab Hall A quasielastic $^3\mathrm{He}(\mathrm{e},\mathrm{e}'\mathrm{p})\mathrm{pn}$ measurements are presented. These measurements were performed at fixed transferred momentum and energy, q = 1.5 GeV/c and ω = 840 MeV, respectively, for missing momenta P_m up to 1 GeV/c and missing energies 7.72 MeV $\leq E_m \leq$ 140 MeV in the continuum region, up to pion threshold [64, 65]; this kinematic coverage is much more extensive than that of any previous experiment.

The cross section data are presented along with the effective momentum density distribution and compared to existing theoretical models. The simplest calculation is a PWIA calculation using Salme's spectral function [49] and the σ_{cc1} electron-proton off-shell cross section [19]. Also results of microscopic calculations of the continuum cross section by J. M. Laget [66], including a plane-wave impulse approximation, and successive implementation of various interaction effects are provided.

6.2.1 Cross section results

Some of the continuum $^3\mathrm{He}(\mathrm{e},\mathrm{e}'\mathrm{p})\mathrm{pn}$ cross section results [64,65] extracted in this work are presented in Figs. 6.4 to 6.7. The corresponding tabulated values are given in the end of this chapter. The results are compared to the available theoretical models. The energy scale in the horizontal axis has been shifted in these plots so that the 3bbu channel starts at 0.

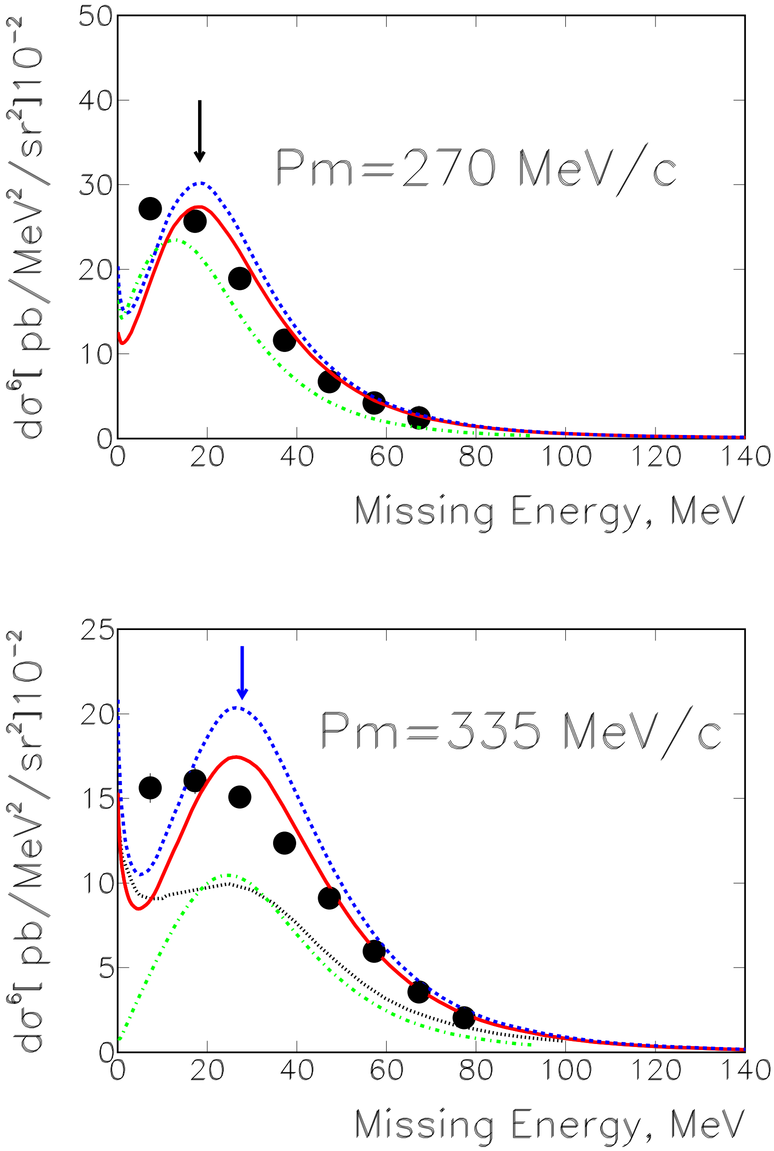

Figure 6.4: Cross-section results for the $^3\mathrm{He}(\mathrm{e},\mathrm{e}'\mathrm{p})\mathrm{pn}$ reaction versus missing energy E_m for missing momenta $\mathrm{P}_m = 270 \pm 10$ MeV/c (upper plot) and $\mathrm{P}_m = 335 \pm 5$ MeV/c (lower plot). The siginficance of the arrow will be given in Sec. 6.2.2.

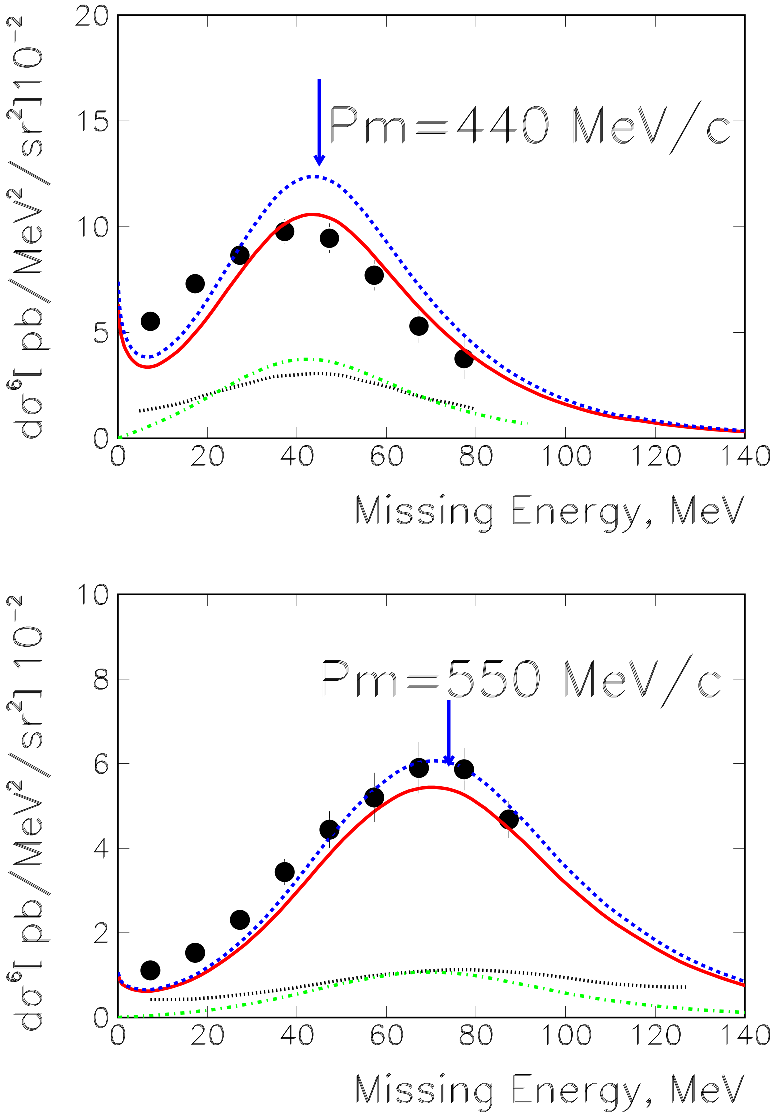

Figure 6.5: Cross-section results for the $^3\mathrm{He(e,e'p)pn}$ reaction versus missing energy E_m for missing momenta $\mathrm{P}_m = 440 \pm 5$ MeV/c (upper plot) and $\mathrm{P}_m = 550 \pm 5$ MeV/c (lower plot). Curves are the same as in Fig. 6.4.

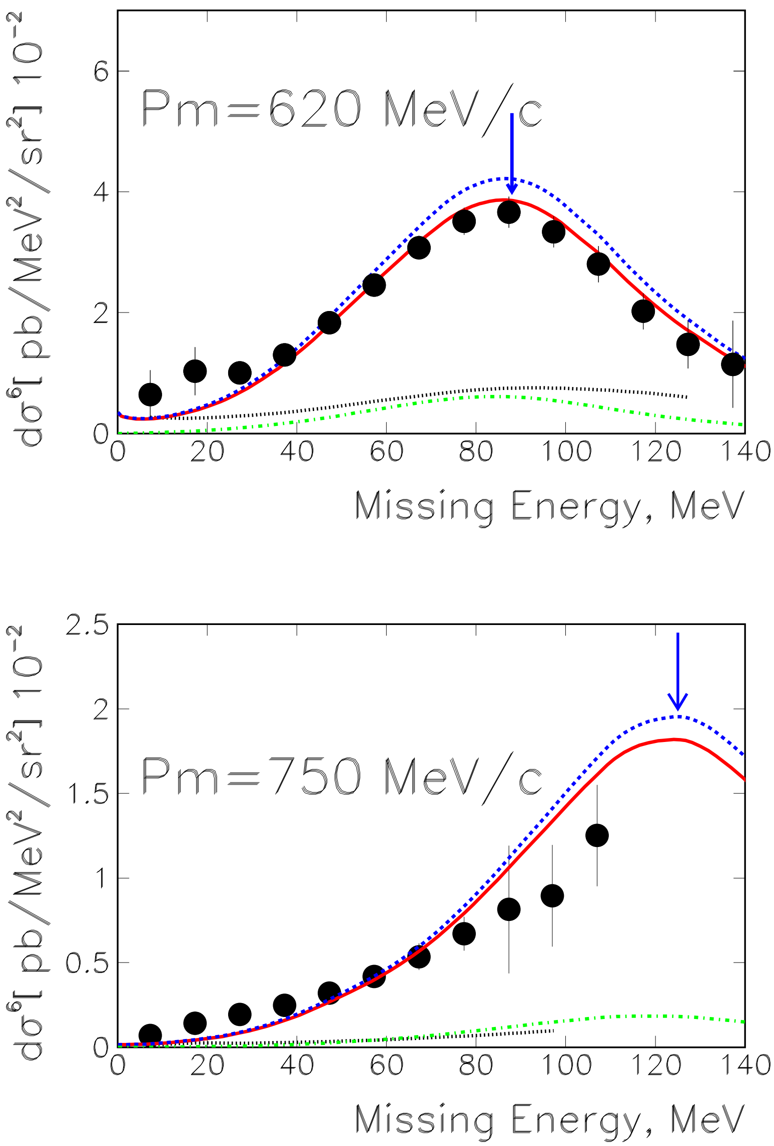

Figure 6.6: Cross-section results for the $^{3}\mathrm{He}(\mathrm{e},\mathrm{e}'\mathrm{p})\mathrm{pn}$ reaction versus missing energy E_m for missing momenta $\mathrm{P}_m = 620 \pm 5$ MeV/c (upper plot) and $\mathrm{P}_m = 750 \pm 5$ MeV/c (lower plot). Curves are the same as in Fig. 6.4.

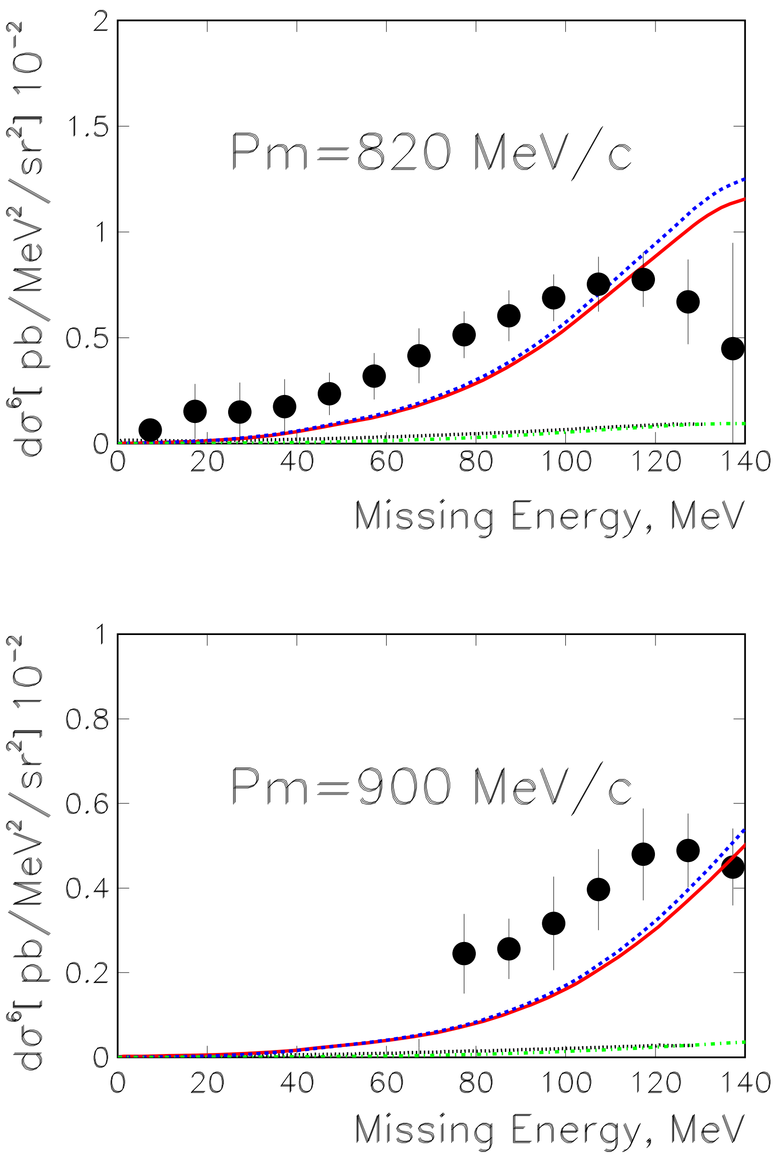

Figure 6.7: Cross-section results for the $^3\mathrm{He(e,e'p)pn}$ reaction versus missing energy E_m for missing momenta $\mathrm{P}_m = 820 \pm 10$ MeV/c (upper plot) and $\mathrm{P}_m = 720 \pm 10$ MeV/c (lower plot). Curves are the same as in Fig. 6.4.

.

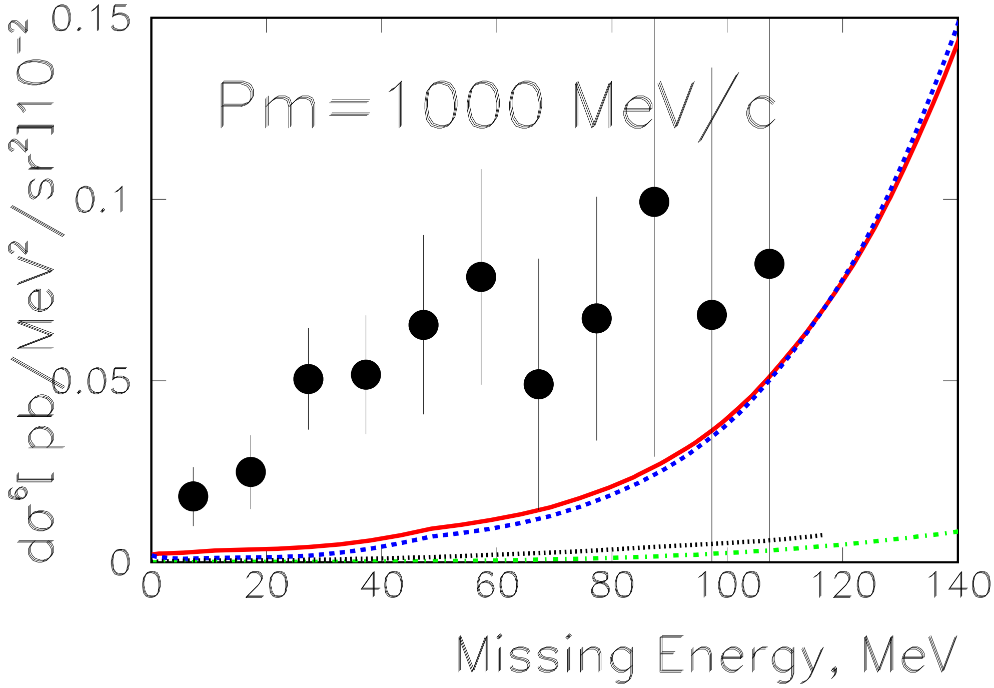

Figure 6.8: Cross-section results for the $^3\mathrm{He(e,e'p)pn}$ reaction versus missing energy E_m for missing momentum $P_m = 1025 \pm 25$ MeV/c. Curves are the same as in Fig. 6.4.

.

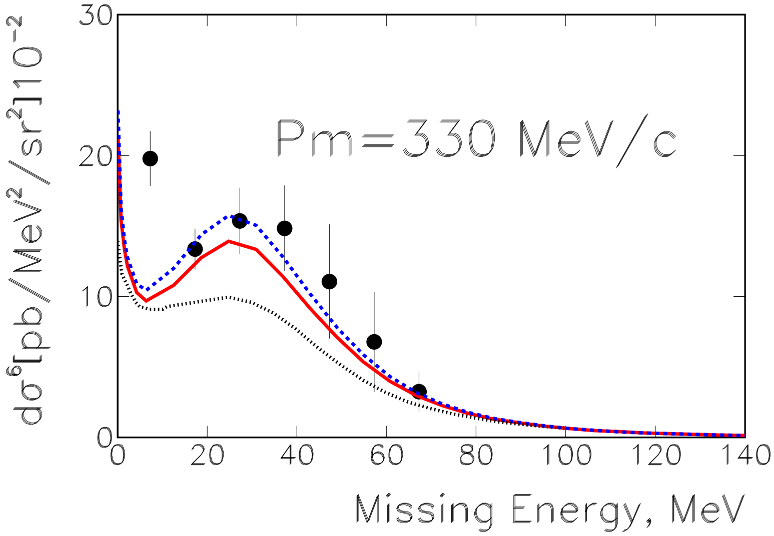

Figure 6.9: Cross-section results for the $^3\mathrm{He}(\mathrm{e},\mathrm{e}'\mathrm{p})\mathrm{pn}$ reaction versus missing energy E_m for missing momentum P$_m$ = 330 ±10 MeV/c from the Σ_2 kinematics 8.Curves are the same as in Fig. 6.4.

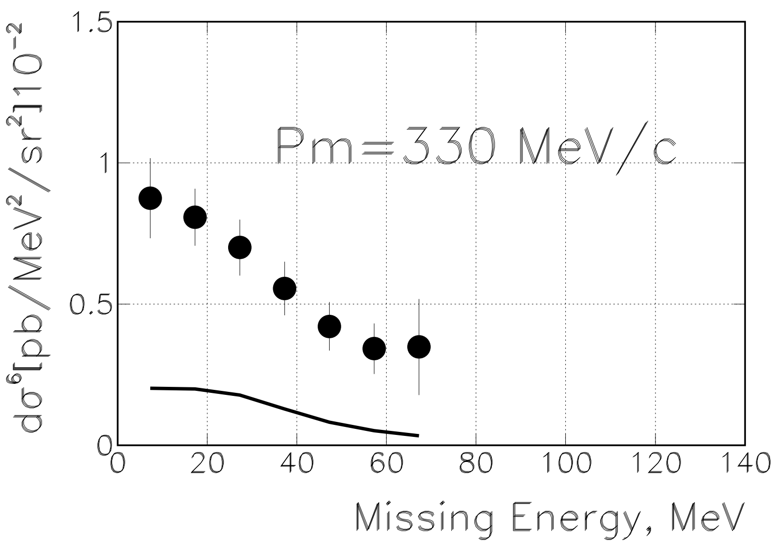

Figure 6.10: Cross-section results for the $^3\mathrm{He}(\mathrm{e},\mathrm{e}'\mathrm{p})\mathrm{pn}$ reaction versus missing energy E$_m$ for missing momentum P$_m$ = 330 ±25 MeV/c from the Σ_3 kinematics 9. The black curve presents a PWIA calculation using Salme's spectral function and σ_{cc1} electron-proton off-shell cross section.

6.2.2 Theoretical interpretation

Figure 6.11 represents a unified picture of the cross-section results for the $^3\mathrm{He(e,e'p)pn}$ reaction versus missing energy E_m when going from lower to higher values in P_m. Figures from Fig. 6.4 to 6.7 are reproduced in the same picture.

As P_m increases, we can see that the broad peak in the cross section moves to higher missing energies. The arrow in the figure indicates where one would expect the peak in the cross section due to the photon coupling to a nucleon in a correlated pair at rest inside the ^{3}He nucleus; the expected peak position for $P_m = 820$ MeV/c is just off scale, at $E_m \approx 145$ MeV. The close correspondence of the peak in the data with the arrow indicates the importance of two-nucleon processes such as correlations. The peak width reflects the motion of the center of mass of the correlated pair.

Several calculations are presented in Fig. 6.11. The simplest calculation is a PWIA calculation using Salme's spectral function [49] and the σ_{cc1} electron-proton off-shell cross section [19]. Also shown in Fig. 6.11 are the results of microscopic calculations of the continuum cross section by J. M. Laget [66], including a plane-wave impulse approximation, and successive implementation of various interaction effects. contributions. The calculation is based on a diagrammatic expansion of the reaction amplitude, up to and including two loops [67]. Both single and double NN scattering, as well as meson exchange and Δ formation are included. The bound-state wave function is a solution of the Faddeev equation used by the Hannover group [68] for the Paris potential [69]. Details of the model can be found in [57]. The kinematics are relativistic, nucleon and meson propagators are relativistic and no angular approximations (Glauber) have been made in the various loop integrals. At low energies, below NN relative kinetic energy of about 500 MeV, the NN amplitude is the solution of the Lippman-Schwinger equation for the Paris potential. In our experiment, the NN relative kinetic energy is higher (T_{NN} = 840 MeV) and the absorptive part of the interaction dominates the NN scattering amplitude - the implementation is explained in [58].

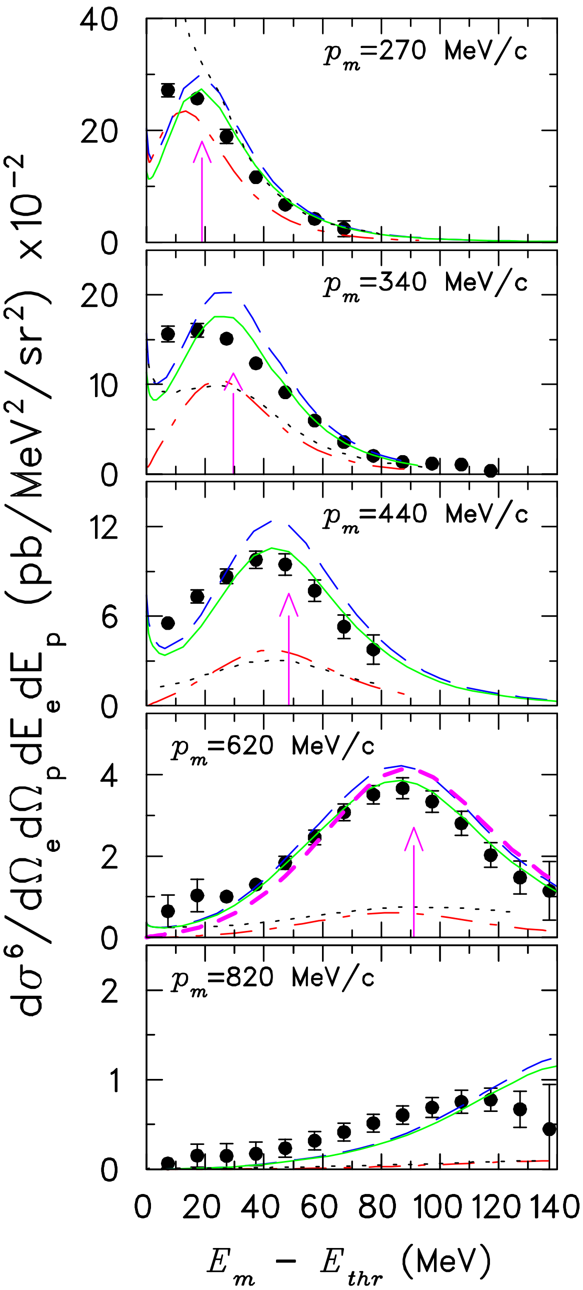

Figure 6.11: Cross-section results for the $^3\mathrm{He}(\mathrm{e},\mathrm{e}'\mathrm{p})\mathrm{pn}$ reaction versus missing energy E_m. The vertical arrow gives the peak position expected for disintegration of correlated pairs. The dotted curve presents a PWIA calculation using Salme's spectral function and σ_{cc1} electron-proton off-shell cross section. Other curves are recent theoretical predictions of J. M. Laget from the PWIA (dash dot) to PWIA + FSI (long dash) to full calculation (solid), including meson exchange current and final state interactions. In the 620 MeV/c panel, the additional short dash curve is a calculation with PWIA + FSI only within the correlated pair.

We can see from the figure that the cross sections, especially at large P_m, are strongly enhanced by final-state interactions. FSI between the two active nucleons - see Fig. 1.6b - increase the cross section by a factor of about four. While rescattering between one nucleon in the correlated pair and the third nucleon - see Fig. 1.6c - might be expected to modify the shape of the distribution, the effects are slight; this is indicated by the additional calculation included in the 620 MeV/c panel of Fig. 6.11, in which FSI with the spectator nucleon are turned off. Neither the shape nor magnitude of the peak is much affected. MEC effects are small (around 15%).

6.3 Effective momentum density distribution results

Figure 6.12 shows the effective momentum density distribution, obtained by integrating the theory and cross-section data, such as those shown in Fig. 6.11, over missing energy from threshold to 140 MeV, as discussed above - see Eq. 1.11. Uncertainties from missing tails of the 3bbu peak, within this integration range, due to limited experimental acceptance are negligible on the scale of Fig. 6.12. The 3bbu distribution is not the same shape as the 2bbu distribution from [48]. The 3bbu distribution tends to have a much larger relative strength for high missing momentum, suggesting an important role for correlations.

The relative importance of the underlying processes can be investigated within theories. The PWIA curve includes conventional correlations in the ^{3}He wave function but not final state interactions. Since the PWIA calculations show an order of magnitude enhancement of the 3bbu over the 2bbu at high missing momentum, we can infer that the relative enhancement of the 3bbu is largely from correlations. Here, the two-body correlations are more clearly seen in 3bbu than in the 2bbu, where the available phase space is reduced since two nucleons are forced to form the deuteron. The differences between the PWIA calculations and the data and full calculations further indicate the

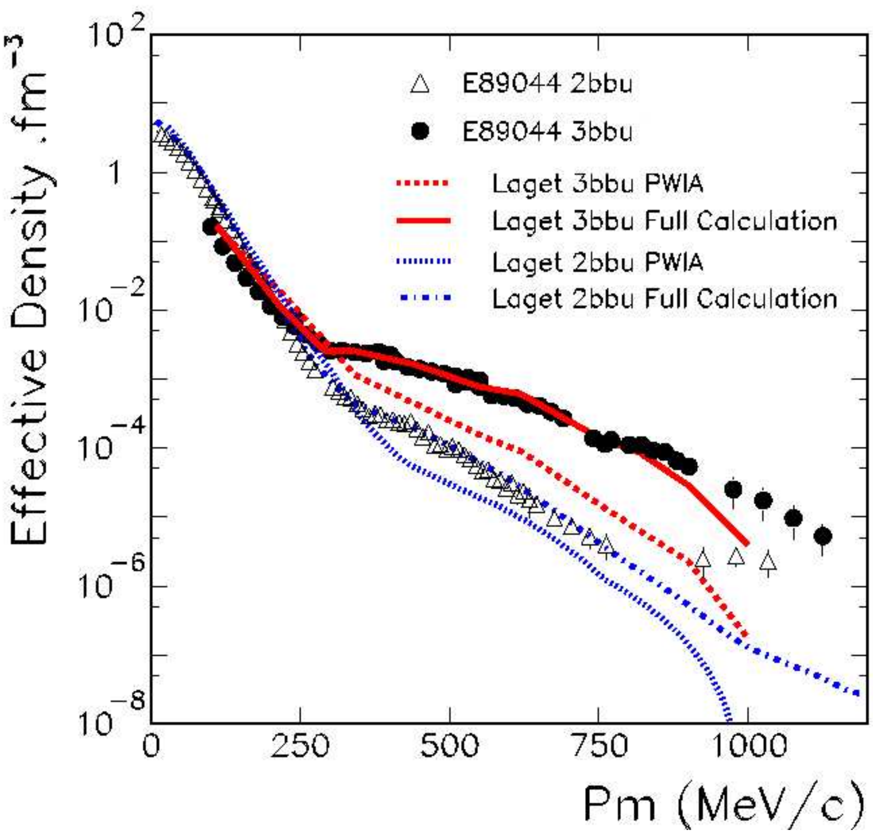

Figure 6.12: Proton effective momentum density distributions in ^{3}He extracted from $^{3}\mathrm{He(e,e'p)pn}$ (filled black circles) and $^{3}\mathrm{He(e,e'p)d}$ (open black triangles), compared to calculations from Laget. The 3bbu integration covers E_M from threshold to 140 MeV.

greater importance of final-state interactions in the 3bbu. The generally good agreement of the full calculations shown in Figs. 6.11 and 6.12 indicates that, at this level of comparison, there is no need for correlations beyond those already present in a modern conventional nuclear physics model.

The conclusions described above might appear to be no longer valid for $P_m \approx 1$ GeV/c. Here the 2bbu distribution flattens out, while the 3bbu distribution continues to fall. This behavior is contrary to what one would expect from the importance of correlations. At these very high P_m, however, one has to be careful about drawing conclusions.

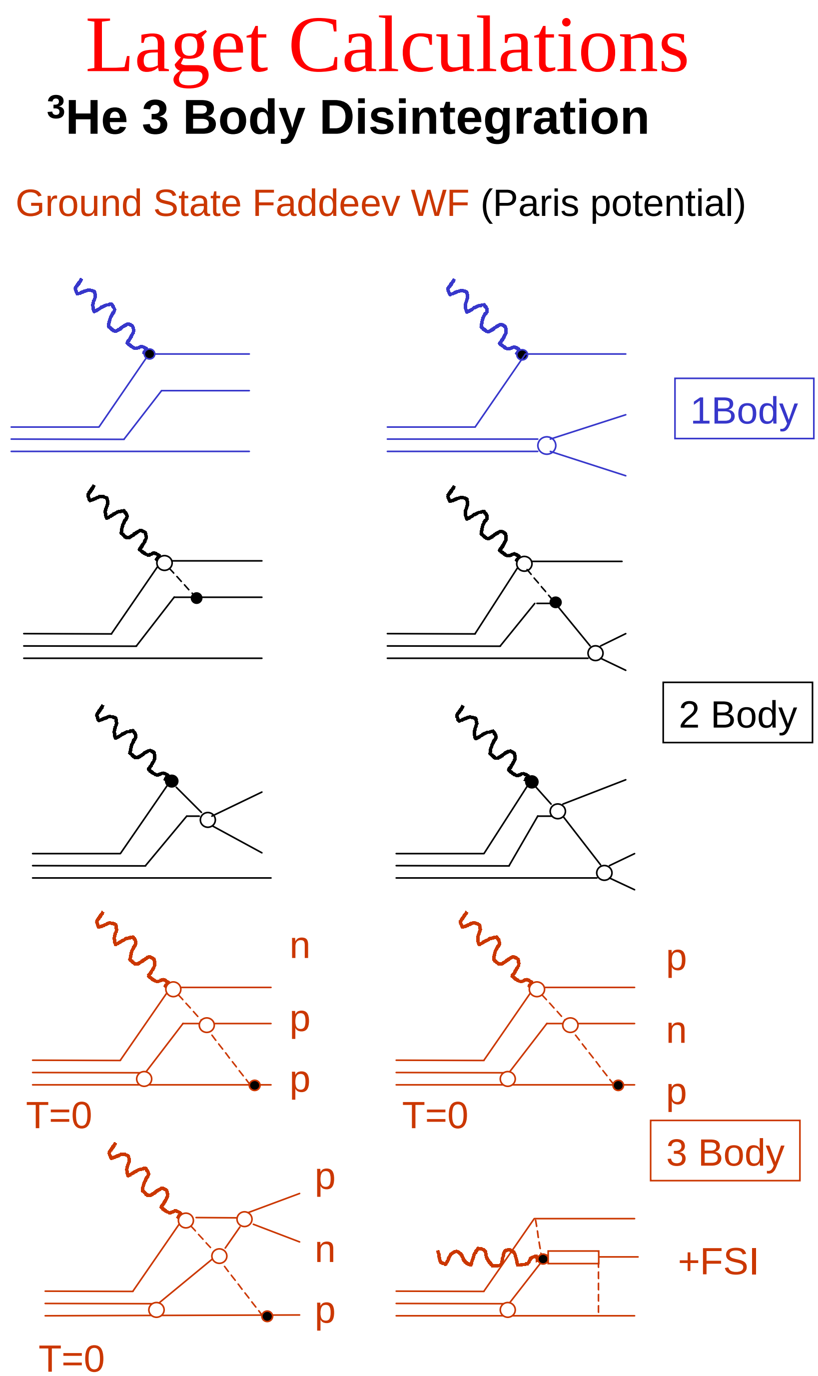

Figure 6.13: Diagrammatic approach of J. M. Laget. Figure from J. M. Laget.

The center of the 3bbu correlation peak moves past $E_m = 140$ MeV, outside of the integration range and into the pion production region, at $P_m \approx 800$ MeV/c, as shown in Fig. 6.11. Thus, the experimental integration is only including a fraction of the 3bbu strength at large P_m, leading to the apparent narrowing of the gap between the 2bbu and 3bbu. Thus, a correction is needed for a more meaningful comparison of 3bbu to 2bbu at large P_m We have estimated the fraction of the strength missed by our experimental integration by calculating what fraction of the total strength of the Laget full calculation lies in the region $E_m < 140$ MeV. This is only a crude estimate, since a close examination of Fig. 6.11 shows that the calculation has a tendency to underpredict the cross section for the low E_m tail of the correlation peak. The estimated correction factors for the missing 3bbu strength are about 1.05, 2, and 20 for P_m = 600, 800, and 1000 MeV/c, respectively. Applying the correction to the 3bbu would cause the distribution to roughly flatten out, starting near 750 MeV/c, at a level nearly two orders of magnitude greater than that of the 2bbu. These observed correction factors also lead to our stopping the calculation at 1 GeV/c; the comparison between data and theory is no longer meaningful when only a small fraction of the tail of the distribution is considered. Given these data along with the theoretical calculations, it remains fair to conclude that the correlations in the wave function preferentially lead to the 3bbu channel, and that the reaction mechanism is reasonably well understood in a modern, conventional nuclear physics model.

6.4 Transverse-longitudinal asymmetry results

Details of the extraction of the transverse-longitudinal asymmetry A_{TL} for the three-body reaction are given in Sec. 5.6. The asymmetry A_{TL} is obtained by combining the cross sections from both sides of the momentum transfer as in Eq. 5.14. Figure 6.14 shows cross section results for kinematics 7 (Σ_1) and kinematics 8 (Σ_2) for a missing energy bin P_m = 330 MeV/c. The resulting A_{TL} asymmetry is shown in Fig. 6.15 and the data is compared to the predictions of J. M. Laget and the PWIA using Salme's spectral function and σ_{cc1} electron-proton off-shell cross section; details of the models are given in Sec. 6.2.2. In this figure, the full calculation of J. M. Laget (PWIA + FSI + MEC) is 4 times higher than the plane wave predictions, and the disagreement with the data can be explained with the symmetry breaking due mostly to final state interaction. This behavior was also observed in the transverse-longitudinal asymmetry in the case of the two-body break-up channel around P_m = 330 MeV/c as shown in Fig. 6.3.

Cross section results for kinematics 10 (Σ_1) and kinematics 11 (Σ_1) are presented in Fig. 6.16 for missing momentum bin P_m = 440 MeV/c. The resulting A_{TL} is presented in Fig. 6.17. This time, only Salme's theoretical calculations along with the σ_{cc1} electron proton off-shell cross section is available. The predictions of the PWIA calculation are lower than the experimental results. This was also observed in Fig. 6.3 in the case of $^3\mathrm{He(e,e'p)d}$ reaction.

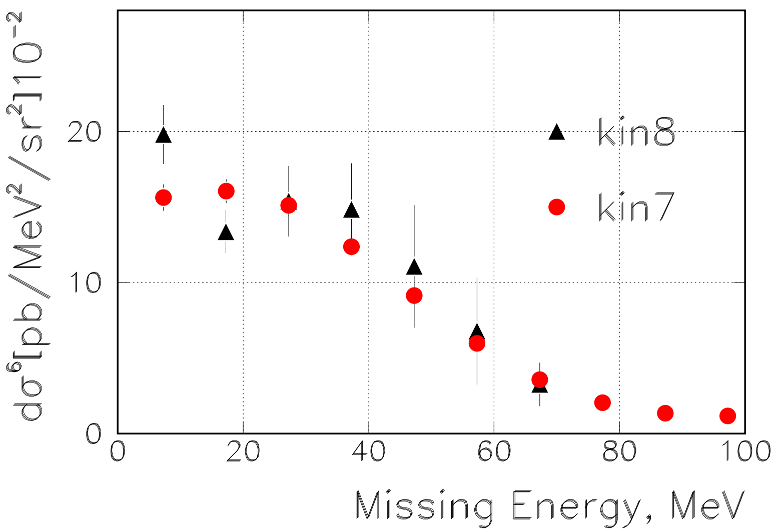

Figure 6.14: Comparison of the cross section for kinematics 8 and kinematics 7 for missing energy bin $P_{miss} = 330 \pm 5$ MeV/c.

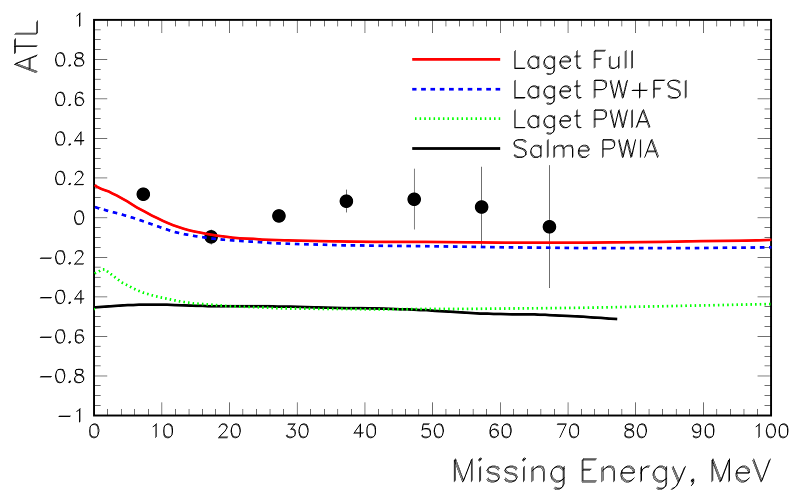

Figure 6.15: A_{TL} Asymmetry extracted at the missing energy bin $P_{miss} = 330 \pm 5$ MeV/c from kinematics 7 and kinematics 8.

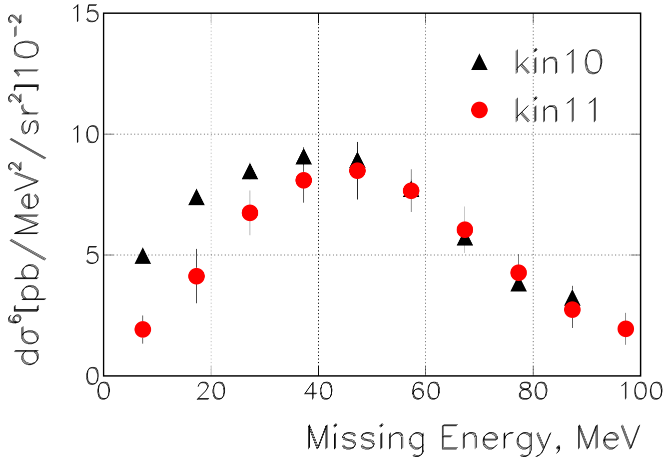

Figure 6.16: Comparison of the cross section for kin8 and kin7 for missing energy bin $P_{miss} = 440 \pm 10$ MeV/c.

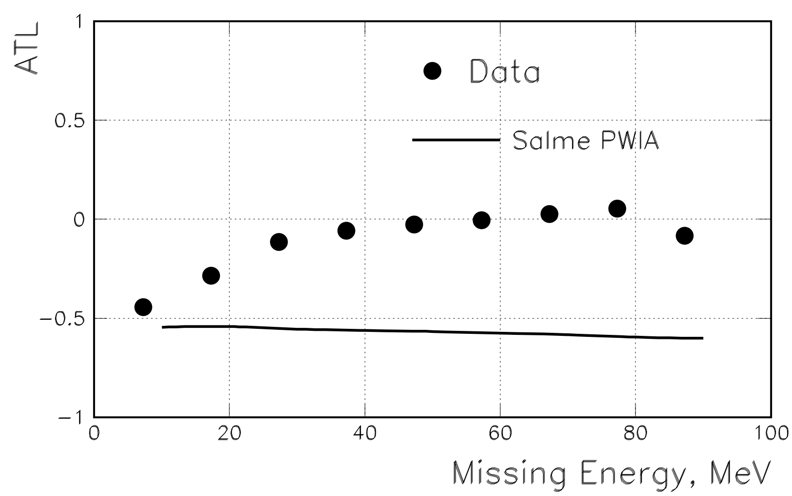

Figure 6.17: A_{TL} Asymmetry extracted at the missing energy bin $P_{miss} = 440 \pm 10$ MeV/c from kinematics 10 and kinematics 11.

6.5 Tabulated results

6.5.1 Cross sections tables

Table 6.1: ^{3}He(e,e′p)pn cross section results for P_m=270 MeV/c (kin7).

Em(MeV) (MeV)	Cross Section pb/(MeV^{2}sr^2)10^{-2}	Stat-uncer pb/(MeV^{2}sr^2)10^{-2}	uncer (%)
7.28	27.172	1.162	4.29
17.28	25.677	0.662	4.59
27.28	18.912	1.259	6.06
37.28	11.622	0.922	7.98
47.28	6.728	0.818	12.19
57.28	4.191	0.880	21.82
67.28	2.449	1.414	57.73

Table 6.2: ^{3}He(e,e′p)pn cross section results for P_m = 340 MeV/c (kin7).

E_m (MeV)	Cross Section pb/(MeV^{2}sr^2)10^{-2}	Stat-uncer pb/(MeV^{2}sr^2)10^{-2}	Rel. uncer (%)
7.28	15.627	0.873	5.58
17.28	16.043	0.785	4.89
27.28	15.096	0.662	4.38
37.28	12.353	0.588	4.76
47.28	9.1242	0.503	5.51
57.28	5.9756	0.387	6.48
67.28	3.5692	0.266	7.44
77.28	2.0346	0.190	9.36
87.28	1.3436	0.146	10.88
97.28	1.1670	0.159	13.64
107.28	1.061	0.201	18.98
117.28	0.359	0.118	33.01

Table 6.3: ^{3}He(e,e$'$p)pn cross section results for $P_m = 440$ MeV/c (kin10).

E_m (MeV)	Cross Section pb/(MeV^{2}sr^2)10^{-2}	Stat-uncer pb/(MeV^{2}sr^2)10^{-2}	Rel. uncer (%)
7.28	5.5349	0.352	6.36
17.28	7.3109	0.437	5.98
27.28	8.6608	0.488	5.64
37.28	9.7827	0.574	5.87
47.28	9.4637	0.705	7.45
57.28	7.704	0.719	9.33
67.28	5.298	0.783	14.75
77.28	3.770	0.969	25.67

Table 6.4: ^{3}He(e,e$'$p)pn cross section results for $P_m = 620$ MeV/c (kin10).

E_m (MeV)	Cross Section pb/(MeV^{2}sr^2)10^{-2}	Stat-uncer pb/(MeV^{2}sr^2)10^{-2}	Rel. uncer (%)
7.28	0.646	0.421	65.17
17.28	1.032	0.411	39.80
27.28	1.002	0.140	14.01
37.28	1.298	0.130	9.87
47.28	1.836	0.156	8.66
57.28	2.459	0.176	7.51
67.28	3.075	0.201	6.64
77.28	3.510	0.223	6.36
87.28	3.663	0.260	7.10
97.28	3.3369	0.260	8.14
107.28	2.803	0.301	10.54
117.28	2.024	0.302	15.37
127.28	1.474	0.410	24.42
137.28	1.146	0.720	50.00

Table 6.5: ^{3}He(e,e$'$p)pn cross section results for $P_m = 740$ MeV/c (kin28).

E_m (MeV)	Cross Section pb/(MeV^{2}sr^2)10^{-2}	Stat-uncer pb/(MeV^{2}sr^2)10^{-2}	Rel. uncer (%)
7.28	0.1088	0.037	34.12
17.28	0.1366	0.039	28.61
27.28	0.2343	0.067	28.44
37.28	0.3803	0.092	24.13
47.28	0.5455	0.094	17.17
57.28	0.6804	0.136	19.94
67.28	0.7517	0.154	20.52
77.28	0.7629	0.203	26.56
87.28	0.7464	0.275	36.80
97.28	0.6182	0.317	51.34

Table 6.6: ^{3}He(e,e$'$p)pn cross section results for $P_m = 800$ MeV/c (kin28).

E_m (MeV)	Cross Section pb/(MeV^{2}sr^2)10^{-2}	Stat-uncer pb/(MeV^{2}sr^2)10^{-2}	Rel. uncer (%)
7.28	0.06183	0.0309	50.00
17.28	0.15335	0.0803	52.36
27.28	0.16091	0.0519	32.30
37.28	0.19096	0.0552	28.89
47.28	0.25493	0.0549	21.54
57.28	0.34342	0.0828	24.13
67.28	0.44931	0.0818	18.22
77.28	0.56160	0.0945	16.82
87.28	0.66885	0.1103	16.49
97.28	0.76689	0.1266	16.50
107.28	0.8288	0.1359	16.40
117.28	0.8067	0.1602	19.86
127.28	0.6880	0.4614	67.06
137.28	0.5426	0.3837	70.71

Table 6.7: ^{3}He(e,e′p)pn cross section results for $P_m = 840$ MeV/c (kin28).

E_m (MeV)	Cross Section pb/(MeV^{2}sr^2)10^{-2}	Stat-uncer pb/(MeV^{2}sr^2)10^{-2}	Rel. uncer (%)
27.28	0.02808	0.0118	42.30
37.28	0.11594	0.0432	37.31
47.28	0.22264	0.0543	24.42
57.28	0.29546	0.0716	24.26
67.28	0.35195	0.0758	21.54
77.28	0.40205	0.0777	19.33
87.28	0.46864	0.0799	17.06
97.28	0.54557	0.0817	14.99
107.28	0.63366	0.1037	16.37
117.28	0.72303	0.1186	16.41
127.28	0.72124	0.1374	19.05
137.28	0.65185	0.186	28.66
147.28	0.50989	0.4026	78.96

Table 6.8: ^{3}He(e,e′p)pn cross section results for $P_m = 900$ MeV/c (kin28).

E_m (MeV)	Cross Section pb/(MeV^{2}sr^2)10^{-2}	Stat-uncer pb/(MeV^{2}sr^2)10^{-2}	Rel. uncer (%)
67.28	0.02267	0.02023	89.27
77.28	0.24475	0.09391	38.37
87.28	0.25642	0.07119	27.76
97.28	0.31666	0.11071	34.96
107.28	0.39658	0.09573	24.14
117.28	0.47965	0.10845	22.61
127.28	0.48878	0.08730	17.86
137.28	0.44982	0.09078	20.18
147.28	0.37756	0.09271	24.56
157.28	0.26686	0.13024	48.80
167.28	0.10528	0.07445	70.71

Table 6.9: ^{3}He(e,e′p)pn cross section results for $P_m = 900$ MeV/c (kin28).

E_m (MeV)	Cross Section pb/(MeV^{2}sr^2)10^{-2}	Stat-uncer pb/(MeV^{2}sr^2)10^{-2}	Rel. uncer (%)
77.28	0.02594	0.0155	59.82
87.28	0.02939	0.0232	78.95
97.28	0.03172	0.0112	35.35
107.28	0.03889	0.0199	51.34
117.28	0.04412	0.0136	31.04
127.28	0.04294	0.0132	30.74
137.28	0.04101	0.0124	30.18
147.28	0.03695	0.0168	45.68
157.28	0.03265	0.0364	111.66
167.28	0.02348	0.0235	100.

Table 6.10: $^3\mathrm{He(e,e'p)pn}$ cross section results for $P_m = 290$ MeV/c (kin9).

E_m (MeV)	Cross Section pb/(MeV^{2}sr^2)10^{-2}	Stat-uncer pb/(MeV^{2}sr^2)10^{-2}	Rel. uncer (%)
7.28	0.85703	0.1370	15.98
17.28	0.83450	1.040E-01	12.47
27.28	0.68986	9.805E-02	14.21
37.28	0.52103	8.268E-02	15.87
47.28	0.40168	8.566E-02	21.33
57.28	0.30443	7.514E-02	24.68
67.28	0.26653	0.15048	56.46

Table 6.11: $^3\mathrm{He(e,e'p)pn}$ cross section results for $P_m = 330$ MeV/c (kin9).

E_m (MeV)	Cross Section pb/(MeV^{2}sr^2)10^{-2}	Stat-uncer pb/(MeV^{2}sr^2)10^{-2}	Rel. uncer (%)
7.28	0.7263	1.015E-01	13.99
17.28	0.7907	0.10502	13.28
27.28	0.7356	1.393E-01	13.65
37.28	0.6766	9.174E-02	15.20
47.28	0.4655	8.341E-02	17.92
57.28	0.3537	9.192E-02	25.98
67.28	0.3063	0.1293	42.21

6.5.2 Momentum density distribution tables

Table 6.12: ^{3}He(e,e$'$p)pn effective momentum density distribution (kin29).

P$_m$ (MeV/c)	Density (fm^{-3})	Total uncer (fm^{-3})	RelEr(extra) (%)	RelEr(Stat) (%)	Rel(total) (%)
975.	2.5396E-05	8.2274E-06	0.144	0.272	32.3
1025.	1.7472E-05	5.4984E-06	0.14	0.262	31.4
1075.	9.5250E-06	2.8642E-06	0.137	0.248	30.0
1125.	5.2697E-06	1.5308E-06	0.134	0.23	29.0

Table 6.13: ^{3}He(e,e$'$p)pn effective momentum density distribution (kin4).

P$_m$ (MeV/c)	Density (fm^{-3})	Total uncer (fm^{-3})	RelEr(extra) (%)	RelEr(Stat) (%)	Rel(total) (%)
120.	0.08370	0.840	0.	0.9597	10.04
140.	0.04851	0.486	0.	0.8250	10.03
160.	0.02914	0.292	0.	0.8181	10.03
180.	0.01848	0.185	0.	0.8639	10.04
200.	0.01161	0.116	0.	0.9764	10.04
220.	0.77703	0.078	0.	1.1399	10.06
240.	0.59092	0.059	0.	1.3812	10.09
260.	0.56649	0.057	0.	1.7821	10.16

Table 6.14: ^{3}He(e,e$'$p)pn effective momentum density distribution (kin13)

P$_m$ (MeV/c)	Density (fm^{-3})	Total uncer (fm^{-3})	Rel(extra) (%)	Rel(Stat) (%)	Rel(total) (%)
240.	0.76676	0.0784	0.	2.272943	10.25
260.	0.43613	0.0443	0.	1.881895	10.17
280.	0.32436	0.0328	0.	1.648834	10.13
300.	0.25970	0.0262	0.	1.521616	10.11
320.	0.25888	0.0261	0.	1.398355	10.09
340.	0.24137	0.0243	0.	1.351334	10.09
360.	0.23390	0.0236	0.	1.363116	10.09
380.	0.25139	0.0254	0.	1.470393	10.10
400.	0.22596	0.0229	0.	1.673365	10.14

Table 6.15: ^{3}He(e,e$'$p)pn effective momentum density distribution (kin10).

P$_m$ (MeV/c)	Density (fm^{-3})	Total uncer (fm^{-3})	Rel(extra) (%)	Rel(Stat) (%)	Rel(total) (%)
370.	0.147028	0.0423	26.5882	3.0134	27.22
390.	0.183159	0.030437	15.6940	2.2047	16.61
410.	0.178076	0.015850	7.12913	1.8441	8.98
430.	0.149241	0.011299	5.44246	1.6430	7.57
450.	0.140313	0.011813	6.59901	1.5297	8.42
470.	0.128313	8.852E-05	4.4997	1.5329	6.89
490.	0.119861	6.278E-05	0.	1.5625	5.24
510.	0.109239	5.755E-05	0.	1.6598	5.27
530.	0.104896	5.597E-05	0.	1.8631	5.33
550.	0.095623	5.202E-05	0.	2.1449	5.44
570.	0.104495	5.919E-05	0.	2.6624	5.66

Table 6.16: ^{3}He(e,e$'$p)pn effective momentum density distribution (kin13).

P$_m$ (MeV/c)	Density (fm^{-3})	Total uncer (fm^{-3})	Rel(Extra) (%)	Rel(Stat) (%)	Rel(total) (%)
490.	0.0624	6.5740E-05	8.44	3.83	10.53
510.	0.0836	0.01389	15.57	2.91	16.61
530.	0.0906	0.01751	18.50	2.35	19.31
550.	0.0774	5.1774E-05	3.92	2.08	6.68
570.	0.0578	3.7129E-05	3.54	1.90	6.42
590.	0.0571	3.0433E-05	0.	1.82	5.33
610.	0.0525	2.7946E-05	0.	1.79	5.31
630.	0.0435	2.3274E-05	0.	1.88	5.34
650.	0.0405	2.1779E-05	0.	1.95	5.37
670.	0.0334	1.8121E-05	0.	2.10	5.42
690.	0.0266	1.4912E-05	0.	2.50	5.59

Table 6.17: ^{3}He(e,e$'$p)pn effective momentum density distribution (kin28).

P$_m$ (MeV/c)	Density (fm^{-3})	Total uncer (fm^{-3})	Rel(extra) (%)	Rel(Stat) (%)	Rel(total) (%)
740.	0.01383	4.092E-05	26.40	8.70	29
760.	0.01131	3.463E-05	27.70	8.04	31
770.	0.01298	1.755E-05	5.40	7.259	13
800.	0.01118	1.597E-05	7.70	6.601	14
820.	0.01114	1.326E-05	0.	6.466	12
840.	9.21E-05	1.107E-05	0.	6.659	12
860.	8.70E-05	1.055E-05	0.	6.846	12
880.	6.57E-05	8.247E-06	0.	7.576	12
900.	5.47E-05	7.2658E-06	0.	8.745	13

6.5.3 Transverse-longitudinal asymmetry tables

Table 6.18: $\mathrm{A_{TL}}$ Asymmetry table for $\mathrm{P}_m = 440 \pm 5\,\mathrm{MeV}/c$.

E_m(MeV)	Cs(Kin10)	erCs(Kin10)	Cs(Kin11)	erCs(Kin11)	$\mathrm{A_{TL}}$	$\mathrm{eA_{TL}}$
7.28	4.9799	0.264	1.916	0.585	-0.4441	2.84E-02
17.28	7.4089	0.343	4.125	1.123	-0.2847	8.67E-03
27.28	8.4751	0.366	6.744	0.924	-0.1137	1.17E-03
37.28	9.0853	0.371	8.093	0.934	-5.773E-02	4.30E-04
47.28	8.9448	0.374	8.486	1.194	-2.630E-02	2.26E-04
57.28	7.7459	0.373	7.663	0.885	-5.352E-03	4.36E-05
67.28	5.7339	0.348	6.045	0.959	2.647E-02	3.74E-04
77.28	3.8284	0.336	4.266	0.770	5.405E-02	1.29E-03
87.28	3.2390	0.486	2.741	0.761	-8.328E-02	4.61E-03
97.28	6.6779	1.470	1.945	0.665	-0.5488	3.43E-02

Table 6.19: $\mathrm{A_{TL}}$ Asymmetry table for $\mathrm{P}_m = 330 \pm 5\,\mathrm{MeV}/c$.

E_m(MeV)	Cs(Kin7)	erCs(Kin7)	Cs(Kin8)	erCs(Kin8)	$\mathrm{A_{TL}}$	$\mathrm{eA_{TL}}$
7.28	15.586	0.872	19.791	1.950	0.1188	2.91E-02
17.28	16.256	0.785	13.356	1.423	-9.790E-02	3.86E-02
27.28	15.124	0.661	15.369	2.342	8.044E-03	3.98E-03
37.28	12.539	0.588	14.839	3.048	8.403E-02	5.77E-02
47.28	9.1723	0.503	11.067	4.060	9.364E-02	0.1538
57.28	6.0857	0.387	6.7686	3.547	5.312E-02	0.2050
67.28	3.5622	0.265	3.2512	1.441	-4.564E-02	0.3106

Chapter 7

Summary and Conclusion

In the introduction of this thesis, we defined the goal to be the investigation of nucleon-nucleon correlations in the ^{3}He nucleus, using the ^{3}He(e,e′p)pn reaction. There are several advantages of ^{3}He for this study:

- ^{3}He has been the subject of study of numerous theoretical groups, and it is now viewed that, starting from the nucleon-nucleon force (plus a three-body force) the structure of ^{3}He can be predicted essentially as reliably as the structure of the deuteron.

- The deuteron lacks the three-body forced present in ^{3}He as well as the correlation peak in the continuum region.

- Heavier nuclei cannot be predicted as reliably as ^{3}He, and the correlation peak in the continuum is obscured by many-body effects.

The experimental measurements were very successful. We used the Jefferson Lab Hall A high-resolution spectrometers with a high-luminosity cryogenic ^{3}He target, and an intense high-energy, continuous-wave beam. We presented in this thesis a comprehensive set of cross sections at a single four momentum transfer, Q^2 = 1.55 GeV^2, in kinematics corresponding to being nearly on top of the quasifree peak. The data covered missing energies up to pion production threshold, and missing momenta up to over 1 GeV/c; this data set is much more extensive than any previous data set on ^{3}He, and superior to measurements on other nuclei as well.

In the data, the correlation peak was easily observed, and its center was seen to vary with missing momentum as predicted by the simple plane-wave impulse approximation and spectator nucleon model. In the theoretical work of J.M. Laget, this arises because the final-state interactions between the two correlated nucleons do not shift the peak, and other reaction mechanism effects are small – interactions with the spectator nucleon, isobars, and meson exchange currents.

By integrating the total strength of the continuum from breakup to pion production threshold, we could make a simple and direct comparison of the relative strengths of two and three body breakup of ^{3}He. We found that the ratio of strengths, of 2bbu to 3bbu, was in general a rapidly decreasing function of p_m. At low p_m, below about 100 MeV/c, the 2bbu strength is about 100 times that of the 3bbu. The strengths become equal at about 200 MeV/c, near the Fermi momentum. Above 500 MeV/c, the 3bbu strength is nearly 100 times that of the 2bbu.

The picture, based again on Laget's work, is as follows. At some points in time the three nucleons all have relatively low momenta, below a few hundred MeV/c. If a photon is then absorbed on one proton, it is ejected, and the other two nucleons have low relative momenta and are likely to form a deuteron.

At other points in time, two nucleons have come close together, and now have high relative momenta, indicating a short-range correlation. Now if a high momentum proton is struck, the remaining two nucleons have high relative momenta, and are unlikely to form a deuteron, so the continuum, 3bbu, final state results.

We saw that Laget's calculations (and preliminary work from other theorists, that is appearing too late to include in this work) reproduce both the 2bbu and 3bbu well up to nearly 1 GeV/c. An important ingredient in this work was the inclusion of both correlations and final-state interactions. Without correlations, the high-momentum tail of the nuclear wave function and the resulting cross sections are reduced orders of magnitude. The final-state interactions also increase the cross section by a factor of several. This large contribution indicates that one likely cannot make precise statements about the magnitude of the two separate effects. It is likely that as more calculations are done, using slightly different but equally good effective nuclear interactions, we will find strength redistributed between these two large, and the other smaller, pieces of physics.

Since Laget's theory works well, there is no *need* to invoke quark effects to understand the measurements. Near 1 GeV/c, however, the agreement begins to break down. In the these we argued first that the apparent convergence in the data is likely an artifact of the kinematic coverage. If pion production were small, and we measured the entire continuum strength, which is largely above pion production threshold at large p_{miss}, we believe we would find the ratio of 3bbu to 2bbu to be about constant and about 100. This is based on a simple estimate, so it is a likely scenario, but it is of course unprovable. As regards the theory, it is very possible that added terms in the diagrammatic expansion can improve the agreement with the data.

Finally, we presented some results for the asymmetry in the cross sections for protons going forward vs. backward of the photon direction, A_{TL}. The data show near 0 asymmetry, very different from plane wave predictions of a large asymmetry. Final state interactions move the prediction towards 0, and account for most of the difference. Thus there is good qualitative success.

A very brief recapitulation is as follows:

- We have made the most extensive measurements to date of the continuum region in ^{3}He(e,e$'$p)pn.
- A modern theory provides an excellent description of the cross sections over a wide range, and a good qualitative explanation of the asymmetry A_{TL}.
- The success of the hadronic theory indicates that one does not need to invoke quark degrees of freedom to understand the data.

Appendix A

Theoretical Review

A.1 Ground state wave function for the three-nucleon system

The wave function is a solution of the non-relativistic $\mathrm{Schrodinger}$ equation H $|\psi>= E|\psi>$. To calculate this wave function we need a potential and a solution method. Variational method and the resolution of the Faddeev equation are the two most frequently used methods. The Hamiltonian is given by:

$$H = H_0 + \frac{1}{2}\sum V_{ij} + W_{ijk}. \tag{A.1}$$

Here, $\mathrm{H_0} = \sum \mathrm{T_i}$ is the three nucleon kinetic energy Hamiltonian. $\mathrm{V_{ij}}$ represents the interaction of two nucleons described by a nucleon-nucleon potential. $\mathrm{W_{ij}}$ is the three nucleon interaction term which represents the three body forces.

A.1.1 Choice of a frame and Jacobi coordinates

In a non-relativistic theory, a system of three particles, each of spin 1/2 and isospin 1/2, can be represented by the normalized states: $|\mathrm{k_1 k_2 k_3}, \sigma_1\sigma_2\sigma_3, \tau_1\tau_2\tau_3\rangle$ where $\mathrm{k_i}$, σ_i and τ_i are the momentum, the spin and the isospin of the particle i, respectively. The kinetic energy of this three-nucleon state is:

$$E_0 = \sum_i \frac{k_i^2}{2M_i}. \tag{A.2}$$

The three nucleons are considered to have the same mass. In the center of mass frame is the most adequate for the description of the intrinsic quantities of the three-nucleon system. We can separate the kinetic energy of this system into a part describing the center of mass and into a relative part (taking into account the movement of the nucleons in the center of mass frame), using Jacobi's coordinates:

$$p_i = \frac{1}{2}\left(\frac{1}{M_n}\right)^2 (k_j - k_k),\ q_i = \frac{1}{6}\left(\frac{3}{M_n}\right)^2 (k_j + k_k - 2k_i) \tag{A.3}$$

The kinetic energy is then given by: $\mathrm{E_0 = \frac{1}{6M_n} + K^2 + p^2 + q^2}$,

where $\mathrm{K = \sum_i k_i}$.

If $|\psi_1\rangle$ is the wave function in the base $|\mathrm{p_1\ q_1}\rangle$, the antisymmetrized wave function is obtained by the permutation of the nucleons:

$$|\psi_A\rangle = \frac{1}{\sqrt{3}}(1 + \epsilon_{123} + \epsilon_{321})|\psi_1\rangle \tag{A.4}$$

where ϵ_{ijk} is the circular permutation operator $\mathrm{(ijk) \rightarrow (jki)}$.

The wave function of the system A can be found in any other frame from it's expression in the center of mass frame plus a plane wave representing the motion of the center of mass.

A.1.2 Faddeev Equations

Faddeev equations allow the calculation of the wave function of a bound state of a three nucleon NNN system, as well as the wave function of a scattering state $\mathrm{NNN \rightarrow Nd}$.

For a three-nucleon system (1, 2, 3), Faddeev equations are given by [71]:

$$T^k(z) = t_k + t_k G_0(z) \sum_{m \neq k} T^m(z) \tag{A.5}$$

where $\mathrm{t_k}$ is the transition operator of the pair k. $\mathrm{z = E + i}\,\epsilon$ and $\mathrm{G_0(z) = \frac{1}{z - H_0}}$ is the Green's function of the three free nucleons.

The wave function of the three-nucleon bound state can be expressed as the sum of "Feddeev amplitudes": $|\psi\rangle = \sum_{i=1}^{3} |\psi_i\rangle$, solutions of the the coupled homogeneous equations:

$$|\psi\rangle = G_0(z)T^i(z)\sum_{i\neq k}^{3} |\psi_i\rangle \tag{A.6}$$

where $T^i(z)$ are the three components of the scattering operator T defined by the integral equation A.5.

In the case where the three particles have equal masses, the amplitudes $|\psi_{\mathrm{i}}\rangle$ are formally identical: $|\psi_{\mathrm{i}}(\mathrm{p}_1, \mathrm{q}_1\rangle \equiv |\psi_2(p_2, q_2)\rangle \equiv |\psi_3(p_3, q_3)\rangle$. Knowing one of them is enough for the determination of $|\psi_i\rangle$.

A.1.3 Variational Method

The variational method allows the calculation of the three-nucleon system wave function, by using the Ritz variational principle which stipulates that the ratio $\frac{\langle\psi|\mathrm{H}|\psi\rangle}{\langle\psi|\psi\rangle}$, where ψ is a trial function, is minimal for the ground state.

A.1.4 Nucleon-Nucleon Potential

Nucleon-Nucleon potential includes the following:

- **a local interaction**, generally expressed as:

$$v_{ij}^{loc}(\vec{r}, \vec{\sigma}, \vec{\tau}) = v_0(\vec{r}, \vec{\tau}) + v_\sigma(\vec{r}, \vec{\tau})\vec{\sigma_i} \cdot \vec{\sigma_j} + v_\tau(\vec{r}, \vec{\tau})S_{ij} \tag{A.7}$$

  where $\vec{\sigma}$ is the spin, $\vec{\tau}$ the isospin, $\vec{L}$ the orbital momentum, and $\vec{S}$ the total spin. The two quantities v_0 and v_σ which commute with $\vec{L}$, L^2, $\vec{S}$ and S^2, form the <u>central part</u> of the of the interaction. The quantity v^τ, which commutes only with S^2, represents the <u>tensor interaction</u>.

- **a non local interaction**, expressed as:

$$v_{ij}^{nloc} = v_{ij}^{loc} + v_{so}\vec{L}\cdot\vec{S}. \tag{A.8}$$

Paris Potential [69] (fr the Faddeev equations), Argonne Potential (for the variational method) and Urbana potential are the most frequently used. These three potentials describe the nucleon-nucleon interaction in terms of meson exchange. The long range part (r $\geq$ 2 fm) is dominated by the one pion exchange process (OPEP).

$$v_{OPEP} = c\vec{\tau_i}\cdot\vec{\tau_j}\left[\vec{\sigma_i}\cdot\vec{\sigma_j} + S_{ij}\left(1 + \frac{3}{rm_\pi} + \frac{3}{(rm_\pi)^2}\right)\right]\frac{e^{-rm_\pi}}{rm_\pi} \tag{A.9}$$

where $S_{ij} = \frac{3}{r^2}(\vec{\sigma_i}\cdot\vec{r})(\vec{\sigma_j}\cdot\vec{r}) - \vec{\sigma_i}\cdot\vec{\sigma_j}$ generates the D state components of the wave function.

Paris Potential

The Paris potential is a non-local potential of type VI.8, including a quadratic spin-orbit term $\left(\tilde{\mathrm{L}}\cdot\tilde{\mathrm{S}}\right)^2$. In this potential, two meson exchange describes the medium range of the interaction (0.8 $\leq$ r $\leq$ 2 fm). The calculation of this range was performed from $\pi\mathrm{N}$ and $\pi\pi$ interactions. The short range part $(\mathrm{r} \leq 0.8\mathrm{fm})$ is described by a “soft core” adjusted phenomenologically.

The Argonne-Urbana Potential is used by Schiavilla $et\,at.$, [72] for the two-body potentials of Argonne [73] or [18] for the calculation of the two body wave function.

Appendix B

Trigger electronics block diagrams

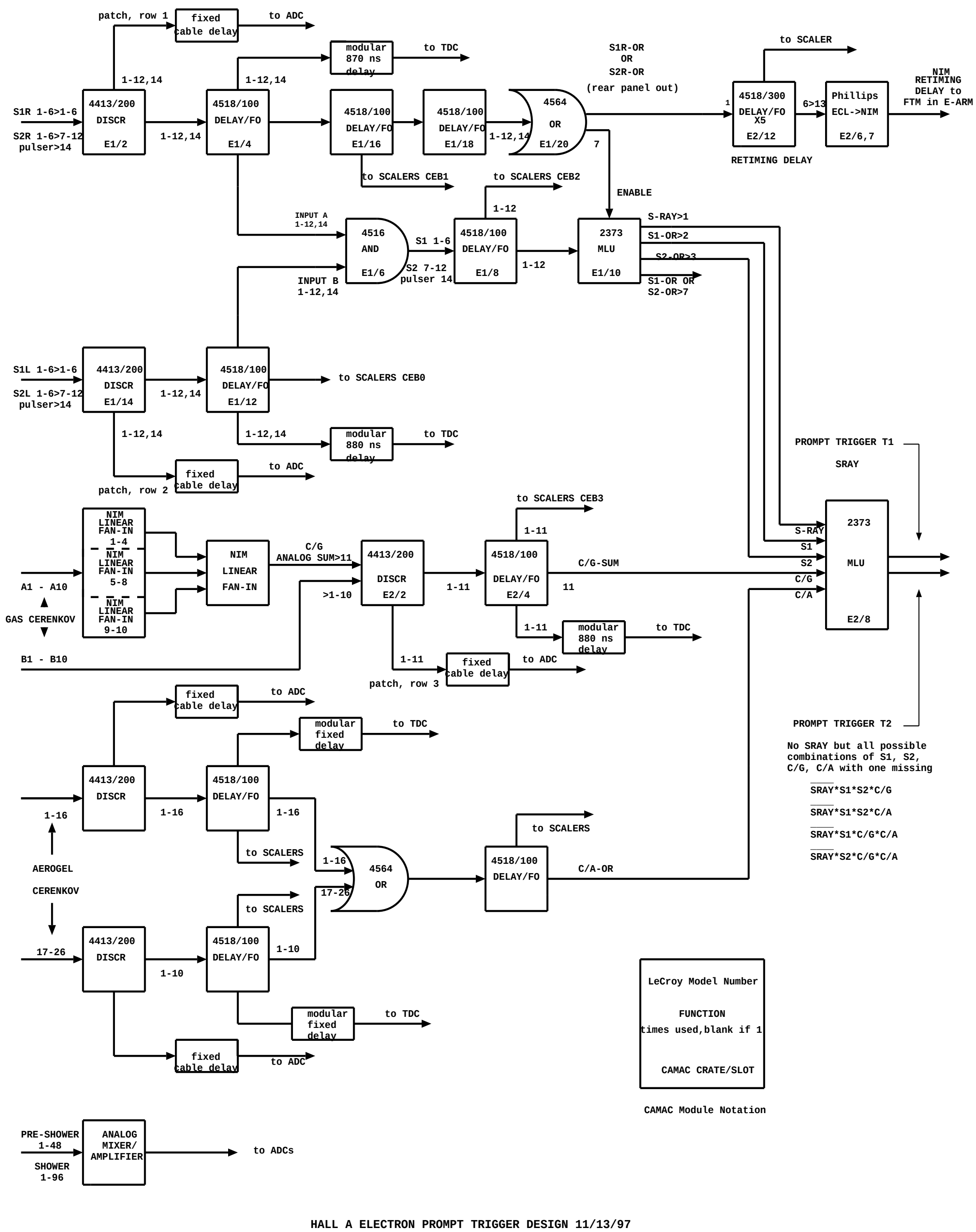

Figure B.1: Block diagram of setup of the electron singles trigger.

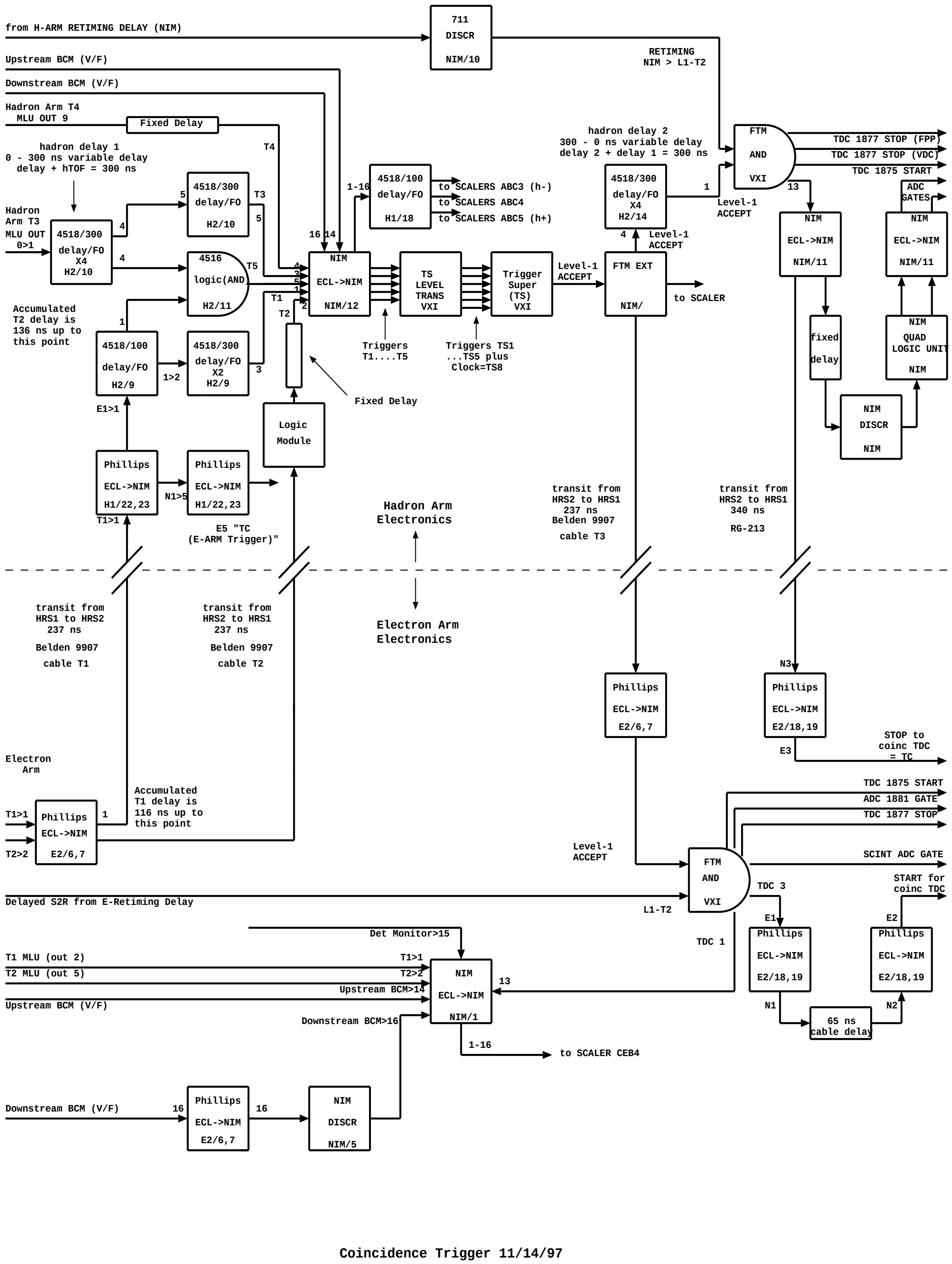

Figure B.2: Block diagram of coincidence circuit of the coincidence trigger.

Appendix C
Analysis codes

C.1 Acceptance definition with R-functions

The following is the definition of the "cut function" f_1 constructed with the R-function technique. The cut on the cut function f_1, together with the cut on the reaction point along the beam and the cut on the reconstructed out-of-plane angle, restricted coincidence events to a flat acceptance region of both spectrometers. Below, f_1 is defined as a PAW function. This definition was used in restricting experimentally reconstructed events to the flat acceptance region. An equivalent definition was coded into the simulation code MCEEP and was used to restrict simulated events to an identical acceptance region.

```
      REAL FUNCTION rfcut()
      include ?
      REAL F1,F2
      REAL sp_cut

      F1=sp_cut(y_tgth,ph_tgth,th_tgth,dph)
      F2=sp_cut(y_tgte,ph_tgte,th_tgte,dpe)
      rfcut=PROD(F1,F2)
      END

* Definition of cut on one spectrometer
      REAL FUNCTION sp_cut(y_tgth,ph_tgth,th_tgth,dph)
```

```
      REAL C1,C2,C3,C4,C5,C6,C7,C8,C9,C10,C11,PROD
      REAL D1,D2,D3,D4,D5
      REAL E1,E2
      REAL y_tgth,ph_tgth,th_tgth,dph
* Definition of hyperplanes forming initial domain
      C1=-0.0137*ph_tgth+0.0502-th_tgth
      C2=0.0502+th_tgth
      C3=-0.136*y_tgth+0.02518-0.991*ph_tgth
      C4=y_tgth*0.136+0.02518+0.991*ph_tgth
      C5=-0.975*dph+0.0396-0.220*th_tgth
      C6=dph+0.0409+0.068*th_tgth
      C9=-0.421*dph-0.907*th_tgth+0.0561
      C7=-dph*0.1776+0.984*ph_tgth+0.0237
      C8=-dph*0.1738+0.0236-0.985*ph_tgth
      C10=0.319* y_tgth-0.948*ph_tgth+0.0336
      C11=-0.319*y_tgth+0.948*ph_tgth+0.0336

* Pairwise products of hyperplane functions
      D1=PROD(C1,C2)
      D2=PROD(C3,C4)
      D3=PROD(C5,C6)
      D3=PROD(C9,D3)
      D4=PROD(C7,C8)
      D5=PROD(C10,C11)

      E1=PROD(D1,D2)
      E2=PROD(D3,D4)
      E2=PROD(E2,D5)
```

```
      sp_cut=PROD(E1,E2)
      END

* Definition of R-function corresponding to logical AND
      REAL FUNCTION PROD(X,Y)
      REAL X,Y

      PROD=MIN(X,Y)
* Below are alternative definitions of R-functions
* corresponding to logical AND
*      PROD=X+Y-SQRT(X*X+Y*Y+2*0.9*X*Y)
*      PROD=X+Y-SQRT(X*X+Y*Y)
      RETURN
      END
```

C.2 Interpolation and Extrapolation of Salme's spectral funtion

```
C----------------
C Read He3-salme-cont.dat
C Normalization: 4pi x Integral(dp p^2 momdist) = 1.326
C (2-body)
C 4pi x Integral(dpdE p^2 momdist) = 0.638 (3-body)
C----------------
C      SUBROUTINE H(BOUND)
C

      Implicit none
```

```
        DOUBLE PRECISION E(200),P(81)
        DOUBLE PRECISION SP(81),SPC(81,200),FRAC_P(200)
        DOUBLE PRECISION EM(200),PM(81),FRAC_E(200,200),
        INTEGER I,J,N_PM,N_EM,N_DAT_DIR
        DOUBLE PRECISION SE1(200,200),SE2(200,200),S11(200,200)
        DOUBLE PRECISION S12(200,200),S21(200,200),S22(200,200)
        DOUBLE PRECISION HBAR,HBARC3
c       INTEGER I,J,N_PM,N_EM
        DOUBLE PRECISION HSP(200,200)
c       LOGICAL BOUND

c       PARAMETER (HBARC =197.327D0)! Hbar*C    in  MeV-fm
c       PARAMETER (HBARC3=7.68369D6)!(Hbar*C)^3 in (MeV-fm)^3

        OPEN(UNIT=3,FILE='he3-salme-cont.dat',STATUS='OLD')
        READ(3,*)N_PM,N_EM
            DO I=1,N_PM
               READ(3,*) P(I)
               DO J=1,N_EM
                  READ(3,*) E(J),SPC(I,J)
c                write(*,*) E(J)
                ENDDO
              ENDDO
c           ENDIF
C
c           CLOSE(UNIT=3)
           do i =1, 199
```

```
      EM(i)=E(i+1)
      enddo
      do j=1,81
      PM(J)=(P(j)+P(J+1))/2
       enddo
C
c     DO I=1,N_PM
c     do J=1,200
c     IF(PM(I).LE.P(I)) GOTO 250
c     ENDDO
c    HSP(I,J)=0.D0 ! NOT TABULATED UP TO THIS MOMENTUM
c    RETURN
c 250  IF(EM(J).LE.E(J)) GOTO 301
c      ENDDO
c      HSP(I,J)=0.D0 ! NOT TABULATED UP TO THIS ENERGY
c      RETURN
c 301 CONTINUE  ! Successful: found indices I and J
        do i=1, 81
        do j=1,200
c        IF (J.EQ.1) THEN
c          HSP(I,J)=0.D0 ! Do not interpolate for EM<E(1)
c           RETURN
c          ENDIF

c    IF (I.EQ.1) THEN
c        FRAC_E(I,J) = (EM(J)-E(J-1)) / (E(J)-E(J-1))
c        S21(I,J) = SPC(I,J-1)
c        S22(I,J) = SPC(I,J)
```

```
c        HSP(I,J) = FRAC_E(I,J)*(S22(I,J)-S21(I,J))+S21(I,J)
c        ENDIF
c  IF (I.GT.1.AND.J.GT.1) THEN !interpolation in EM and PM

    FRAC_E(I,J) = (EM(I)-E(J-1)) / (E(J)-E(J-1))
    FRAC_P(I) = (PM(I)-P(I-1)) / (P(I)-P(I-1))
    S11(I,J) = SPC(I-1,J-1)
    S12(I,J) = SPC(I-1,J)
    S21(I,J) = SPC(I,J-1)
    S22(I,J) = SPC(I,J)
    SE1(I,J)=LOG(FRAC_E(I,J)*(S12(I,J)-S11(I,J))+S11(I,J))
    SE2(I,J)=LOG(FRAC_E(I,J)*(S22(I,J)-S21(I,J))+S21(I,J))
    HSP(I,J)=EXP(FRAC_P(I)*(SE2(I,J)-SE1(I,J))+SE1(I,J))
    ENNDO
    ENNDO
     open (4,file='Prog.dat', status='unknown')
      DO I=1,80
        write(4,*) PM(I)
          DO J=1,200
        write(4,*) EM(J),HSP(I,J)
          ENNDO
        ENNDO


c      RETURN
       stop
       END
C
```

References

[1] E. Jans *et al.*, Nucl. Phys. A **475**, 687 (1994).

[2] P. H. M. Keizer *et al.*, Phys. Lett. B **197**, 29 (1987).

[3] C. Marchand *et al.*, Phys. Rev. Lett. **60**, 1703 (1988).

[4] J. M. Le Goff *et al.*, Phys. Rev. C **55**, 1600 (1997).

[5] R. Florizone, PhD thesis, MIT (1999).

[6] P. H. M. Keizer *et al.*, Phys. Lett. B **157**, 29 (1985).

[7] C. Tripp *et al.*, Phys. Rev. Lett. **76**, 885 (1996).

[8] C. M. Spaltro *et al.*, Phys. Rev. Lett. **81**, 2898 (1998).

[9] D. H. Beck, Phys. Rev. Lett. **64**, 268 (1990).

[10] T. W. Donnelly and A. S. Raskin, Ann. Phys **169**, 247 (1986).

[11] T. W. Donnelly and A. S. Raskin, Ann. Phys **191**, 78 (1989).

[12] A. Picklesimer *et al.*,Phys. Rev. C **32**, 1312 (1985).

[13] A. Picklesimer and J. W. Van Orden, Phys. Rev. C **35**, 266 (1987).

[14] S. Boffi *et al.*,Nucl. Phys. A **476**, 617 (1988).

[15] J. J. Kelly, Adv. Nucl. Phys. **23** ed. by J. W. Negele and E. Vogt 75 (1996).

[16] N. K. Liyanage, PhD thesis, Massachusetts Institute of Technology, (1999).

[17] L. Frankfurt and M. Strikman, Phys. Rep. **76**, 236 (1981).

[18] J. M. Laget, Nucl. Phys. A **358**, 275 (1981).

[19] T. DeForest, Nucl. Phys. A **392**, 232 (1983).

[20] Jefferson Lab Experiment E89-044, 'Selected Studies of the ^{3}He Nucleus Through Electro-disintegration at High Momentum Transfer' , M. Epstein, A. Saha, E. Voutier, spokespeople.

[21] J. E. Ducret *et al.*, Nucl. Phys. A **553**, 697 (1993).

[22] G. G. Simon *et al.*, Nucl. Phys. A **333**, 381 (1980).

[23] M. Rvachev, Ph.D. thesis, Massachussetts Institute of Technology (2003).

[24] E. Penel-Notaris, Doctorate thesis, University Joseph Fourrier, (2004).

[25] W. Barry, $et\ al.$, Jlab-TN-90-246, (1990).

[26] J. Bertho, P. Vernin, NPN **9**, 12 (1990).

[27] E. Offerman $et\ al.$, ESPACE: Event Scanning Programm for Hall A Collaboration Experiments, v.2.9B, (2000).

[28] J. Alcorn $et\ al.$, Nucl. Inst. Meth. A **522**, 294 (2004); see also `http://www.jlab.org/Hall-A/equipment/HRS.html`.

[29] See `http://www.coda.jlab.org/`.

[30] EPICS, see `http://aps.anl.gov/epics/`.

[31] CERN Program Library, see `wwwasd.web.cern.ch/wwwasd/cernlib.html`.

[32] HBOOK-Statistical Analysis and Histogramming, CERN Program Library Long Writeup Y250, see `wwwasd.web.cern.ch/wwwasd/hbook/HBOOKMAIN.html`.

[33] GEANT, Detector description and simulation tool, CERN Program Library W5013, see `wwwinfo.cern.ch/asd/geant/`.

[34] F. Benmokhtar $et\ al.$, "Spectrometer Setups", Report to E89044 collaboration, (2000).

[35] C. Curtis, Private communication.

[36] J. Gomez, Private communication.

[37] M. Jones, Report of electronic deadtime, (2000). See `http://www.jlab.org/~jones/e91011/report_on_deadtime.ps`.

[38] See `http://hallaweb.jlab.org/equipment/daq/daq_trig.html`.

[39] See `http://www.physics.odu.edu/~ulmer/mceep/mceep.html`.

[40] M. Rvachev, TJNAF Hall A Technical Note Jlab-TN-01-0555

[41] A. Amroun $et\ al.$, Nucl. Phys. A **579**, 596 (1994).

[42] C. R. Otterman $et\ al.$, Nucl. Phys. A **435**, 688 (1985).

[43] J. Heinsenberg and H. P. Blok, Ann. Rev. Nucl. Part. Sci. **33**, 569 (1983).

[44] F. Benmokhtar, ’Compiled list of good runs for E89044’, see `http://www.jlab.org/~doug/e89044/fatiha_runs.txt`.

[45] W. Leo, "Technics of Nuclear and Particle Physics Experiments" (Springer-Verlag, 1977).

[46] R. Sterheimer, M. Berger, and S. Seltzer, At. Data Nucl. Data Tables **30**, 261 (1984).

[47] J. Lerose, Forward Transfer Function for Hall A Spectrometers. (2002). See `http://hallaweb.jlab.org/news/minutes/transferfuncs.html`.

[48] M. Rvachev *et al.*, to appear in Phys. Rev. Lett., see `http://arxiv.org/abs/nucl-ex/0409005`, (2004).

[49] A. Kievsky, E. Pace, G. Salme and M. Viviani, Phys. Rev. C **56**, 64 (1997).

[50] J. S. Schwinger, Phys. Rev. Lett. **75**, 898 (1949).

[51] S. Penner, Nuclear Structure Physics, Proceeding of the 18^{th} Scottish University Summer School in Physics, page 69 (1977).

[52] Y. T. Tsai, Rev. Mod.Phys. **46**, 815 (1974), errata.

[53] E. Borie and D. Drechsel, Nucl. Phys. A **167**, 369 (1971).

[54] P. Ulmer, Private communication.

[55] K. Fissum and P. Ulmer, Jefferson Lab Tech. Note. 02-015 (2002).

[56] R. Schuand P. Sauer Phys. Rev. C **48**, 38 (1993).

[57] J. M. Laget, Nucl. Phys. A **579**, 333 (1994).

[58] J. M. Laget, Few Body System Supplment, **15**, 171 (2003).

[59] S. Gilad, W. Bertozzi and L. Zhou, Nucl. Phys. A **631**, 276c (1998).

[60] J. Udias, J. Javier, E. M. de Guerra, J. Amaro, and J. Caballero, in Proc. of the Vth Workshop on electromagnetic Induced Two-Hadron Emission (2001), Lund (Sweden), nucl-th/0109077.

[61] J. Gao *et al.*, Phys. Rev. Lett. **84**, 3265 (2000).

[62] J. Udias, J. Caballero, E. M. de Guerra, J. Amaro, and T. Donnelly, PRL **84**, 5441 (1999).

[63] J. U. Udias, in XXIII^{rd} International Workshop on Nuclear Theory (2004), Rila (Bulgaria).

[64] F. Benmokhtar $et\ al.$, to appear in Phys. Rev. Lett., see `http://arxiv.org/abs/nucl-ex/0408015`, (2004).

[65] F. Benmokhtar, Nucl. Phys. A **737**, S143 (2004).

[66] J. M. Laget, Phys. Lett. B **151**, 325 (1985).

[67] J. M. Laget, Phys. Rep. **69**, 1 (1981).

[68] C. Hadjuk $et\ al.$, Nucl. Phys. A **369**, 321 (1981), and Nucl. Phys. A **405**, 581 (1983).

[69] M. Lacombe $et\ al.$, Phys. Lett. B **101**, 139 (1981).

[70] J. A. Templon, C. E. Vellidis, R. F. Florizone and A. J. Sarty Phys. Rev. C **014607**, 2000 (.)

[71] L. D. Faddeev, SoV. Phys. JETP **12** 1014 (1961).

[72] R. Schavilla $et\ al.$, Nucl. Phys. A **449**, 219 (1991).

[73] R. B. Wiringa. R. A. Smith and T. L. Ainsworth, Phys. Rev. C **29**, 1207 (1984).

Curriculum Vita

Fatiha Benmokhtar

Education

10/2004-...	Postdoctoral Research Associate, University of Maryland, USA.
10/2004	Ph.D. degree in Physics from Rutgers University, USA.
09/2000-10/2004	Graduate Assistant in Nuclear Pysics, Rutgers University, USA.
11/1999-09/2000	Research at Thomas Jefferson National Accelerator Facility, VA.
.	USA.
09/1995-06/1999	Master degree in Nuclear Physics. High distinction.
.	University of Sciences and Technology (USTHB) of Algiers, Al-
.	geria collaboration with the Institute of Nuclear Sciences (ISN)
.	of Grenoble, France.
1991-1995	Bachelor degree in Physics of Radiation, High distinction, USTHB,
.	Algiers, Algeria.
06/1991	Baccalaureate degree in mathematics, high distinction. Algiers, Al-
.	geria.

Publication

F. Benmokhtar *et al.*, to appear in Phys. Rev. Lett., see `http://arxiv.org/abs/nucl-ex/0408015`, (2004).

F. Benmokhtar, Nucl. Phys. A **737**, S143 (2004).

M. Rvachev *et al.*, to appear in Phys. Rev. Lett., see `http://arxiv.org/abs/nucl-ex/0409005`, (2004).

O. Gayou *et al.*, PRL **88**, 092301 (2002).